Adhesion of Two Cylindrical Particles to a Soft Membrane Tube

by

Sergey Mkrtchyan

A thesis
presented to the University of Waterloo
in fulfillment of the
thesis requirement for the degree of
Doctor of Philosophy
in
Physics

Waterloo, Ontario, Canada, 2012

I hereby declare that I am the sole author of this thesis. This is a true copy of the thesis, including any required final revisions, as accepted by my examiners.

I understand that my thesis may be made electronically available to the public.

Abstract

The interaction of nanoparticles with biological systems, especially interactions with cell membranes, has been a subject of active research due to its numerous applications in many areas of soft-matter and biological systems. Within only a few relevant physical parameters profound structural properties have been discovered in the context of simple coarse-grained theoretical models. In this Thesis we study the structure of a tubular membrane adhering to two rigid cylindrical particles on a basis of a free-energy model that uses Helfrich energy for the description of the membrane. A numerical procedure is developed to solve the shape equations that determine the state of lowest energy. Several phase transitions exist in the system, arising from the competition between the bending energy of the membrane and the adhesion energy between the membrane and the particles. A continuous adhesion transition between the free and bound states, as well as several discontinuous shape transitions are identified, depending on the physical parameters of the system. The results are then generalized into a single phase diagram separating free, symmetric- and asymmetric-wrapping states in the phase space of the size of the particles and the adhesion energy. We show that for a relatively small size of the membrane tube the interaction between the cylinders becomes attractive in the strong curvature regime, leading to aggregation of the particles in the highly curved area of the tube that is characteristically different from the aggregation in a related three-dimensional systems. For a relatively large membrane tube size the cylinders prefer to have a non-zero separation, even in the completely engulfed state. This indicates that, i) the spontaneous curvature of the membrane may play a role in the sign of the interaction of two colloidal particles adhered to a membrane and ii) cylindrical particles can aggregate on membrane tubes and vesicles if the curvature of the membrane around the aggregation region is sufficiently large.

Acknowledgements

First and foremost, I am thankful to my supervisor, Professor Jeff Z.Y. Chen, for his guidance and support throughout my work, without which this thesis would not be possible. I am also very grateful to the members of the supervisory committee, Professors Robert Wickham, Russell Thompson and Mohammad Kohandel for all the assistance and helpful feedback provided throughout my time at the University of Waterloo. I would especially like to thank Professors Robert Wickham and Russell Thompson for taking the time to provide valuable feedback on the first draft of my thesis.

I am very grateful to a friend and a mentor, Arsen Grigoryan, who is the reason I decided to pursue a PhD in theoretical physics. Thanks Arsen for supporting me at every step in this journey.

I have benefited a lot from the incredible friendships I have made while studying at the University of Waterloo. Thanks to all my graduate friends, particularly those with whom I could exchange ideas for this thesis. ZiJian Long, Wuyang Zhang, Ying Jiang and Yu-Cheng Su, thanks for all the interesting discussions we have had. Special thanks to Francesco Franceschi, Andrea Ciani, Antony Chettupuzha, Kier von Konigslow, Kyle Denison and William Sellier for all the support during this time.

I am especially grateful to my mother and my sister for all the love and encouragement in all stages of my life, including this one.

This work was made possible by the facilities of the Shared Hierarchical Academic Research Computing Network (SHARCNET:www.sharcnet.ca) and Compute/Calcul Canada.

Table of Contents

List of Figures

Chapter 1

Introduction

1.1 Cells and Membranes

The cell is the most basic structural unit of all known living organisms and is often called the "building block of life". Although cells come in a wide variety of shapes and sizes, the basic structural elements of most cells are the same: fluid sheets enclose the contents of the cell, while networks of filaments maintain the cell's shape and organize its contents. The fluid sheet enclosing the cell – the membrane – possesses a host of interesting chemical and physical properties making it a fascinating system from a number of scientific perspectives. From the biological perspective, the plasma membrane is what defines the boundaries of the cell and separates it from its immediate environment. It has to provide protection from external stresses (chemical, mechanical, biological, etc.) that act upon the cell, yet at the same time be sufficiently flexible to allow the cell to communicate with its external environment and to grow, move, and deform as necessary [1, 2, 3]. Membranes are also found within the cell, where they partition the cell into different compartments and are essential, for example, in the production of chemical energy. Outside the cell, membranes can form tubular structures that connect two separate cells, and thus provide means for cell-to-cell communication and transport of materials from one cell to another. This, for example, makes the lipid-bilayer membranes particularly attractive for their potential use in pharmaceutical and technological applications [4, 5].

The biological relevance of fundamental physical study on lipid bilayers is also hard to underestimate. For example, the conformational behavior of membrane shapes in different physical settings can be studied with simplified models, that incorporate theoretical concepts such as bending elasticity and curvature. Of particular interest is the system of

nanoparticles interacting with cell membranes due to its applicability in many soft-matter and biological systems. For instance, with only few relevant physical parameters, the adhesion of colloidal particles to a flat, fluid sheet of membrane was theoretically shown to produce several stages of phase transitions, ending at a full envelopment of the membrane sheet about the particle [6, 7, 8, 9, 10]. The applicability of this system in biology is easy to point out – there are many examples of processes which involve encapsulation of large particles located inside a biological cell. Viruses, for example, are transported into and out of the cell in the process of endo- or exocytosis [11, 12, 13, 14, 15], in which they are fully encapsulated in the cell membrane and are subsequently pinched off (this is also how the viruses get their final coating). Because full envelopment is a necessary condition for endo/exocytosis, these physical models can provide a basis for understanding the necessary conditions for the passage of colloidal particles through cell membranes.

There is also significant interest in direct mechanical manipulation of membrane sheets in order to conform them to specific shapes or measure different properties of the membrane. This is common, for example, in many experimental techniques where membrane vesicles are manipulated by tools such as micropipetes [16, 17, 18], optical tweezers [19, 20, 21] or AFM [6]. These techniques are also widely used to stabilize membranes in different shapes, one of which, for example, is a bilayer membrane in a long tubular shape [22, 23, 24, 25, 26]. There has been significant interest in the study of structural and transport properties in systems particularly involving tubular membranes [27, 28, 29, 30, 31, 32, 33, 34, 35] and we will be interested in these structures as well.

It is interesting to note that membranes also act as a medium for interaction between nanoparticles adhered to it, which can drive different membrane transformations through the cooperative action of the particles adhered. We now know that several nanoparticles adhered to a flat membrane can interact indirectly through induced membrane curvature [7, 36, 37, 38, 39, 40, 10], aggregate and drive vesiculation [41, 42, 43] or tubulation [25, 44, 34] of membranes or even mediate attraction between two membrane sheets [45, 46]. Since all these interactions can be controlled by "fine-tuning" the membrane properties they are of significant interest in drug delivery, for example.

In this Thesis, we theoretically study the system of two rigid cylindrical particles of radius R attracted to a freely standing soft cylindrical tube of radius r_0, with co-directed axes as sketched in Fig. 1.1(A). We take the view that the membrane tube is connected to a remote "reservoir" (a vesicle, for example) that maintains a constant tension σ in the system, or equivalently, the considered membrane tube is only a segment of a much longer system where the radius is controlled at a constant value remotely. This is common in actual experimental setups where the extraction of a tubular membrane requires a much larger vesicle to act as a source of "infinite" lipid supply [22, 23, 47, 24, 25, 26].

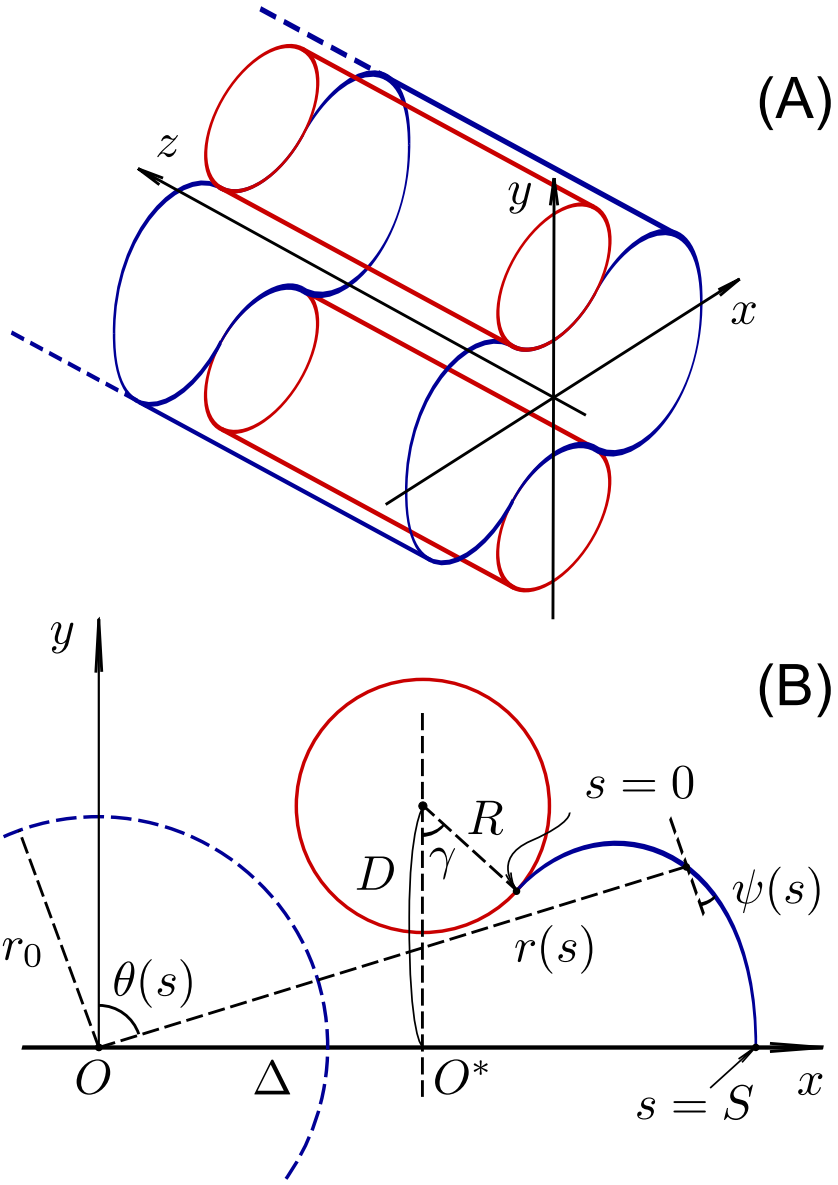

Figure 1.1: (A) Illustration of the system of two cylinders (red) adhering to a soft tubular membrane (blue). The coordinate system used in this work is shown in (B) which represents the cross-section of the upper-half of the system perpendicular to the cylinder axes.

To describe the energetics of the fluid membrane we use the Helfrich model that contains two parameters: the bending rigidity κ and surface tension σ [48, 49]. The nanoparticles adsorbed to the surface of the membrane are considered to be cylindrical in shape and of length that is much smaller than the total length of the membrane tube, so that the end effects can be ignored. Examples for such objects are cylindrical viruses or coated latex cylinders. Following Seifert and Lipowsky [50], we further introduce a phenomenological parameter w which describes the adsorption energy per unit area between the contact surfaces of the cylinders and the soft tube. We show that of five parameters, the nanoparticle radius R, their separation distance D, membrane bending rigidity κ, surface tension σ and the adhesion energy w, only three dimensionless combinations are relevant in the consideration of the structure of the current system and develop a numerical procedure that allows us to solve shape equations that correspond to the minimum of free energy. Even in two-dimensions the problem proves to be non-trivial, where special care has to be taken in order to take into account the asymmetric membrane shapes. The analysis of the free energy indicates that several phase transitions exist in the system, depending on three rescaled parameters: R/r_0, D/r_0, and wr_0^2/κ. A non-trivial adhesion transition between bound and free states is found, which arises from the competition between bending and adhesion energies and has a signature of a second-order phase transition. Beyond the bound state, increasing the adhesion energy leads to several first-order transitions, with the number of stable shapes being dependent on the relative size of the cylinders and the tube. The characteristics of different bound states are described and the results are then generalized to the case of only two relevant physical parameters: the relative size of the cylindrical particles and the adhesion energy.

The study of this model system serves two purposes, i) to provide further understanding for the structural properties of systems related to tubular membranes with two nanoparticles adhered to it, thus extending the work done in Ref. [51] and ii) to look into the interaction properties between two nanoparticles adhered to the membrane in different curvature regimes. The variety of nanotube profiles obtained can be controlled by the nanoparticle-nanotube diameter ratio and the interaction strength between the nanotube and the cylinders, which has potential applications in materials science and nanomedicine. Our results also indicate that in strong curvature regime, when the membrane wraps around the cylinders with significant shape distortion, interaction between the cylinders becomes attractive, which is indicative of the fact that the spontaneous curvature of the membrane could play a role in the sign of the interaction between the nanoparticles. This is particularly interesting, since it's been shown recently that, within the elastic theory approach, two *circular* particles on a *flat* membrane can experience attractive interaction in a sufficiently strong curvature regime. It would be interesting to see how the system behaves

for two *spherical* particles adhering to a *closed membrane vesicle*, which has proven to display complex structural behavior (and attractive interaction between the particles), for example, in light microscopy experiments [42]. Given the complex behavior of vesicles in three dimensions, it is useful to simplify the problem by reducing the dimension and to study one-dimensional vesicles embedded in two-dimensional space, which we do in our work. The numerical procedure used in solving the system can also be useful in the future study of related systems.

1.2 Literature Review

Theoretically, the physical nature of fluid membranes and vesicles can be well captured by the Helfrich free energy [49], a model that has provided insight into the physics of membrane-related systems with only a few relevant parameters. It is now often used as a theoretical basis for understanding of the conformational and dynamical properties of various systems and one may find many treatments in review articles and books [52, 53, 54, 55]. Among the biophysical problems studied within the elastic model are the shape [56, 49, 57, 58, 59] and fluctuation dynamics [60, 61, 62] of human red blood cells, the shape transformations of vesicles [52, 63, 64, 65], the interactions between multiple membrane proteins [66, 43], the interaction of tubular vesicles with a polymer solution [67] and the conformations of several nanoparticles [29], or a single polymer chain confined in a tubular membrane [27, 28]. While the above list is certainly not all-inclusive, it conveys a sense of how broad is the range of the problems that are well suited to the elastic level of membrane modeling with analytical calculation.

Our primary interest lies in the area of membrane nanoparticle interaction. One of the pioneering works in the area was the study of a simple system of a closed membrane vesicle adhering to a flat surface [50]. Within the scope of the elastic model that includes only the bending energy of the membrane and the contact potential between the membrane and the adhesion surface, numerical solutions of the shape equations revealed the existence of a large variety of different shapes. In addition, a nontrivial adhesion transition from a bound to a free state of the vesicle (even in the presence of the non-zero adhesion potential), as well as transitions between different bound states have been observed [68, 52], that were shown to be governed by the competition between bending and adhesion energies in the system. Within the same treatment, the existence of multiple shapes (and transitions between those) were shown to exist for a two-dimensional system as well, where the vesicles are cylindrical in shape, with a length much longer than their size [50]. The concept of a "pinned" state was introduced, where the vesicles aquired their original "free" shape but

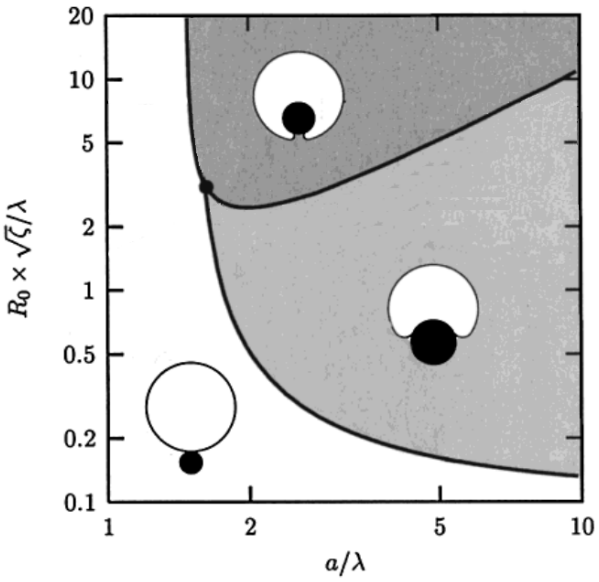

Figure 1.2: Phase diagram of colloid-vesicle complexes in the $[a, R_0]$ phase space obtained in Ref. [69]. Here a is the radius of the adhering colloid, R_0 is the radius of the membrane vesicle, $\xi = w/k_{ten}$ is the ratio between the adhesion energy and the surface expansion modulus, and $\lambda^2 = \kappa/w$, where κ is the bending modulus of the membrane. Image is taken from Ref. [69].

were still bound to the surface. In the works above, the vesicles were considered to be closed and have a limited lipid supply, hence, either a pressure difference between the exterior and the interior of the membrane surface, or the enclosed area were fixed externally.

Within the same treatment Deserno and Gelbart studied the adsorption of spherical colloidal particles onto vesicles under a constraint of fixed volume [69]. Similarly to the vesicle adhesion case three distinct states – unbound, partially wrapped and enveloped (see Fig. 1.2) – were found depending on the relative size of the adhering particle and the membrane vesicle. For large enough vesicles, decreasing the size of the nanoparticle was shown to lead first to progressively more wrapping, then to a discontinuous jump to fully enveloped state, and finally to an unbinding of the complex. For smaller vesicles, full envelopment was shown to be never achieved, instead the trend of increasing wrapping upon size reduction of the particle was shown to reverse at some point until the particle finally unbinds. A similar system of an *originally flat* fluid membrane interacting with a single spherical colloidal particle was studied by Deserno and co-workers later as well.

Even in such a seemingly simple system, where no area or volume constraints have to be imposed, and one essentially has infinite membrane supply, as the adhesion energy or the membrane tension change, two stages of phase transition were shown to occur: a second-order adsorption transition where the sphere starts to bind a weakly deformed membrane and a first-order partial-to-full wrapping transition where the last phase contains an almost fully wrapped sphere with a highly deformed membrane shape [70, 8, 9].

One naturally may ask what happens if several nanoparticles adhere to a membrane, since it is now known that membranes can act as a medium for interaction between nanoparticles adhered to it. Early experiments show that the membrane distortions caused by particle adhesion can induce interparticle attraction with a range approximately equal to the particle diameter [42]. In the same work multiple particles adhered to a fluid membrane were shown to aggregate into finite-sized two-dimensional aggregates or, unexpectedly, one-dimensional ring-like structures. Interestingly the latter result has been confirmed recently in a Monte-Carlo study, where it's been shown that fluid membranes can drive linear aggregation of spherical nanoparticles binding to it [71]. This is in contrast with expected two-dimensional clustering of nanoparticles and can lead to a number of fascinating shapes in various related systems [72].

Interface mediated interactions between two *cylindrical* particles bound to the same side of membrane have been studied via stress and torque tensors in Refs. [40, 37] and via energy minimization in Refs. [7, 37, 10]. In the pioneering work in Ref. [7], the shape profile was described in terms of small deviations of the membrane surface from a flat reference plane. For a planar membrane under lateral tension, the interaction was shown to be repulsive for a pair of cylinders adhering to the same side of the membrane, and attractive for cylinders adhering to opposite membrane sides. The results were later confirmed in a full treatment of the Helfrich model in Ref [10]. Although these works were concerned with interface-mediated forces resulting from the deformations caused by the adhering particles, it is interesting to note that a recent work by Gosselin and co-workers [73] shows that additional entropic forces induced by thermal fluctuations of the membrane actually enhance the curvature-mediated repulsion between the cylinders. This is an example of the more general Casimir forces between objects in a fluctuating medium, and interestingly, in the case of two parallel cylinders, contrasts the original formulation where two uncharged, conducting plates are predicted to attract each other due to the quantum electromagnetic fluctuations of the vacuum [74].

Approximate theories predict repulsion between membrane adhered particles [66, 75, 76, 43], but some evidence suggests that curvature-mediated attractive interactions could aid cooperation and complement the effects of specific binding events on membrane remodelling [77, 78]. This was also in line with the coarse-grained molecular dynamics simu-

lations, where it's been shown that several particles can aggregate into clusters (and drive subsequent vesiculation of the membrane) purely as a result of membrane curvature [41]. The size of the resulting vesicles was shown to correlate with the local curvature imprint of each adhering particle. Due to the challenging nature of the problem, it's been shown only recently that, within continuum elasticity model, the sign of the force reverses over an intermediate distance range, once the membrane is beyond a sufficiently strong deformation [36]. The sign flip was traced to a change in the magnitude between the two principal curvatures midway between the particles, which can only occur at sufficient particle tilt, a condition which was previously ruled out in the linearised description.

It is now also known that in addition to a variety of closed shapes normally seen in vesicles, a lipid-bilayer membrane can also be stabilized in a long tubular shape by using a number of experimental techniques [22, 23, 24, 25, 26], or through adhering nanoparticles (or polymers) that can drive tubulation of membranes [25, 44, 34]. It is possible to construct complex two-dimensional microscopic networks of nanotubes, where the connectivity, container size, the length and the angles between the tubes can be easily controlled [47]. Containers within these networks can be made to have chemically different compositions and materials can be routed between two containers via the nanotube channel. For example, Fig. 1.3 shows an intratubular transport between two liposome containers experimentally implemented by Karlsson *et al.* (see Ref. [47]) by generating membrane surface-tension difference between the containers. For charged nanoparticles the same effect can be achieved through the application of an electric potential over the two nanotube-connected vesicles. These model systems can be used for studying various properties of membranes and intracellular transport phenomena and there has been significant experimental and theoretical effort to examine the structural and transport properties in systems particularly involving tubular membranes [27, 28, 29, 30, 31, 32, 33, 34, 35].

In this work, we study the structure of the system of two rigid cylindrical particles attracted to a freely standing soft cylindrical tube with co-directed axes. The study of this model system serves two purposes, i) to provide further understanding for the structural properties of systems related to tubular membranes with two nanoparticles adhered to it, thus extending the work done in Ref. [51] and ii) to look into the interaction properties between two nanoparticles adhered to the membrane in different curvature regimes. The variety of nanotube profiles obtained can be controlled by the nanoparticle-nanotube diameter ratio and the elastic properties of the nanotube, and could be useful for potential applications in materials science and nanomedicine. Our results also indicate that for strong curvature regime, interaction between the cylinders becomes attractive, which could be indicative of the fact that the spontaneous curvature of the membrane could also play a role in the sign of the interaction between the nanoparticles. This is particularly

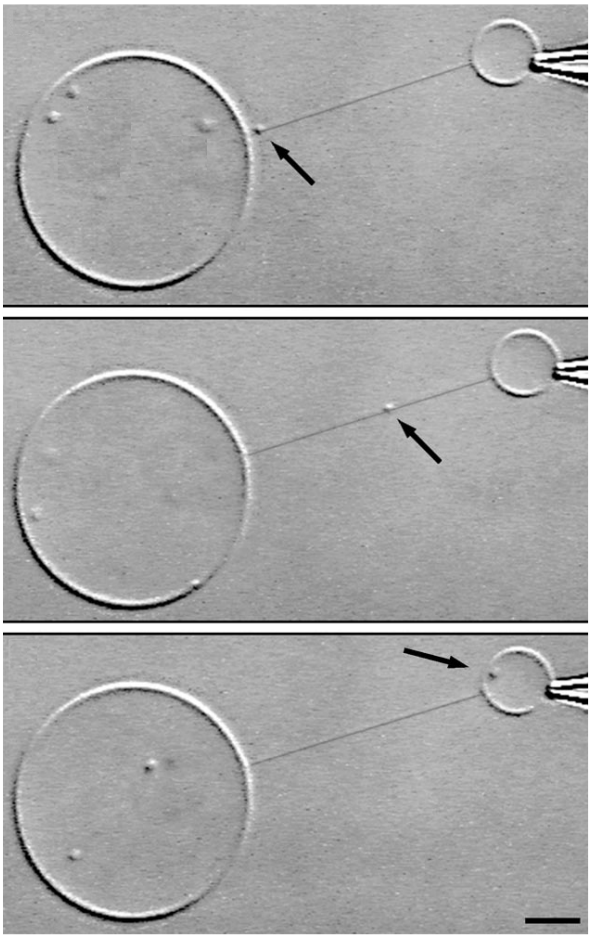

Figure 1.3: Intratubular transport between two lipid vesicles through vesicle surface tension difference. The size of the nanoparticle is around 150 nm while the scale bar is 5 μm. Image is taken from Ref. [47].

interesting, since it has been shown recently that, within the elastic theory approach, two *circular* particles on a *flat* membrane can experience attractive interaction in a sufficiently strong curvature regime. The numerical procedure used in solving the system could also be useful in the study of related systems.

Chapter 2

Theory

2.1 Biological Membranes

Membranes are a crucial part of all forms of life on Earth because they separate the cells from the external world and different compartments of the cell from each other. The primary constituent of all membranes is a lipid – an amphiphile molecule with two physically separated subdomains, one part of which is hydrophilic (able to form bonds with water molecules) and the other part of which is hydrophobic. The basic lipid structure is illustrated in Fig. 2.1, where the hydrophilic head is shown in blue, while the hydrophobic tail is shown in yellow. In an aqueous solution, beyond a certain concentration, lipid molecules form into two-dimensional structures by spontaneous aggregation. Such a process is called self-assembly and can be often found in nature when a large number of molecules, driven by the possibility to lower the free energy of the system, form a (non-trivial) condensed state. In the case of lipids, such aggregates are driven by the desire to shield its hydrophobic part against the surrounding water by using the hydrophilic part. Different morphologies can be observed in such aggregates. They can for instance cluster into spheres (called spherical micelles), with all the tails packed inside the sphere and the heads on the surface. Aggregates that are cylindrical in shape can also be formed, with the hydrophobic tails inside the cylinders and the heads on the surface (these are called cylindrical micelles). Finally, one can also imagine a double-layer in which the hydrophobic tails are sandwiched between two planes of hydrophilic head groups (see Fig. 2.1) and these are the structures that we will be interested in.

But what determines the type of the structure that is formed from the aggregation of the lipids? Without going too much into details (see Ref. [79] for a more detailed analysis)

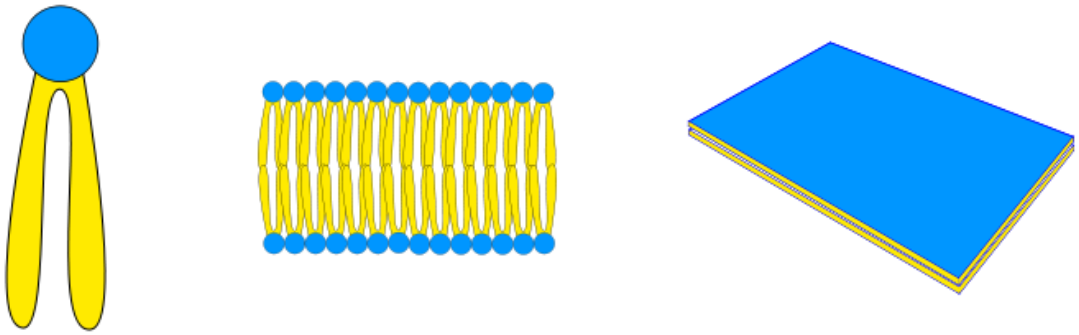

Figure 2.1: Illustration of the structure of a lipid molecule (on the left) and the bilayer structure of the biological membrane. The hydrophilic heads are shown in blue, while the hydrophobic tails are shown in yellow.

let us say that the geometry of the lipids plays an important role in the determination of the structures formed from their aggregation. Lipids with a relatively large head-to-tail size ratio resemble an inverted cone and naturally will pack into spherical aggregates. Lipids with smaller head-to-tail size ratio resemble cylindrical shape and typically aggregate into two-dimensional planar aggregates.

What's important for us is the fact that, from a mechanical perspective, the defining property of the bilayer is their relatively small thickness (typically few nanometers) compared to their large lateral size. As a result, we can treat the membrane as a two-dimensional sheet embedded in a three-dimensional space and examine the deformations that occur from stretching or bending of the planar sheet.

2.2 The Elastic Theory of Membranes

An accurate physical description of a membrane requires knowing how its energy changes upon various deformations of the membrane. Due to the absence of an external field in our work, any kind of translation or rotation of the membrane is not going to affect the total energy of the system, and since the thickness of the membrane is also neglected, we are left with the following three types of deformation: stretching, bending and shear, geometrically illustrated in Fig 2.2.

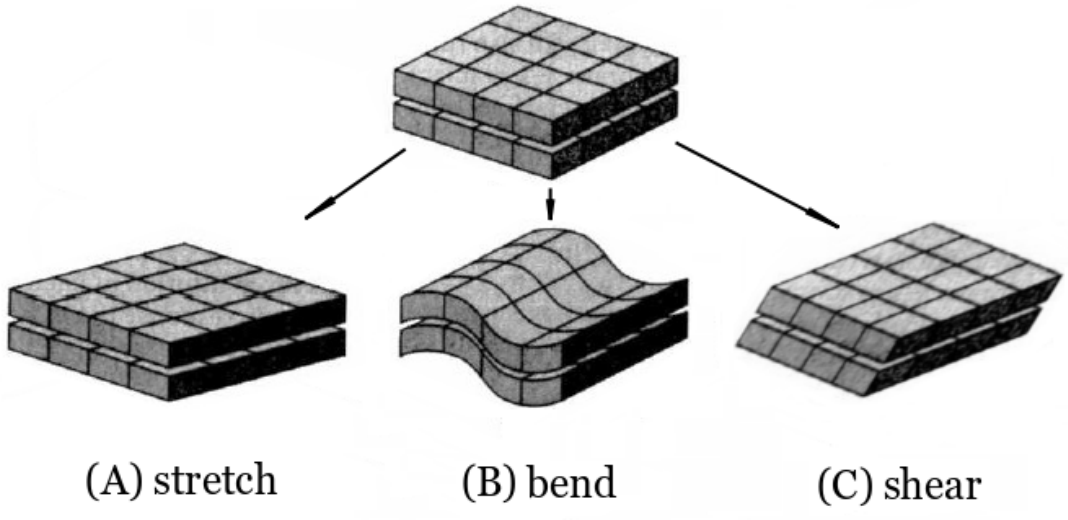

Figure 2.2: The geometry of three types of membrane deformations – stretch, bend and shear. Shear and thickness change are not considered in this work due to the fluidity of the membrane and negligible thickness. Image is taken from Ref. [106].

2.2.1 Stretching and Shearing

Fig. 2.2(A) illustrates one class of deformations when the area of the membrane is increased by an amount ΔA. We restrict such deformations to the membrane plane. Assume that in the absence of the external stress our membrane sheet has an area A_0, and we now stretch it to a size $A > A_0$. From the Taylor expansion we can write down the energy change to the lowest order as

$$E_{stretch} = \frac{1}{2} K_{stretch} \frac{(A - A_0)^2}{A_0}, \tag{2.1}$$

where the modulus $K_{stretch}$ is a proportionality constant and the additional $1/A_0$ is a convention. By definition, the lateral stress under which the membrane is when subjected to a strain (i.e. the tension Σ) is the derivative of the energy with respect to the area,

$$\Sigma = \frac{\partial E_{stretch}}{\partial A} = K_{stretch} \frac{A - A_0}{A_0} = K_{stretch} u, \tag{2.2}$$

where we have defined the dimensionless strain $u = A/A_0 - 1$. This essentially recovers Hooke's law for membrane stretching, where the stress is proportional to the strain through the stretching modulus $K_{stretch}$. The stretching modulus $K_{stretch}$ can been measured, for example, in micropipette experiments [80, 81]. In a typical experimental setup, part of

the surface of the membrane vesicle is being sucked into a much smaller micropipette, such that the vesicle is under tension. Subsequently the area change in the vesicle is calculated from geometric considerations based on the amount of membrane that ends up in the micropipette, and the tension can be inferred from the vesicle radius and the suction pressure through the Young-Laplace law. Through this method, the linear stress-strain relation is confirmed, and for phospholipid membranes the values of $K_{stretch}$ are found to be in the range of $230 - 290\ mN/m$ ($55 - 70\ k_BT/nm^2$).

As for the shear, pure lipid bilayer membranes are fluid and therefore cannot support a shear deformation. However, cell membranes are often attached to an elastic network, such as the one formed by spectrin in the case of red blood cells, which provides them with shear rigidity. We are however concerned only with fluid membranes, hence static shear is not a deformation that costs the fluid membrane energy in our case.

2.2.2 Bending

On a sufficiently large length scales membranes can be considered as essentially two-dimensional surfaces that can be bent into the third dimension. When a patch of a lipid bilayer is bent away from its flat, zero-energy configuration (assuming there is no spontaneous curvature), there is a re-arrangement of both headgroups and the tails of the lipids within the bilayer, which costs energy. Characteristically, weak bending is a deformation which costs significantly less energy than the stretching. Take, for example, a sheet of paper. Bending it is something we can do very easily (because the local volume strain is very small), while rupturing it by stretching is very difficult due to the very high stretching modulus. Let's see how this works out quantitatively.

Imagine a rectangular sheet of paper of side length L that's curved in one direction with a radius of curvature R (see Fig. 2.3(A)). Due to the deformation, one side of the paper is stretched, while the opposite side if compressed. This naturally requires that the middle region of the paper not be strained at all. Assuming that the paper material locally stretches following a simple elastic relation similar to the one we obtained in Eq. 2.1, we can write down the energy of the deformation as

$$E_{stretch} = \frac{1}{2} Y \frac{(V - V_0)^2}{V_0}, \tag{2.3}$$

where Y is the Younge's modulus and V is the volume of the paper. The total bending energy (per unit area) can be expressed as an integral over the volume of the paper (see

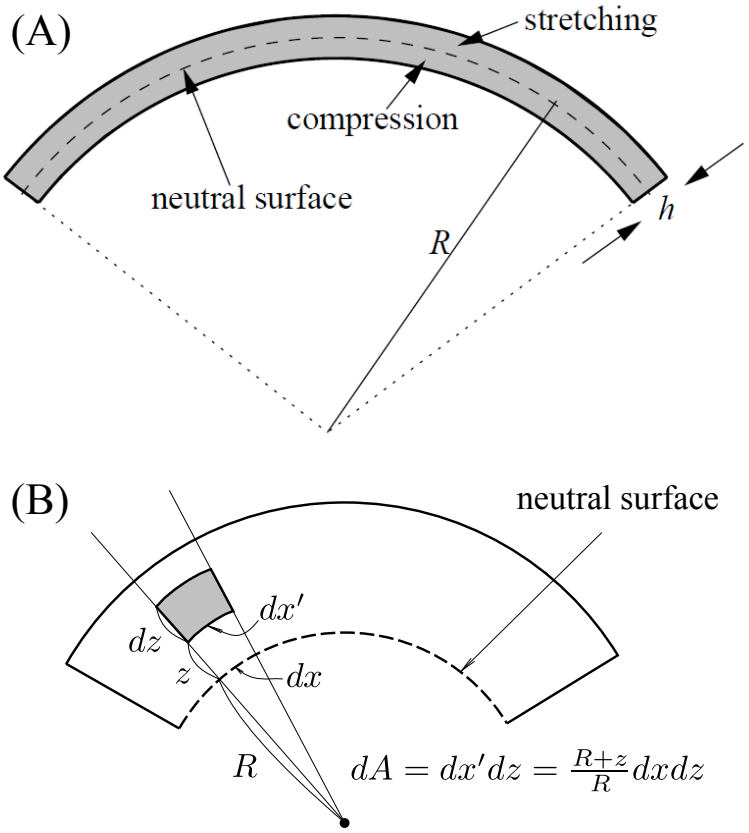

Figure 2.3: (A) Illustration of a piece of paper that's bent in one dimension. Due to the deformation the outer side is stretched, while the inner side is compressed. (B) shows the surface area element after the deformation. Image (A) is taken from Ref. [103].

Fig. 2.3(B))

$$e_{bend} = \frac{E_{bend}}{L^2} = \frac{1}{L^2}\int_0^L\int_0^L\int_{-h/2}^{h/2}\frac{1}{2}Y\frac{((1+z/R)dxdydz - dxdydz)^2}{dxdydz}$$
$$= \frac{1}{2}Y\int_{-h/2}^{h/2}\mathrm{d}z\left(\frac{z}{R}\right)^2 = \frac{1}{24}Y\frac{h^3}{R^2}. \tag{2.4}$$

Since in this approach bending of the sheet leads to uniaxial extension of the little volume elements within the membrane plane, we can express the three-dimensional Young's

modulus Y through the two-dimensional stretching modulus $K_{stretch}$, discussed in the previous section,

$$K_{stretch} = Yh, \tag{2.5}$$

which leads us to

$$e_{bend} = \frac{1}{24} K_{stretch} \left(\frac{h}{R}\right)^2. \tag{2.6}$$

The ratio h/R in the above expression is a very small quantity, even for a significant paper deformation. For a piece of paper bent into a circle with a radius of, say, 10 cm, assuming paper thickness of 0.1 mm, $(h/R)^2 \sim 10^{-6}$, so even for a large values of the stretching modulus $K_{stretch}$ the factor $(h/R)^2$ will reduce the bending energy significantly.

Introducing a bending modulus κ as

$$\kappa = \frac{1}{12} K_{stretch} h^2, \tag{2.7}$$

we can re-write the bending energy per unit area as

$$e_{bend} = \frac{1}{2} \kappa \frac{1}{R^2}, \tag{2.8}$$

hence the bending energy per unit area is locally proportional to the square of the curvature. It should be pointed out that the relation in Eq. 2.7 is an approximation which in general does not hold for the connection between the Young's modulus and bending modulus. Another correction could be introduced, however, that takes into account the fundamental difference between a membrane, which is a bilayer, and a paper sheet. Since the bilayer can be thought of as two elastic sheets that cannot transfer shear across its thickness (the sheets can laterally move with respect to each other with no difficulty), bending the bilayer is equivalent to bending two elastic sheets of half-thickness. Thus for two uncoupled elastic sheets the relation between stretching and bending modulus can be written as,

$$\kappa = \frac{1}{48} K_{stretch} h^2. \tag{2.9}$$

This relation can often be seen in literature used as a way to obtain approximate values for bending modulus κ by way of measuring $K_{stretch}$. Due to the approximations taken to derive the Eq. 2.9 it is only used to estimate the approximate values for the bending rigidity of the membrane. More reliable experimental approaches avoid using the relation between Young's modulus and bending modulus altogether and either directly measure the energy required to impose some bending, or monitor thermal fluctuations opposed by the bending rigidity.

We want to have at least a rough estimate for the bending modulus of membranes. The bending energy modulus κ has units of energy, and since the membrane is a structure which emerged from self-assembly, the characteristic energy for the system is k_BT. Because the membrane should have some stability, we expect the modulus to be somewhat bigger than thermal energy k_BT. Even with the approximation in Eq. 2.9, for a typical membrane thickness of $h = 5\ nm$, and Young's modulus $K_{stretch} = 10^7\ N/m^2$, we end up with

$$\kappa = \frac{1}{48} \times 10^7 N/m^2 \times (5nm)^3 \approx 10^{-19} J \approx 6k_BT, \tag{2.10}$$

which is fairly close to typical values for phospholipid membranes [3]. Typically a few tens of k_BT is often used in calculations with $20k_BT$ being used most often.

2.2.3 Surface Curvature

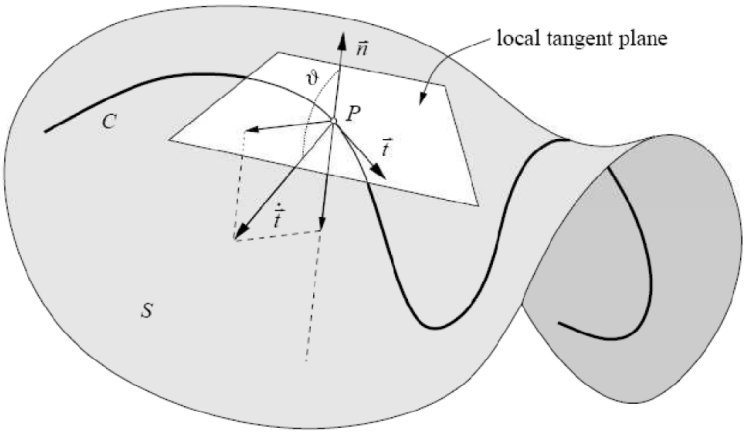

Figure 2.4: A space curve on a surface patch with the normal and tangent vectors shown. Image is taken from Ref. [104].

The relation in Eq. 2.4 is for the piece of paper that's bent only in one direction. The equation resembles the bending energy density for a worm-like chain [82], but we have to keep in mind that a polymer chain can locally be described only by a single radius of

curvature. The picture changes for membranes, since being a two-dimensional surface, the local curvature of the membrane cannot be so easily described, that is, if we take a curve on a surface, we cannot readily identify the curvature of the surface based on the curvature of the curve alone.

Consider a curve C defined on a surface patch S, that is parametrized through the arclength s as $\vec{r}(u^1(s), u^2(s))$ (see Fig. 2.4). At any point P on the curve, one can construct a tangent to the curve $\vec{t} = \dot{\vec{r}}$ and a principal normal vector of the curve $\vec{p} = \dot{\vec{t}}/|\dot{\vec{t}}| = \dot{\vec{t}}/\xi$, where the dot indicates derivative with respect to the arclength s. It can be shown that the local curvature of the curve, c_{curve}, multiplied by the scalar product between the two normal vectors, $\hat{p} \cdot \hat{n}$, where $\vec{n}$ is the local normal vector *of the surface* at point P, is a curvature that no longer depends on any property of the curve except its direction [83, 84]. The resulting curvature is called a directional curvature and we can write it as

$$c_{surface} = c_{curve}\hat{p} \cdot \hat{n} = c_{curve} \cos\theta, \tag{2.11}$$

where θ is the angle between the two normal vectors $\hat{p}$ and $\hat{n}$.

For a surface, however, we have an infinite number of directions at any given point, which means an infinite number of directional curvatures. It turns out that for any given point on the surface there exist two orthogonal directions in which the directional curvatures are extremal. These two directions are called principal directions, with corresponding curvatures called principal curvatures. Once we know these directions (and the corresponding curvatures), we can calculate every directional curvature by means of a formula derived first by Euler [84],

$$c(\alpha) = c_1 \cos^2(\alpha) + c_2 \sin^2(\alpha), \tag{2.12}$$

where α is the angle between the chosen direction and the principal direction belonging to one of the curvatures. It thus suffices to know only the two principal curvatures at at any point (and the direction of one) to have all the local information we need. Based on the two principal curvatures, two local quantities are usually used, the extrinsic curvature

$$K = c_1 + c_2, \tag{2.13}$$

and the Gaussian curvature

$$K_G = c_1 c_2. \tag{2.14}$$

2.2.4 The Helfrich Hamiltonian

In 1970 Canham proposed a generalization of the Eq. 2.8 in the following way,

$$e_{bend} = \frac{1}{2}\kappa_1 c_1^2 + \frac{1}{2}\kappa_2 c_2^2, \tag{2.15}$$

where c_1 and c_2 are the two principal curvatures of the membrane and κ_1 and κ_2 are the corresponding bending moduli [56]. For an isotropic system, which is the case for pure lipid bilayers, κ_1 and κ_2 are identical, since there is no directional preference in terms of the energy. In this case the bending energy density can be written as,

$$e_{bend} = \frac{1}{2}\kappa(c_1^2 + c_2^2) = \frac{1}{2}(K^2 - 2K_G). \tag{2.16}$$

In 1973 Helfrich proposed a slightly different energy density [49],

$$e_{bend} = \frac{1}{2}\kappa(c_1 + c_2 - c_0) + \bar{\kappa}c_1c_2 = \frac{1}{2}\kappa(K - c_0)^2 + \bar{\kappa}K_G, \tag{2.17}$$

where κ, $\bar{\kappa}$ and c_0 are material properties (constants) of the physical surface under consideration: the bending modulus, saddle-splay modulus, and spontaneous curvature, respectively. The bending modulus κ reflects the energy cost associated with driving the mean curvature of the membrane away from its preferred value, c_0, while the saddle-splay modulus $\bar{\kappa}$ reflects the cost of imposing the Gaussian curvature, c_1c_2, on the surface. Note that the introduction of these constants requires effective surface homogeneity, which is assumed throughout this work.

Interestingly, both equations in Eq. 2.16 and Eq. 2.17 are correct and this is due to the fact that both contain a term that involves the Gaussian curvature of the surface. For the total energy of the membrane, the energy density e_{bend} has to be integrated over the surface of the membrane, and from differential geometry we know that any surface integral of the Gaussian curvature K_G can be written as a boundary term and a topological constant (this is known as Gauss-Bonnet theorem [85, 86, 84]). This leads to a constant term in the energy expression after the integration for both of the expressions in Eq. 2.16 and Eq. 2.17 and thus is irrelevant in the energy calculations.

We therefore use the Helfrich energy for a symmetric membrane (i.e. no spontaneous curvature) in the following form,

$$E_{bend} = \int_{membrane} \mathrm{d}A \left(\frac{1}{2}\kappa K^2 + \bar{\kappa}K_G\right), \tag{2.18}$$

where the integration is done over the surface of the membrane, and $\mathrm{d}A$ is the area element on the membrane surface.

2.3 Geometrical Model

In this Thesis, we study the behavior of elastic membrane tubes in contact with two cylindrical nanoparticles from the theoretical point of view. Our arguments apply to any

particles that are rigid and cannot permeate the membrane on the experimentally relevant time scales, and thus, the membrane acts as flexible (but impenetrable) cylindrical tube for the adhered particles. In addition, we assume that the membrane exerts attractive forces onto these particles. In the following section we describe the coordinate system used in the problem of adhesion of two cylinders to a soft membrane tube. A segment of the system is sketched in Fig. 1.1(A), where the membrane tube is represented by the blue color and the rigid cylinders are represented by red. The sketch in Fig. 1.1(A) is only a portion of a much longer system, where we take the view that the membrane tube is connected to a remote reservoir that maintains a constant tension σ in the system, or alternatively, the considered membrane tube is only a segment of a much longer system where the radius is maintained constant at a certain value remotely. This is not uncommon in actual experimental setup where the extraction of a tubular membrane typically requires much larger vesicle to act as a "reservoir" for lipid supply [22, 23, 47, 24, 25, 26]. We also assume that the lateral size of the cylinders is much greater than their radius ($L/R \gg 1$) and ignore the end effects.

Due to the translational symmetry in the system along the z axis, we can reduce the problem to two dimensions and only consider the cross-section of the above system (shown in Fig. 1.1(B)), essentially considering the interaction of two rigid circles with a closed deformable curve. We assume a reflection symmetry of the membrane configuration about a mirror plane represented by the x-z axes, however no symmetry about the y-z plane is assumed, since we want to be able to take into account configurations that are not necessarily two-fold symmetric. With this in mind we only need to consider the upper-half ($y > 0$ range) of the membrane configuration in our calculations.

We will follow the so-called angle-arclength parametrization to describe our system. The shape of the non-adhered portion of the membrane can be specified in terms of polar coordinates $[r(s), \theta(s)]$, shown in Fig. 1.1(B), where we choose to parametrize the profile of the membrane by its arclength s, changing from $s = 0$, where the membrane detaches from the cylinder, to the point $s = S$, where the membrane intersects with the x-axis. The shape itself can be described by specifying the angle $\psi(s)$ defined as the angle between the shape line and the original (undisturbed) membrane tube (dashed circle in Fig. 1.1(B)). From Fig. 2.5(A) it is easy to notice that the two variables $[r(s), \theta(s)]$ are related to $\psi(s)$ at any point s by the following two equations

$$\frac{dr(s)}{ds} = \sin\psi(s), \tag{2.19}$$

$$r(s)\frac{d\theta(s)}{ds} = \cos\psi(s). \tag{2.20}$$

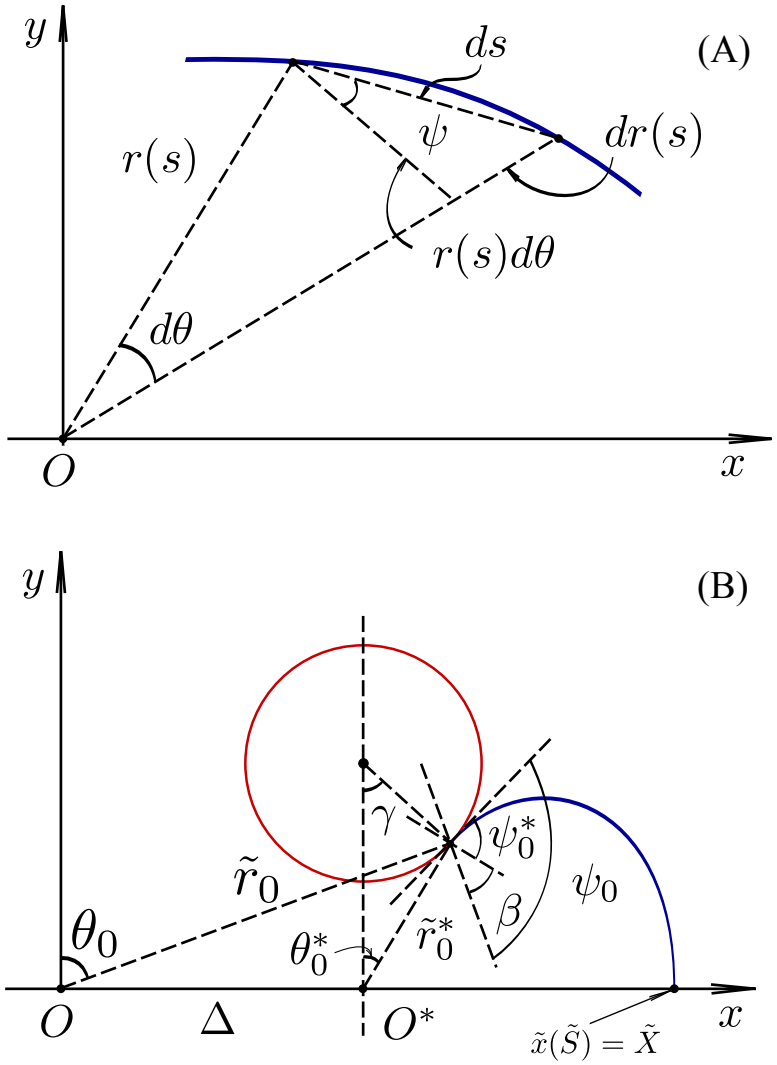

Figure 2.5: (A) Sketch illustrating the relation between the polar coordinates and the angle-arclength parametrization. (B) The shifted coordinate system and the change in relevant parameters for the initial conditions.

The relation to Cartesian coordinate system is straightforward

$$x(s) = r(s)\sin\theta(s), \tag{2.21}$$

$$y(s) = r(s)\cos\theta(s), \tag{2.22}$$

where in order to simplify the numerical procedure of dealing with asymmetric membrane shapes (negative γ contact angles in Fig. 2.5(B)) we choose to place the origin of the coordinate system at point O, that is shifted by the amount Δ from the more intuitive point O' located on the axis connecting the centres of the cylinders (see Fig. 2.5(B)). The choice of Δ is arbitrary as long as the symmetry point at $s = S$ stays on one side of the point O for the range of contact angles γ that we are interested in. By doing so we avoid the numerical complications that arise in the requirement to implement different boundary conditions depending on the location of the symmetry point at $s = S$ relative to the center of the coordinate system O.

Using the angle-arclength parametrization allows us to take into account the possible "over-wraps" of the membrane and is not restricted to small membrane deformations, where the membrane shape is usually described by specifying the height h as a function of the coordinate x, for example (so-called Monge-like parametrization). The angle-arclength parametrization has been used extensively in similar systems recently [87, 30, 8, 9, 88, 37, 29, 10, 51].

2.4 Free Energy of the Free Portion of the Membrane

In this coordinate system the square bending curvature of the membrane at any point s can be written as [84],

$$K^2 = \left[\frac{d\psi}{ds} - \frac{d\theta}{ds}\right]^2, \tag{2.23}$$

and thus, assuming zero spontaneous curvature, the Helfrich free energy for the free part of the membrane becomes

$$F = L\int_0^S ds\left\{\frac{\kappa}{2}\left[\frac{d\psi}{ds} - \frac{\cos\psi}{r}\right]^2 + \sigma\right\}, \tag{2.24}$$

where L is the length of the cylinders, κ is the bending energy and σ is the surface tension of the membrane surface. The integral is taken from $s = 0$, where the membrane detaches

from the cylinder to the point $s = S$, where the membrane intersects with the reflection plane on the x-axis shown in Fig. 2.5(B).

Let's see how this formalism applies for a simple case of a free, tubular membrane centred at O. Since the membrane is undisturbed from its original shape, $\psi(s) = 0$ at any point on the membrane and thus, from Eq. 2.19, for any s we can write

$$\frac{dr(s)}{ds} = \sin\psi(s) = 0.$$

The solution to the above equation is $r(s) = r_0$ for any s, which is what we expect for an undisturbed tubular membrane. The curvature is then constant and is equal to $1/r_0$ everywhere along the membrane. Thus, following Eq. 2.24, we can then write the free energy for the freely standing tubular membrane as

$$F_0 = 4L \int_0^S ds \left\{ \frac{\kappa}{2} \frac{1}{r_0^2} + \sigma \right\}.$$

After the integration and a little re-arrangement we obtain

$$F_0 = 4\kappa L \left\{ \frac{\pi}{4r_0} + \frac{\sigma\pi r_0}{2\kappa} \right\}.$$

The above free energy can be minimized with respect to the size of the membrane tube r_0

$$\frac{\partial F_0}{\partial r_0} = 4\kappa L \left\{ -\frac{\pi}{4r_0^2} + \frac{\sigma\pi}{2\kappa} \right\} = 0,$$

$$r_0^2 = \frac{\kappa}{2\sigma}, \tag{2.25}$$

which is the square radius of the undisturbed membrane tube. This is a known result [30, 27, 28, 51], which indicates that the radius of a freely standing membrane tube is dependent only on the physical characteristics of the membrane, namely the surface tension σ and the bending rigidity κ. For typical values of $\kappa \approx 40\ pN\ nm$ and $\sigma \approx 0.05\ pN/nm$, one finds $r_0 \approx 20\ nm$, which appears to be a good estimate. Using r_0 as a basic length-scale, for the rest of this work, we will replace all the relevant parameters with their dimensionless counterparts

$$\tilde{s} = \frac{s}{r_0}, \tag{2.26}$$

$$\tilde{r} = \frac{r}{r_0}, \tag{2.27}$$

$$\tilde{F} = \frac{F r_0}{\kappa L}. \tag{2.28}$$

The general expression for the free energy in Eq. 2.24 can be then written in terms of the new re-scaled parameters

$$\tilde{F}[\psi(\tilde{s}), \psi'(\tilde{s})] = \int_0^{\tilde{S}} d\tilde{s} \left\{ \frac{1}{2} \left[\frac{d\psi}{d\tilde{s}} - \frac{\cos\psi}{\tilde{r}} \right]^2 + \frac{1}{2} \right\}. \tag{2.29}$$

Notice how the free energy above is a functional of the membrane shape $\psi(\tilde{s})$, thus if the membrane shape is known (i.e. $\psi(\tilde{s})$ is explicitly given), we can find the corresponding energy by simply integrating the above expression along the shape. However, in our problem the membrane shape that minimizes the energy is not known *a-priori*, so for a given configuration of the system, our first task is to determine the equilibrium shape of the membrane by minimizing its energy. This leads to the following functional minimization problem: *For a given radius of the cylinders $\tilde{R}$, contact angle γ and separation distance between the cylinders $\tilde{D}$, find the curve $\psi = \psi(\tilde{s})$ for which the functional in Eq. 2.29 has an extremum, where the admissible curves satisfy the boundary conditions*

$$\psi(0) = \gamma, \tag{2.30}$$

$$\psi(\tilde{S}) = 0, \tag{2.31}$$

and are such that the following condition is satisfied,

$$\int_0^{\tilde{S}} \frac{\cos\psi}{\tilde{r}} \, d\tilde{s} = \frac{\pi}{2} - \theta_0, \tag{2.32}$$

where γ is the contact angle and θ_0 is the angle between $r(s)$ and the y-axis at $\tilde{s} = 0$ (see Fig. 2.5(B)). The two boundary conditions in Eq. 2.30 and Eq. 2.31 are imposed to ensure that the membrane is smooth both at the detachment point $\tilde{s} = 0$, and at the symmetry point $\tilde{s} = \tilde{S}$ (otherwise the bending energy would go to infinity there). The constraint in Eq. 2.32 restrains the symmetry point at $\tilde{s} = \tilde{S}$ to remain on the x-axis while looking for shapes that minimize the energy. The angle $\theta_0 = \theta(0)$ in Eq. 2.32 is the angle between the vertical axis and the line connecting the center of the coordinate system to the $\tilde{s} = 0$ point (see Fig. 1.1(B)) and can be easily determined based on the geometrical configuration of the system (i.e. parameters $\tilde{R}, \tilde{D}$ and γ). In functional minimization this is known as an isoperimetric problem and the solution can be found by incorporating the constraint in Eq. 2.32 into our functional with the use of a Lagrange multiplier. To put it formally, we

can say that there exists a constant λ_θ such that the solution we are looking for, $\psi = \psi(\tilde{s})$ is an extremum of the following functional

$$\int_0^{\tilde{S}} \left\{ \frac{1}{2} \left[\frac{d\psi}{d\tilde{s}} - \frac{\cos\psi}{\tilde{r}} \right]^2 + \frac{1}{2} + \lambda_\theta \frac{\cos\psi}{\tilde{r}} \right\} d\tilde{s}. \tag{2.33}$$

The solution hence satisfies the Euler-Lagrange equation

$$\frac{\partial L}{\partial \psi} = \frac{d}{d\tilde{s}} \left(\frac{\partial L}{\partial \psi'} \right), \tag{2.34}$$

where the Lagrange function L is the integrand of the functional in Eq. 2.33,

$$L = \frac{1}{2} \left[\frac{d\psi}{d\tilde{s}} - \frac{\cos\psi}{\tilde{r}} \right]^2 + \frac{1}{2} + \lambda_\theta \frac{\cos\psi}{\tilde{r}}. \tag{2.35}$$

The two derivatives in the Euler-Lagrange equation can be found

$$\frac{\partial L}{\partial \psi} = \left[\frac{d\psi}{d\tilde{s}} - \frac{\cos\psi}{\tilde{r}} \right] \frac{\sin\psi}{\tilde{r}} - \lambda_\theta \frac{\sin\psi}{\tilde{r}} \tag{2.36}$$

and

$$\frac{\partial L}{\partial \psi'} = \left[\frac{d\psi}{d\tilde{s}} - \frac{\cos\psi}{\tilde{r}} \right]. \tag{2.37}$$

Thus

$$\frac{d}{d\tilde{s}} \frac{\partial L}{\partial \psi'} = \psi'' - \frac{-\sin\psi\psi'\tilde{r} - \tilde{r}'\cos\psi}{\tilde{r}^2} = \psi'' + \frac{\sin\psi\psi'}{\tilde{r}} + \frac{\tilde{r}'\cos\psi}{\tilde{r}^2}, \tag{2.38}$$

and the Euler-Lagrange equation becomes,

$$\psi' \frac{\sin\psi}{\tilde{r}} - \frac{\cos\psi\sin\psi}{\tilde{r}^2} - \lambda_\theta \frac{\sin\psi}{\tilde{r}} = \psi'' + \frac{\sin\psi\psi'}{\tilde{r}} + \frac{\tilde{r}'\cos\psi}{\tilde{r}^2}, \tag{2.39}$$

$$\psi'' + \frac{2\sin\psi\cos\psi}{\tilde{r}^2} + \lambda_\theta \frac{\sin\psi}{\tilde{r}} = 0. \tag{2.40}$$

In order to solve this second-order differential equation numerically, we can treat it as a system of two first-order differential equations by introducing a new function $\phi(\tilde{s}) = d\psi/d\tilde{s}$. With other relevant functions in the system, we end up with the following system of first-order differential equations

$$\begin{cases} \dfrac{d\psi}{d\tilde{s}} = \phi(\tilde{s}) \\ \dfrac{d\phi}{d\tilde{s}} = -\dfrac{\lambda_\theta \sin\psi(\tilde{s})}{\tilde{r}(\tilde{s})} - \dfrac{2\sin\psi(\tilde{s})\cos\psi(\tilde{s})}{\tilde{r}(\tilde{s})^2} \\ \dfrac{d\tilde{r}}{d\tilde{s}} = \sin\psi(\tilde{s}) \end{cases} \tag{2.41}$$

Within this treatment, mathematically the function $\theta(\tilde{s})$ is not directly involved. The integration to find $\theta(s)$ is however straightforward once the function $\psi(\tilde{s})$ is known,

$$\theta(\tilde{s}) = \int_0^{\tilde{s}} \frac{\cos\psi(\tilde{t})}{\tilde{r}(\tilde{t})}\, dt. \tag{2.42}$$

Three initial conditions are required for the three functions in the above system to solve the equations numerically. From the diagram shown in Fig. 2.5(B), based on geometric considerations, one can write down the following initial conditions

$$\begin{cases} \psi_0 = \psi(0) = \psi_0^* + \beta \\ \phi_0 = \phi(0) = \xi \\ \tilde{r}_0 = \tilde{r}(0) = \sqrt{(\Delta + \tilde{R}\sin\gamma)^2 + (\tilde{D} - \tilde{R}\cos\gamma)^2} \end{cases} \tag{2.43}$$

where

$$\psi_0^* = \gamma + \arcsin\left[\frac{\tilde{R}\sin\gamma}{\sqrt{\tilde{D}^2 + \tilde{R}^2 - 2\tilde{D}\tilde{R}\cos\gamma}}\right],$$

β is an angle (see Fig. 2.5(B)) which, through $\tilde{r}_0$, is dependent only on the shift Δ

$$\beta = \arccos\left[\frac{\tilde{D} - \tilde{R}\cos(\gamma)}{\tilde{r}_0}\right] - \arcsin\left[\frac{\tilde{R}\sin(\gamma)}{\tilde{r}_0}\right],$$

and ξ is an unknown variable that we have introduced, since we don't really know the value of $\dot{\psi}(0)$. The initial value for $\theta(\tilde{s})$ can also be determined through the following equation

$$\theta_0 = \theta(0) = \arcsin(\tilde{R}\sin\gamma/\tilde{r}_0^*). \tag{2.44}$$

At this point we have two unknown variables λ_θ and ξ that, regardless of their values, will give us a solution that is an extrema of the functional in Eq. 2.29. However our task is to find such a pair that the constraint given by Eq. 2.32 and the boundary value $\psi(\tilde{S}) = 0$ are both satisfied. Numerically this could be done by so-called shooting method (see Appendix A for a detailed description of the numerical implementation) and we can obtain a solution that, for fixed physical parameters of the system $\tilde{R}$ and $\tilde{D}$, fixed contact angle γ, *and fixed curve length* $\tilde{S}$, minimizes the free energy of free portion of the membrane. In other words, the free energy minimum produced through this method is dependent on four variables, $\tilde{F}_f = \tilde{F}_f(\tilde{R}, \tilde{D}, \gamma, \tilde{S})$. The next step would then be to minimize it with respect

to the length of the membrane $\tilde{S}$, as done for example in [51], but this doesn't prove to be a good approach in the numerical implementation for the following two reasons. First, for a certain range of contact angles γ we observe multiple solutions corresponding to the same length of the membrane shape $\tilde{S}$ and second, inevitably there is going to be a contact angle, where the solution that minimizes the free energy happens to be at the lowest value the arclength $\tilde{S}$ can possibly attain (this would happen for contact angle $\gamma = -\pi/2$, for example, where the membrane shape that minimizes the energy is simply a straight line wrapping around both cylinders). For these reasons the numerical implementation of the minimization process becomes unreasonably challenging.

To avoid this difficulty, we choose to introduce an extra constraint into the system. Now for fixed $\tilde{R}$, $\tilde{D}$ and γ, we want to solve the exact same problem, but with an extra requirement for a fixed symmetry point $\tilde{x}_s = \tilde{x}(\tilde{S}) = \tilde{X}$ (see Fig. 2.5(B)). With this in mind we have to "relax" the requirement for fixed $\tilde{S}$ and now have to find three unknown variables λ_θ, ξ and $\tilde{S}$ such that the constraint given by Eq. (2.32), the boundary value $\psi(\tilde{S}) = 0$, and the new constraint $\tilde{x}(\tilde{S}) = \tilde{X}$ are all satisfied. Numerically this can be implemented with a three-dimensional shooting method. After the procedure the free energy of the free part of the membrane can be written as a function of four variables, $\tilde{F}_f = \tilde{F}_f(\tilde{R}, \tilde{D}, \gamma, \tilde{X})$ and the subsequent minimization with respect to the symmetry point $\tilde{X}$ presents no difficulty, since we know for certain that fixed value of $\tilde{X}$ produces a unique solution. The resulting free energy $\tilde{F}_f(\tilde{R}, \tilde{D}, \gamma)$ is then used in the next sections for the numerical analysis of the system.

2.5 Free Energy of the Adhered Portion of the Membrane

For the adhered state, the membrane segment adjacent to the colloid surface can experience a variety of intramolecular forces, such as van der Waals, electrostatic, and steric interactions. In order to have a bound state, the effective interaction potential must exhibit a minimum at a finite distance, which is usually in the range of the order of a few nm. Typically the size of the membrane vesicles varies from 0.1 to 10 μm [50], while the size of the tubes varies from 10 nm for tense membranes ($\sigma = 10^{-3} Nm^{-1}$, $\kappa = 10 k_B T \sim 4 \times 10^{-20} J$) and 100 nm for floppy ones ($\sigma = 10^{-5} Nm^{-1}$) [27]. Since we are primarily interested in the overall shape of the vesicle, we will ignore spatial variations on the scale of the potential range and replace the microscopic interaction potential for the adhesion by an effective (short-ranged) negative energy w per unit-area. The same parameter was introduced in related systems recently [50, 87, 7, 8, 9, 29, 10]. Thus, for contact angle γ, taking into

account the bending and tension energies of the membrane, we can write the free energy for the adhered portion of the membrane (for one half of the system only) for both cylinders as

$$F = 2L \int_0^S ds \left\{ \frac{\kappa}{2} \frac{1}{R^2} + \sigma \right\} + 2L\gamma R w,$$

which, after introducing a rescaled adhesion energy $\tilde{w} = w r_0^2/\kappa$, and using the rescaled variables in Eqs. 2.26 - 2.28 can be written as

$$\tilde{F}_c = \gamma \tilde{R} (\frac{1}{\tilde{R}^2} + 1 + 2\tilde{w}). \tag{2.45}$$

Since we do not assume symmetry with respect to the y-axis (see Fig. 2.6(B)) we need to consider the contributions from two parts of the membrane, corresponding to two different contact angles γ_1 and γ_2, when calculating the total energy of the system. The total reduced energy for the system can then be written as

$$\begin{aligned} \Delta\tilde{F}(\tilde{R}, \tilde{D}, \tilde{w}, \gamma_1, \gamma_2) = \tilde{F}_f(\tilde{R}, \tilde{D}, \gamma_1) + \tilde{F}_c(\tilde{R}, \tilde{D}, \tilde{w}, \gamma_1) + \\ \tilde{F}_f(\tilde{R}, \tilde{D}, \gamma_2) + \tilde{F}_c(\tilde{R}, \tilde{D}, \tilde{w}, \gamma_2) - 2\pi, \end{aligned} \tag{2.46}$$

where the index f indicates the free portion of the membrane and the index c indicates the contact portion of the membrane (see Fig. 2.6(B)). The last term in the above equation is the rescaled energy of the original undisturbed membrane tube $\tilde{F}_0$,

$$\begin{aligned} F_0 &= L \int_0^{2\pi r_0} ds \left\{ \frac{\kappa}{2} \frac{1}{r_0^2} + \sigma \right\}, \\ F_0 &= 2\pi r_0 L \left\{ \frac{\kappa}{2} \frac{1}{r_0^2} + \sigma \right\}, \\ \frac{F_0}{\kappa L} &= \pi r_0 \left\{ \frac{1}{r_0^2} + \frac{2\sigma}{\kappa} \right\}, \\ \frac{F_0}{\kappa L} &= \pi r_0 \left\{ \frac{1}{r_0^2} + \frac{1}{r_0^2} \right\}, \\ \tilde{F}_0 &= \frac{F_0 r_0}{\kappa L} = 2\pi. \end{aligned} \tag{2.47}$$

The total energy difference in Eq. 2.46 is then used in further analysis of the system discussed in the sections below. We organize the rest of the work in the following way: for a given relative size of the rigid cylinders $\tilde{R}$, as a first step we want to fix the separation

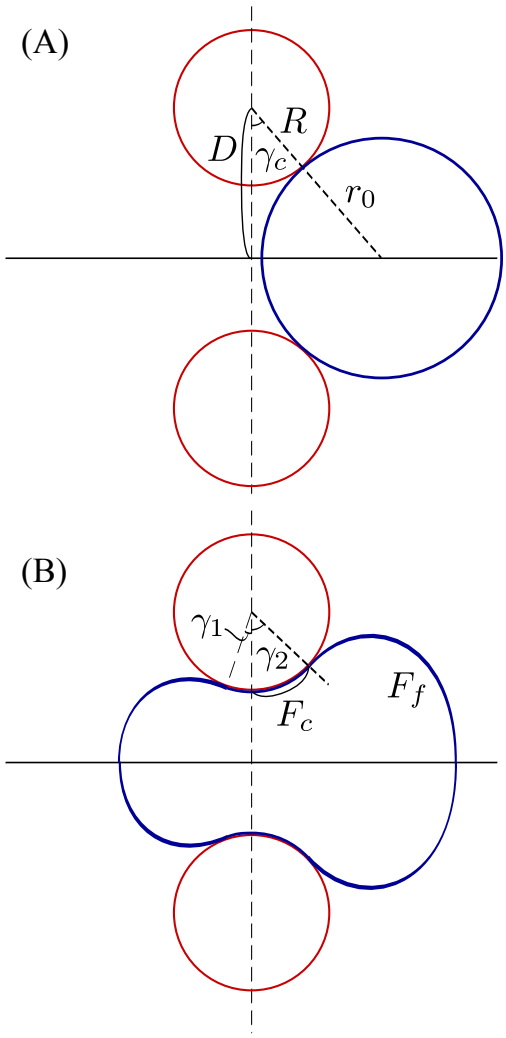

Figure 2.6: (A) A sketch illustrating the non-adhered state of the membrane tube in which the two contact angles are equal in magnitude and opposite in sign, $\gamma_1 = -\gamma_c$ and $\gamma_2 = \gamma_c$. The adhered state is sketched in (B) with free and contact portions of the membrane shown. In this case, contributions from two different portions of the membrane with corresponding γ_1 and γ_2 contact angles have to be considered.

between the cylinders $\tilde{D}$ and see how the system behaves when the adhesion between the cylinders and the membrane increases gradually. We then repeat the process for a range of values of the separation distance between the cylinders and for each value of $\tilde{R}$, map out a phase diagram in the $(\tilde{w}, \tilde{D})$ phase space. This process is done for a range of values of $\tilde{R}$ and the different characteristics for the membrane configurations are discussed. As a next step, we look into the free energy dependence on the separation distance between the cylinders for fixed values of adhesion energy $\tilde{w}$, for each fixed $\tilde{R}$. This allows us to minimize the free energy with respect to the separation distance between the cylinders and generalize the results to a single phase diagram in $(\tilde{w}, \tilde{R})$ phase space.

2.6 Numerical Implementation

The first step in every analysis in this work is to numerically compute and list in a table the values of the function $\tilde{F}_f(\tilde{R}, \tilde{D}, \gamma)$ for a range of contact angles γ for each $(\tilde{R}, \tilde{D})$ pair that we consider. In this section, we describe the general outline for the numerical implementation of the process without going too much into detail about the methods themselves. The numerical methods used in this work are described in detail in Appendix A.

For given $\tilde{R}$ and $\tilde{D}$, we first pick a starting angle (usually $\gamma = \pi$) and "guess" a triple of the unknown parameters (λ_θ, ξ and $\tilde{S}$) that, through the ODEs in Eq. 2.41, will lead to a solution that roughly (i.e. within $\delta = 0.1$ precision) satisfies the desired boundary conditions

$$\begin{aligned} \psi(\tilde{S}) &= 0, \\ \int_0^{\tilde{S}} \frac{\cos\psi}{\tilde{r}}\, d\tilde{s} &= \frac{\pi}{2} - \theta_0, \\ x(\tilde{S}) &= \tilde{X}. \end{aligned} \tag{2.48}$$

Notice that while the exact location of the intersection point $\tilde{X}$ is irrelevant, it is just fixed at a certain value. The numerical integration of the system of equations in Eq. 2.41 is done using 4-th order Runge-Kutta method, which takes in the initial values for all the functions in Eq. 2.41 at $\tilde{s} = 0$ and returns the values at $\tilde{s} = \tilde{S}$ by simply marching along the parameter $\tilde{s}$ in the interval $[0, \tilde{S}]$ (for the detailed description see Appendix A). In general, since our choice of the initial values was somewhat random, after the integration, we are pretty much guaranteed not to have the desired boundary values at the other end of the boundary $\tilde{s} = \tilde{S}$ and thus we need to refine our guess to better match the desired boundary values at $\tilde{s} = \tilde{S}$. In essence, this is a multidimensional root-finding problem,

where we need to find the adjustments of our free parameters (λ_θ, ξ and $\tilde{S}$), that will zero the discrepancies of the functions $\psi(\tilde{s})$, $\tilde{x}(\tilde{s})$ and $\int_0^{\tilde{S}}(\cos\psi/\tilde{r})\,d\tilde{s}$ at the other boundary $\tilde{s} = \tilde{S}$. This is implemented using the Newton-Raphson method generalized for three dimensions. The procedure described above is usually referred to as "shooting", since by picking initial values for the three unknown variables, we are essentially aiming at the target (desired) boundary values and (based on the outcome) systematically improve out "shots" by adjusting the aim.

The shooting method described above produces a solution for the ODEs in Eq. 2.41 that, for fixed $\tilde{R}$, $\tilde{D}$ and contact angle γ, satisfies the boundary conditions that we impose in Eqs. 2.48. Hence, after the procedure the free energy of the free part of the membrane can be written as a function of four variables, $\tilde{F}_f = \tilde{F}_f(\tilde{R}, \tilde{D}, \gamma, \tilde{X})$, where $\tilde{X}$ is an arbitrary point we chose for the intersection point on the axis x and γ was initially chosen to be π. Our next step is to minimize the free energy with respect to the symmetry point $\tilde{X}$, and thus find the membrane shape that minimizes the free energy of the free part of the membrane for given $\tilde{R}$, $\tilde{D}$ and γ only. This could be done by first bracketing the minimum and then narrowing the width of the bracket until the desired precision is reached. We implement this using golden section search method described in the Appendix A. As a result of the last step, we now know the shape (and the free energy) of the free part of the membrane that minimizes the free energy for given parameters in the system: $\tilde{F}_f = \tilde{F}_f(\tilde{R}, \tilde{D}, \gamma)$.

Since we are interested in a range of contact angles γ, we then gradually decrease the value of γ (starting from the initial value π that we chose) with a certain step-size, dependent on the region that we are interested in ($\delta\gamma = 0.0001$ to $\delta\gamma = 0.000000001$ around the region where we expect weak wrapping). At each step, the solution for the previous (neighbouring) contact angle γ is taken as an initial guess for the current one and the whole procedure is repeated. An example free energy curve produced by this method is shown in black in Fig. 2.7(A) for $\tilde{R} = 0.55$ and $\tilde{D} = 0.65$. In the positive γ region, the shape of the membrane is labelled with (a) in Fig. 2.7(A), while in the negative γ region the shape is labelled with (b). The membrane shape (b) is quite distorted with a lot of membrane material pulled in, while in the negative region of the contact angles one would expect a membrane shape similar to the shape (c) in Fig. 2.7(A), which has both less membrane material and less overall curvature. In order to check if this is only a local minimum, we repeat the procedure this time taking as a starting point $\gamma = -\pi$ with a "guess" shape similar to the shape (c) in Fig. 2.7(A). Gradually increasing the values for γ produces the blue free energy curve shown in Fig. 2.7(A). Indeed, the results show that two solutions exist for the same contact angle γ (shapes (b) and (c) in Fig 2.7(A)) in the negative γ region.

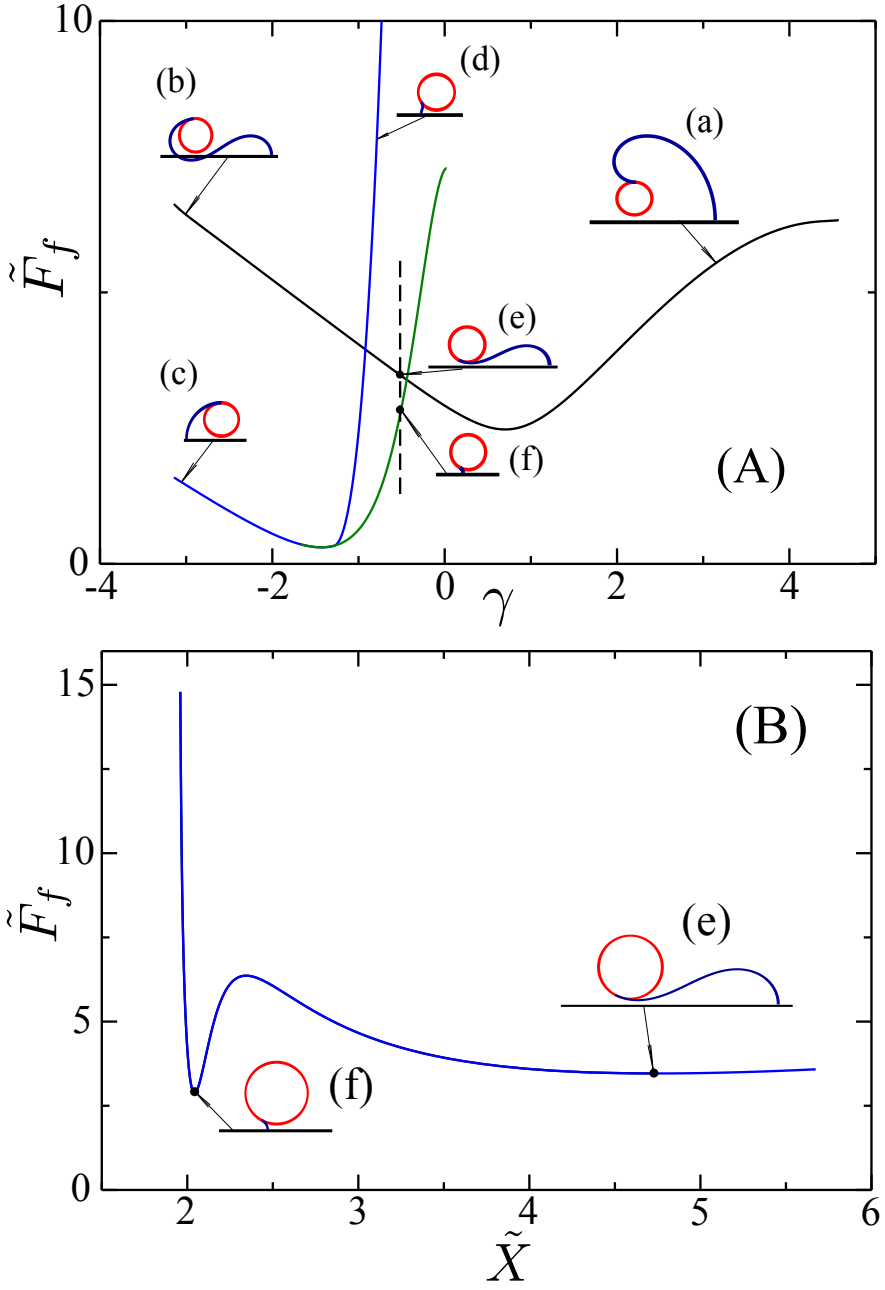

Figure 2.7: (A) The free energy curves as a function of the contact angle γ for $\tilde{R} = 0.55$ and $\tilde{D} = 0.65$. (B) The free energy for the contact angle $\gamma = -0.5$ as a function of the intersection point $\tilde{X}$.

Yet another solution exists in the negative region of the contact angles γ. In order to see this, we pick a certain contact angle γ (in this example $\gamma = -0.5$, shown by the dashed line in Fig. 2.7(A)) and look into the free energy dependence on the intersection point $\tilde{X}$ for constant contact angle γ. Numerically this is implemented in a similar way, but this time $\tilde{R}$, $\tilde{D}$ and γ are all kept constant, while the intersection point $\tilde{X}$ is gradually decreasing with a certain step-size. At each step the solution from the previous step is taken as an initial guess for the next one. For $\tilde{R} = 0.55$ and $\tilde{D} = 0.55$, the resulting free energy curve for $\gamma = -0.5$ is shown in Fig. 2.7(B). As we can see two minima exist, one for a relatively large value of the intersection point $\tilde{X}$ (corresponding to shape (e) in Fig. 2.7(B)) and another one corresponding to a smaller value of $\tilde{X}$ (shape (f) in Fig. 2.7(B)). Once the second minimum is identified, we pick the solution with smaller free energy as our starting point and "walk" up and down from $\gamma = -0.5$ tracing the green free energy line in Fig. 2.7(A).

Chapter 3

Results and Discussion

3.1 Second-Order Adhesion Transition from Desorption to Weak Wrapping

For fixed $\tilde{R}$ and $\tilde{D}$, increasing the adhesion energy $|\tilde{w}|$ induces adhesion transition between the desorption state, where the rigid cylinders and the membrane tube have no contact, to a weak-wrapping state, where the configuration resembles the one shown in Fig. 3.1 with a small wrapping area formed by the angles γ_1 and γ_2. Weak wrapping configuration is characterized by two contact angles γ_1 and γ_2 that are opposite in sign and are only slightly different in absolute value. In this section we show that this phase transition can be determined analytically without invoking the numerical analysis described in the sections below. In order to do this, as a first step we want to show that in weak adhesion, to the linear order of the membrane shape $\psi(\tilde{s})$, the contribution of the energy of the free membrane $\tilde{F}_f(\tilde{R}, \tilde{D}, \gamma)$ to the total reduced energy of the system is simply $\psi(0)$, which is the angle between the membrane shape and the original reference tube at the contact point $\tilde{s} = 0$. Fig. 3.1 shows an exaggerated sketch of a weakly adhered membrane tube with two separate portions of the membrane labelled correspondingly with indices I and II. Notice that for the simplicity of the calculations that follow, we slightly deviate from the notation we have used so far and use indices I and II instead of 1 and 2. The difference is that the angles γ_I and γ_{II} are defined as the angles at which the detachment point is located with respect to the axis connecting the center of the cylinder with the center of the reference membrane tube (see Fig. 3.1), while the angles γ_1 and γ_2 are the angles the detachment

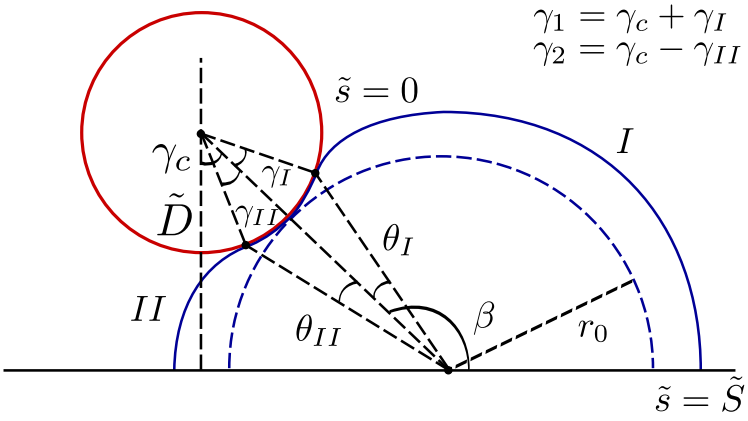

Figure 3.1: A sketch illustrating the weakly-adhered configuration of the membrane.

point makes with respect to the vertical axis. It is easy to notice that

$$\begin{aligned} \gamma_1 &= \gamma_c + \gamma_I, \\ \gamma_2 &= \gamma_c - \gamma_{II}, \end{aligned} \tag{3.1}$$

where

$$\gamma_c = \arccos\left(\frac{D}{R + r_0}\right), \tag{3.2}$$

is the angle between the axis connecting the center of the cylinder to the center of the reference membrane tube and the vertical axis (see Fig. 3.1).

We will treat the two contributions of the two sides of the membrane separately. For the free portion of the membrane we re-write the energy in Eq. 2.29 in the following way

$$\tilde{F}_f = \int_0^{\tilde{S}} d\tilde{s} \left\{ \frac{1}{2}\left(\frac{d\psi}{d\tilde{s}}\right)^2 - \frac{d\psi}{d\tilde{s}}\frac{\cos\psi}{\tilde{r}} + \frac{1}{2}\left(\frac{\cos\psi}{\tilde{r}}\right)^2 + \frac{1}{2} \right\}. \tag{3.3}$$

In a desorbed state, the membrane shape is circular, with no contact between the membrane and the cylinders (the dashed blue line in Fig. 3.1). The angle β, which is the angle between the horizontal axis and the line connecting the center of the cylinder and the membrane tube, can be determined from the geometry of the system and is dependent only on the relative size of the cylinders $\tilde{R}$ and their separation distance $\tilde{D}$. Corresponding to a circular shape, the zeroth order of a weakly deformed membrane shape, for branch I we can write $\psi_0(\tilde{s}) = \psi_0 = 0$ and $\tilde{r}_0 = 1$. To the zeroth order the membrane energy

is simply the rescaled energy of the segment of the membrane tube corresponding to the angle β shown in Fig. 3.1, $\tilde{F}_f \approx \beta$. When the membrane shape makes weak distortion adhering to the cylinder with a contact angle γ_I, to the first-order correction we can write the shape as

$$\psi = \psi_0 + \lambda\phi. \tag{3.4}$$

With this,

$$\cos\psi = \cos(\psi_0 + \lambda\phi) = \cos\psi_0 - \lambda\phi\sin\psi_0 \simeq 1, \tag{3.5}$$

and, from Eq. 2.19

$$d\tilde{r} = \sin\psi d\tilde{s} = \sin(\psi_0 + \lambda\phi)d\tilde{s}, \tag{3.6}$$

$$\tilde{r}(\tilde{s}) \simeq \tilde{r}_0 + \lambda\int\phi\, d\tilde{s}. \tag{3.7}$$

Using the Eqs. 3.4, 3.5 and 3.7, we can re-write the Eq. 3.3 as

$$\tilde{F}_f = \int_0^{\tilde{S}} d\tilde{s}\left\{\frac{1}{2}\left(\frac{d\psi_0}{d\tilde{s}} + \lambda\frac{d\phi}{d\tilde{s}}\right)^2 - \left(\frac{d\psi_0}{d\tilde{s}} + \lambda\frac{d\phi}{d\tilde{s}}\right)\frac{1}{1+\lambda\int\phi\, d\tilde{s}}\right\} + \\ + \int_0^{\tilde{S}} d\tilde{s}\left\{\frac{1}{2}\left(\frac{1}{1+\lambda\int\phi\, d\tilde{s}}\right)^2 + \frac{1}{2}\right\}. \tag{3.8}$$

Keeping only the terms of linear order in λ and dropping all the higher order terms, we obtain

$$\tilde{F}_f = \int_0^{\tilde{S}} d\tilde{s}\left\{-\lambda\frac{d\phi}{ds}(1-\lambda\int\phi\, d\tilde{s}) + \frac{1}{2}(1-\lambda\int\phi\, d\tilde{s})^2 + \frac{1}{2}\right\} \tag{3.9}$$

$$= \int_0^{\tilde{S}} d\tilde{s}\left\{-\lambda\frac{d\phi}{ds} + \frac{1}{2} - \lambda\int\phi\, d\tilde{s} + \frac{1}{2}\right\} \tag{3.10}$$

$$= \int_0^{\tilde{S}} d\tilde{s}\left\{-\lambda\frac{d\phi}{ds} + 1 - \lambda\int\phi\, d\tilde{s}\right\}. \tag{3.11}$$

Since the $\tilde{s} = 0$ point is fixed, and $\tilde{s} = \tilde{S}$ point has to lie on the horizontal axis, we can use the constraint

$$\int_0^{\tilde{S}} d\tilde{s}\frac{\cos\psi}{\tilde{r}} = \beta - \theta_I, \tag{3.12}$$

which, using the Eqs. 3.5 and 3.7, can be written as

$$\int_0^{\tilde{S}} d\tilde{s}(1-\lambda\int\phi\, d\tilde{s}) = \beta - \theta_I, \tag{3.13}$$

With this the Eq. 3.11 can be written as

$$\tilde{F}_f = \int_0^{\tilde{S}} d\tilde{s} \left\{ -\lambda \frac{d\phi}{ds} \right\} + \beta - \theta_I. \tag{3.14}$$

Thus to the linear order of $\psi(\tilde{s})$ the free energy of the free part of the membrane branch I can be written as

$$\tilde{F}_f = \psi(0) - \psi(\tilde{S}) + \beta - \theta_I. \tag{3.15}$$

The term $\psi(\tilde{S})$ in the above equation is zero due to the requirement that membrane shape is smooth at the symmetry axis (otherwise the bending energy would go to infinity there), and it is easy to show that

$$\psi(0) = \gamma_I + \theta_I, \tag{3.16}$$

which leaves us with the following expression for the free energy of the free part of the membrane for branch I

$$\tilde{F}_f^I = \gamma_I + \beta. \tag{3.17}$$

Repeating the same procedure for the membrane branch II, we can similarly show that to the linear order of $\psi(\tilde{s})$, for the free energy of the membrane branch II the following expression is true

$$\tilde{F}_f^{II} = \gamma_{II} + \pi - \beta. \tag{3.18}$$

Using the contributions from these two free parts of the membrane in Eqs. 3.17 and 3.18, along with the free energy for the adhered portions of the membrane, to the linear order of $\psi(\tilde{s})$, we can write down the total reduced energy of the system in Eq. 2.46 as

$$\Delta\tilde{F} = \tilde{F}_f^I + \tilde{F}_c^I + \tilde{F}_f^{II} + \tilde{F}_c^{II} + O(\gamma_I^2) + O(\gamma_{II}^2) \tag{3.19}$$

$$\begin{aligned} \Delta\tilde{F} = 2(\gamma_I + \beta) + \gamma_I \tilde{R} \left(\frac{1}{\tilde{R}^2} + 1 + 2\tilde{w} \right) + 2(\gamma_{II} + \pi - \beta) + \\ \gamma_{II} \tilde{R} \left(\frac{1}{\tilde{R}^2} + 1 + 2\tilde{w} \right) - 2\pi + O(\gamma_I^2) + O(\gamma_{II}^2), \end{aligned} \tag{3.20}$$

where the 2π term is the rescaled energy of the undisturbed membrane tube.

$$\Delta\tilde{F} = 2\gamma_I + \gamma_I \tilde{R} \left(\frac{1}{\tilde{R}^2} + 1 + 2\tilde{w} \right) + 2\gamma_{II} + \gamma_{II} \tilde{R} \left(\frac{1}{\tilde{R}^2} + 1 + 2\tilde{w} \right) + O(\gamma_I^2) + O(\gamma_{II}^2), \tag{3.21}$$

$$\Delta\tilde{F} = \left[\tilde{R} \left(\frac{1}{\tilde{R}^2} + 1 + 2\tilde{w} \right) + 2 \right] \gamma_I + \left[\tilde{R} \left(\frac{1}{\tilde{R}^2} + 1 + 2\tilde{w} \right) + 2 \right] \gamma_{II} + O(\gamma_I^2) + O(\gamma_{II}^2). \tag{3.22}$$

This expansion allows us to identify two order parameters, $\sqrt{\gamma_I}$ and $\sqrt{\gamma_{II}}$, in comparison with the standard Ginzburg-Landau free energy expansion of a second-order phase transition (note that $\tilde{w} \leq 0$). As the adhesion energy $\tilde{w}$ is small, the free energy has a minimum at $\gamma_I = \gamma_{II} = 0$, indicating no contact between the cylinders and the membrane, hence the system is in a desorption state. Beyond a critical $\tilde{w}_c$ energy, the first two terms in Eq. 3.22 become negative at a non-zero, small γ_I and γ_{II} (the energy minima splits into four, two of which are not physical, and the other two represent adhesion from left or right sides correspondingly). The critical point is determined by the requirement that one of the coefficients (same in our problem) of the γ term vanishes, which can be solved to yield

$$\tilde{R}\left(\frac{1}{\tilde{R}^2} + 1 + 2\tilde{w}_c\right) + 2 = 0, \tag{3.23}$$

$$\tilde{w}_c = -\frac{1}{2}\left(1 + \frac{1}{\tilde{R}}\right)^2. \tag{3.24}$$

Although we have determined the second-order transition boundary analytically using a small-angle approximation, we can also determine the transition numerically on the basis of the analysis of the look-up table of the function $\tilde{F}_f(\tilde{R}, \tilde{D}, \gamma)$. For a given $\tilde{R}$ and each fixed $\tilde{D}$ we solve the minimization problem described in Section 2.4, and numerically compute and list in a table the function $\tilde{F}_f(\tilde{R}, \tilde{D}, \gamma)$ for values of γ spanning the range $[\gamma_t, -\pi]$ with a step-size of $\delta\gamma = 0.0001$. The upper boundary γ_t is numerically determined terminal angle (usually $\gamma_t > \pi$) at which the membrane intersects with either itself (see Fig. 3.2(c1),(c2) or Fig. 3.3(c1),(c2), for example) or the rigid cylinders (see Fig. 3.3(c3),(c4) or Fig. 3.4(c1)-(c3)). Around the regions where weak-adhesion is expected, the step-size of the angle γ is refined sometimes up to 0.00000001 precision, according to necessity. This is done in order to see the weak-adhesion state, since wrapping angles can be significantly small. As a result, for given $\tilde{R}$ and $\tilde{D}$, the look-up table contains a list of free energy minima for the free portion of the membrane, for a range of contact angles γ.

Using this table, we then search for a minimum of the function $\Delta\tilde{F}(\tilde{R}, \tilde{D}, \tilde{w}, \gamma_1, \gamma_2)$ as a function of γ_1 and γ_2 for given values of $\tilde{R}$ and $\tilde{D}$ gradually increasing the adhesion energy $|\tilde{w}|$. Note that the procedure of finding the free energy for the contact portion does not require solving an optimization problem, since the shape of the adhered membrane is already known. Numerically, for each fixed value of $\tilde{w}$, a loop runs through the look-up table for the values of contact angles $\gamma_1 = 0.0$ to $\gamma_1 = \gamma_t$ (one of the contributing parts of the membrane has to have a positive contact angle) and another nested loop runs from $\gamma_2 = \pi$ to $\gamma_2 = -\gamma_1$ essentially tracing a free energy surface in (γ_1, γ_2) space. Notice that the $\gamma_2 = -\gamma_1$ limit comes from the requirement that the membrane shape does not self-intersect in the weak-wrapping regime, which results in the cut-out (lower-left) corners in

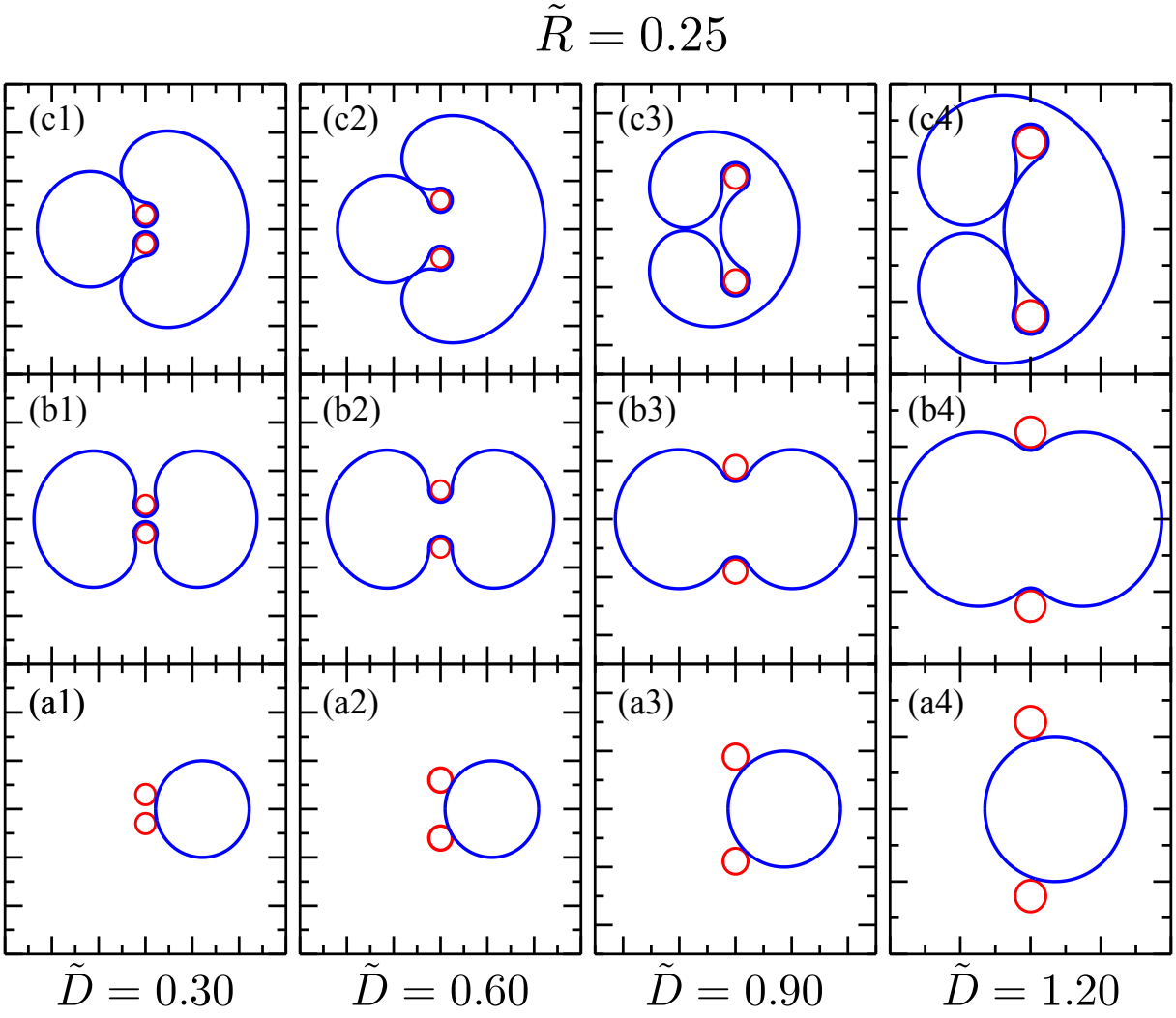

Figure 3.2: Cross-section profiles of the tubular membrane (blue) configurations around the rigid cylinders (red) in a weak-wrapping state (labelled (a)), symmetric-wrapping state (labelled (b)) and the asymmetric-wrapping state (labelled (c)) for $\tilde{R} = 0.25$ and $\tilde{D} = 0.30$, 0.60, 0.90 and 1.20 correspondingly from left to right.

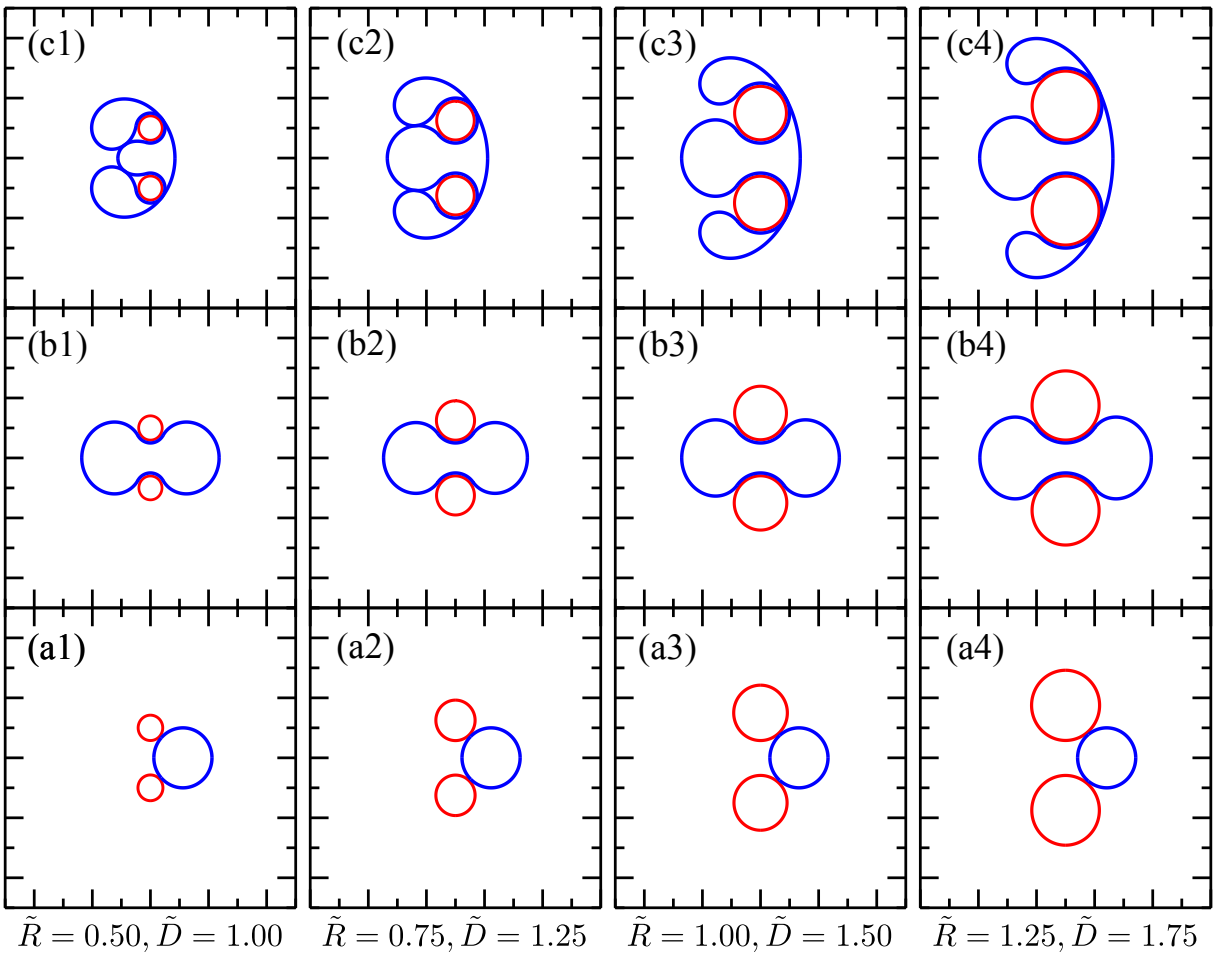

Figure 3.3: Cross-section profiles of the tubular membrane configurations around the rigid cylinders in a weak-wrapping state (configurations (a)), symmetric-wrapping state (labelled (b)) and the asymmetric-wrapping state (labelled (c)) for ($\tilde{R} = 0.50$, $\tilde{D} = 1.00$), ($\tilde{R} = 0.75$, $\tilde{D} = 1.25$), ($\tilde{R} = 1.00$, $\tilde{D} = 1.50$) and ($\tilde{R} = 1.25$, $\tilde{D} = 1.75$).

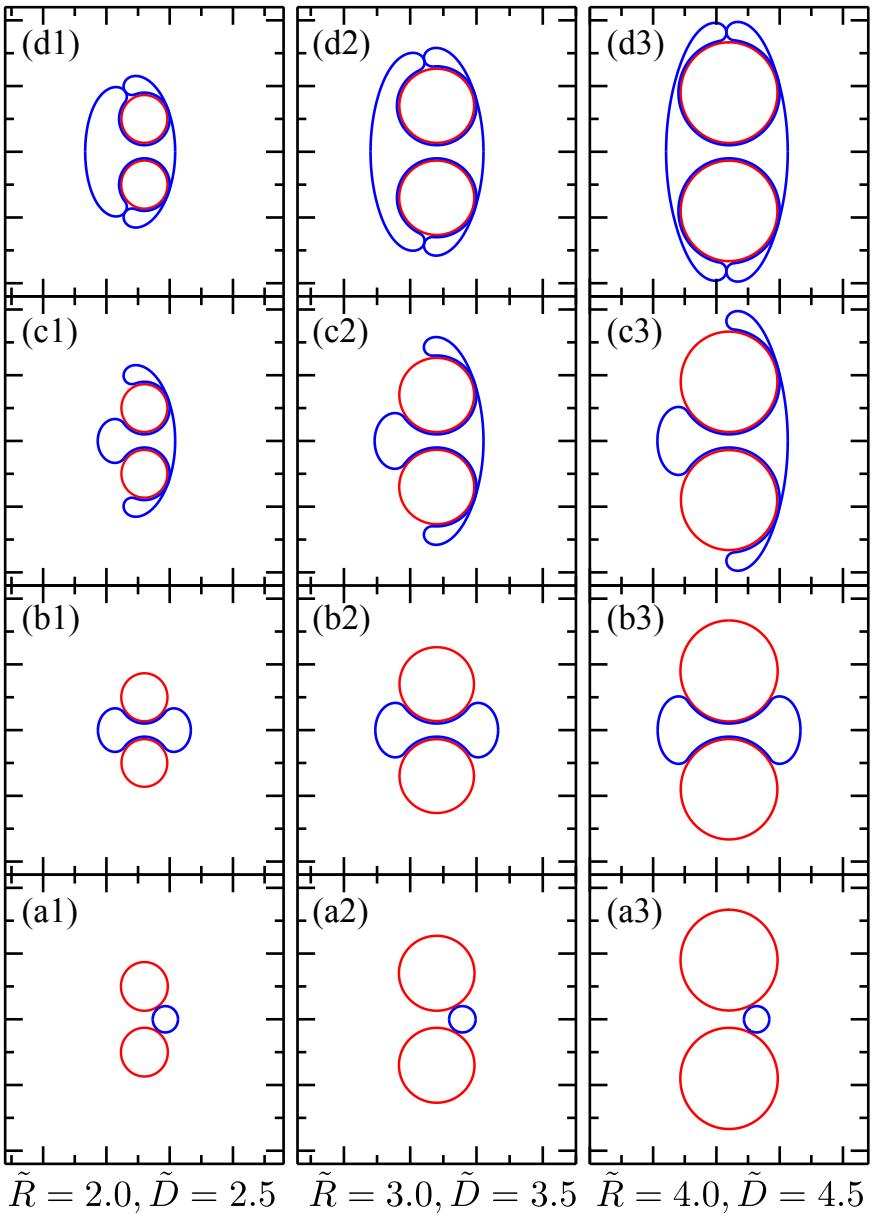

Figure 3.4: Cross-section profiles of the tubular membrane configurations around the rigid cylinders in a weak-wrapping state (labelled (a)), symmetric-wrapping state (labelled (b)), asymmetric-wrapping state (labelled (c)) and the closure state (labelled (d)) for ($\tilde{R} = 2.00$, $\tilde{D} = 2.50$), ($\tilde{R} = 3.00$, $\tilde{D} = 3.50$) and ($\tilde{R} = 4.00$, $\tilde{D} = 4.50$).

the example contour plots shown in Fig. 3.6. The top right cut-out corners are due to the same requirement, but correspond to the significant curvature regime where the membrane touches itself from the opposing sides of the cylinders.

As a result of the numerical search described above, at small values of $\tilde{w}$, the only free energy minimum we observe has a value of 0 and is observed for contact angles γ_1 and γ_2 that are equal in magnitude to the angle γ_c, but opposite in sign, which indicates no contact between the membrane and the cylinders (see Fig. 2.6(A)). In all calculations that we performed the match was within the 0.00001 range from the theoretical value in Eq. 3.2 indicating perfect correspondence to the analytical result. At a critical point $\tilde{w}_c$ the observed minimum becomes weakly negative with small deviations of the angles γ_1 and γ_2 from the no-contact value γ_c, indicating weak wrapping adhesion between the membrane and the tubes. Due to the tedious nature of the search (the data has to be refined to fine precision), we run the same procedure for the second order transition points for several values of $\tilde{R}$ only for selected points in our diagrams to check the consistency with the theoretical result. For all the calculations performed (select points ranging from $\tilde{R} = 0.05$ to $\tilde{R} = 4.0$) we observe the second order transition for values of adhesion energy $\tilde{w}$ within 0.00001 precision from the predicted theoretical result. Example transition boundaries for numerically performed calculations are shown in Fig 3.5 for $\tilde{R} = 0.25$ and $\tilde{R} = 0.35$. The dashed black line in the diagrams represents the theoretical curve for the second-order transition points. Maroon diamonds are the numerically determined second order transition points, while the blue squares are the numerically determined first-order transition points from weakly-wrapped state to intermediate-wrapping state.

3.2 First-Order Transition from Weak Wrapping to Symmetric Wrapping

At fixed $\tilde{R}$ and $\tilde{D}$, increasing adhesion energy beyond the second-order adhesion transition $\tilde{w}_c$ causes more distortion of the membrane, but the entire membrane conformation remains approximately circular. Characteristically the weakness of the distortion of the membrane is indicated by the smallness of the wrapping area formed by the angles γ_1 and γ_2. As $\tilde{w}$ reaches another transition point $\tilde{w}_p$, a first-order transition from the weak-wrapping state to an intermediate, symmetric-wrapping state occurs. This state is characterized by two-fold symmetry of the membrane shape, with the wrapping occurring on both sides of the adhering cylinders. In this configuration a major portion of the membrane is "sucked in" in between the cylinders and the distortion from the circular shape is quite significant resembling a barbell shape.

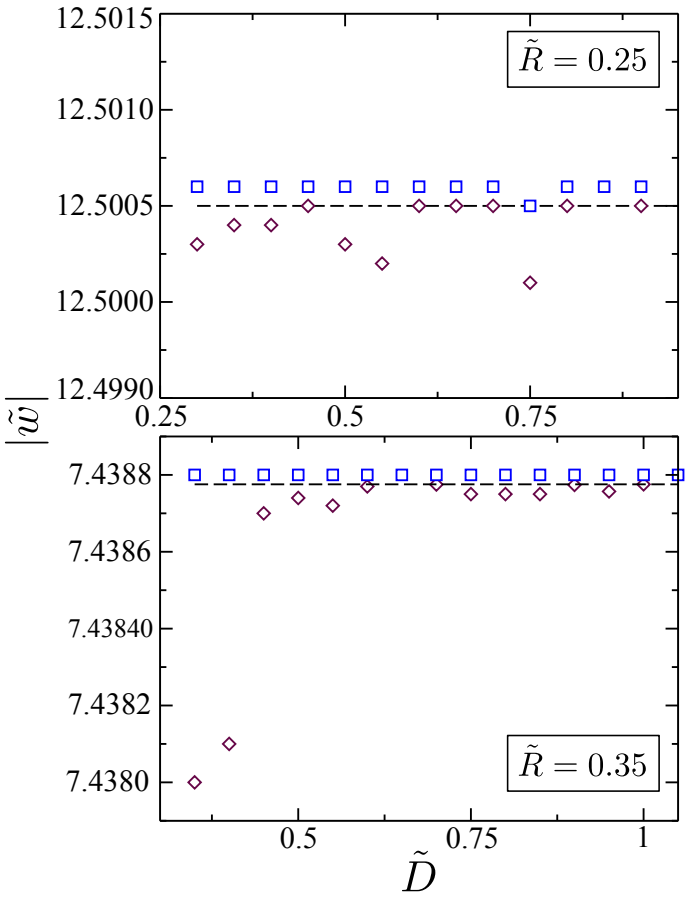

Figure 3.5: Phase boundaries between the no-wrapping state, weak-wrapping state and the symmetric-wrapping state for $\tilde{R} = 0.25$ and $\tilde{R} = 0.35$. Maroon diamonds indicate the numerically determined second-order transition points from free to a weak-wrapping state, the blue squares indicate the first-order transition points from weak-wrapping state to symmetric-wrapping state and the dashed line represents the analytical line for the second order boundary.

There is no analytic solution for this phase boundary, and we determine the transition points numerically on the basis of the analysis of the look-up table of the function $\tilde{F}_m(\tilde{R}, \tilde{D}, \gamma)$. The process is similar to one described in the previous chapter, where a numerical search is performed for a minimum of the function $\Delta\tilde{F}(\tilde{R}, \tilde{D}, \tilde{w}, \gamma_1, \gamma_2)$ as a function of γ_1 and γ_2 for given values of $\tilde{R}$ and $\tilde{D}$ gradually increasing the adhesion energy $|\tilde{w}|$ now beyond the second order adhesion point. With increasing adhesion energy we see that in the weak-wrapping state the wrapping area gradually increases, but the shape remains approximately circular. Near the wrapping transition $\tilde{w}_p$, two minima are typically observed: one corresponding to a shallow-wrapping state (for example shapes see Fig. 3.2(a1)-(a4), 3.3(a1)-(a4) and 3.4(a1)-(a3)) and the other to the partially wrapped state (Fig. 3.2(b1)-(b4), 3.3(b1)-(b4) and 3.4(b1)-(b3)). At the transition point the two minima have an equal free energy value separated by an energy barrier. Three typical contour plots for the free energy surfaces $\Delta\tilde{F}(\tilde{R}, \tilde{D}, \tilde{w}, \gamma_1, \gamma_2)$ are shown in Fig. 3.6 for $\tilde{R} = 2.00$ and $\tilde{D} = 2.50$ for the adhesion energies $|\tilde{w}| = 1.125$, $|\tilde{w}| = 1.570$ and $|\tilde{w}| = 1.805$ (the transition points where two minima have an equal value). Note that in the contour plots in Fig. 3.6, the free energy is plotted against the two contact angles γ_1 and γ_2 and the cut-out edges are due to the requirement of the membrane not to intersect with itself, both in the weak-wrapping regime (lower left corners) and the significant curvature regime (top-right corners), where the membrane is highly deformed.

The first-order transition points corresponding to this transition are indicated by blue squares on the phase diagrams in Fig. 3.7 - 3.17. In the phase diagrams shown in Figs. 3.7-3.9 (corresponding to $\tilde{R} = 0.30$, $\tilde{R} = 1.00$ and $\tilde{R} = 3.50$) we show three typical detailed phase diagrams with numerically obtained shapes overlayed on top to give an idea of the configurations in different phase regions. For all the phase diagrams, the no-wrapping state is shown in blue color, the symmetric wrapping state is shown in green, the asymmetric wrapping state is shown in red and the closure states are shown in purple. The numerically obtained weakly adhered shapes and the symmetric-wrapping shapes are also shown for $\tilde{R} = 0.25$ and various distances $\tilde{D} = 0.30, 0.60, 0.90, 1.20$ in Fig. 3.2 (labelled a and b correspondingly), as well as for various increasing values of $\tilde{R}$ in Figs. 3.3 and 3.4. We observe that for all values of $\tilde{R}$ and $\tilde{D}$, the symmetric-wrapping state shapes are characteristically similar, with more "squeezed" shape profile for smaller separation between the cylinders. For $\tilde{D} < 1 + \tilde{R}$, which is where the two cylinders are separated exactly by the diameter of the original reference tube, the adhesion energy values at which the transition from weak to partial wrapping occurs are equal in value and are within $\Delta\tilde{w} = 0.0001$ range from the second-order adhesion transition points. For separation distances larger than the diameter of the original reference tube, the membrane shape deformation needed to achieve the partially wrapped state is much more significant (since it's not in contact with cylinders

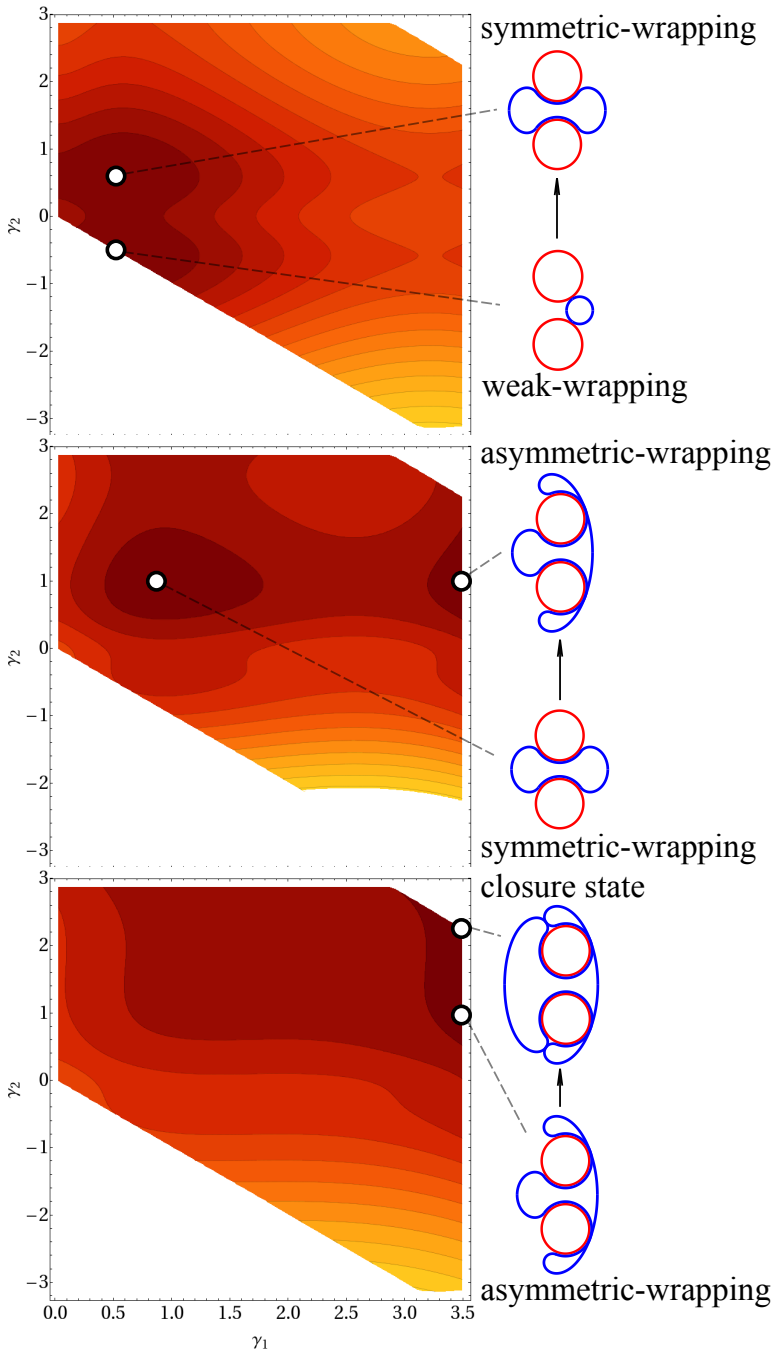

Figure 3.6: $\Delta\tilde{F}(\tilde{R}, \tilde{D}, \tilde{w}, \gamma_1, \gamma_2)$ free energy contour plots as a function of the two contact angles γ_1 and γ_2 for $\tilde{R} = 2.00$ and $\tilde{D} = 2.50$, at the three first-order transition points.

any more, and no second-order transition to weak-wrapping is observed), and thus the transition occurs at a larger values of $\tilde{w}$ to compensate for the deformation of the original reference tube. This can be seen in the phase diagrams where the blue squares start to rise for increasing separation between the cylinders. Notice that this is the case for all the values of $\tilde{R}$ considered, however some of the diagrams do not show this, as the separation distance is considered only up to the $\tilde{D} = 2$ point for those.

3.3 First-Order Transitions from Symmetric Wrapping to Asymmetric Wrapping and to Closure States

Beyond the critical point $\tilde{w}_p$, where the transition between weak-wrapping state and symmetric-wrapping occurs, increasing the adhesion energy even more causes more distortion of the membrane shape, but the whole configuration remains symmetric with respect to both x and y axes. As the adhesion energy approaches another critical point, $\tilde{w}_w$, we observe another first-order transition, which is characterised with a break in symmetry about the y-axis (see Fig. 3.2(c1)-(c1), 3.3(c1)-(c4) and 3.4(c1)-(c3) for example shapes). Numerical determination of the $\tilde{w}_w$ transition points exactly replicates the one described in previous chapters, where again near the transition point two minima are observed, one corresponding to the state with symmetric shapes (similar to the one shown in Fig. 3.2(b1)-(b4)), and another minimum corresponding to asymmetric-wrapping configuration (shapes similar to one in Fig. 3.2(c1)-(c4)). At the transition point $\tilde{w}_w$ the two minima have an equal value for the free energy, beyond which the asymmetric-wrapping configuration becomes energetically favourable. A typical contour plot for the free energy surface for this transition is shown in Fig 3.6 for $\tilde{R} = 2.00$ and $\tilde{D} = 2.50$ near the transition point $\tilde{w}_w = 1.570$, where two minima can be observed separated by an energy barrier.

Closer examination of the configurations reveals interesting characteristics for the asymmetric wrapping state. For example, for relatively small values of $\tilde{R}$, the asymmetric-wrapping configuration completely encapsulates the cylinders with the membrane in configurations resembling shapes shown in Fig. 3.3(c1)-(c2). Further increase in the adhesion energy does not affect the configuration of the membrane around the cylinders and, for the cylinder radius range $\tilde{R} = 0.05$ to $\tilde{R} = 1.75$, we observe only three phase transitions for the fixed separation between the cylinders: a second-order phase transition from desorped state to a weakly adhered state, a first-order transition from weakly adhered state to a symmetric, partially wrapped state, and another first-order transition from symmetric-

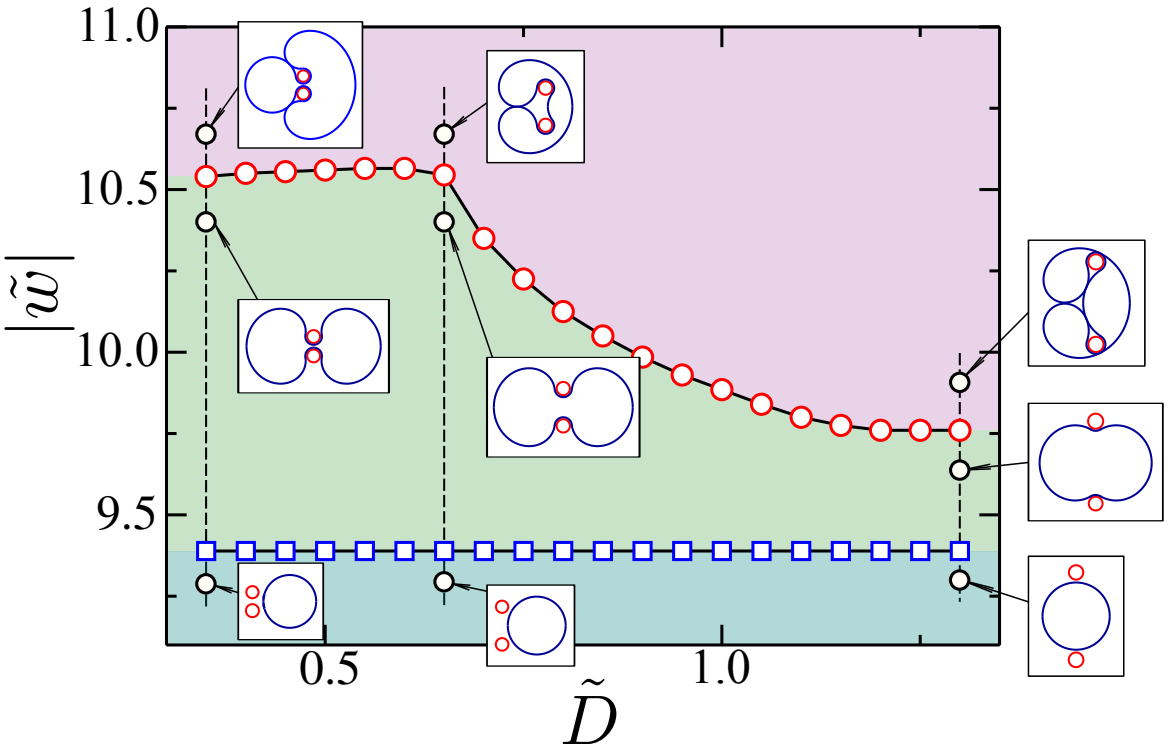

Figure 3.7: Phase diagram for $\tilde{R} = 0.30$ indicating the boundaries between no-wrapping state (blue), symmetric-wrapping state (green) and the asymmetric-wrapping state (red). The first order transition points from weak-wrapping state to the symmetric-wrapping state are shown in blue squares, while the symmetric-to-asymmetric wrapping first-order transition points are shown in red circles. The second-order boundary between the no-wrapping state and the weak-wrapping state is not shown (see text).

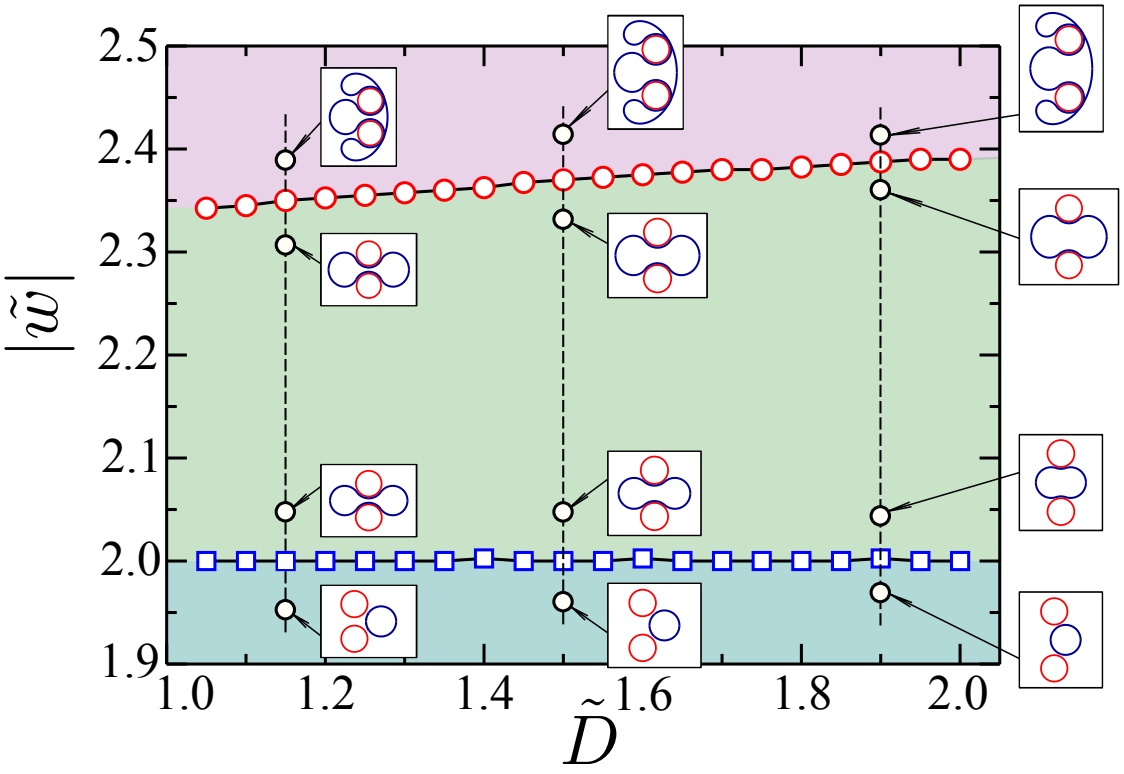

Figure 3.8: Phase diagram for $\tilde{R} = 1.00$ indicating the boundaries between no-wrapping state (blue), symmetric-wrapping state (green) and the asymmetric-wrapping state (red). The first order transition points from weak-wrapping state to the symmetric-wrapping state are shown in blue squares, while the symmetric-to-asymmetric wrapping first-order transition points are shown in red circles. The boundary between no-wrapping state and the weak-wrapping state is not shown (see text).

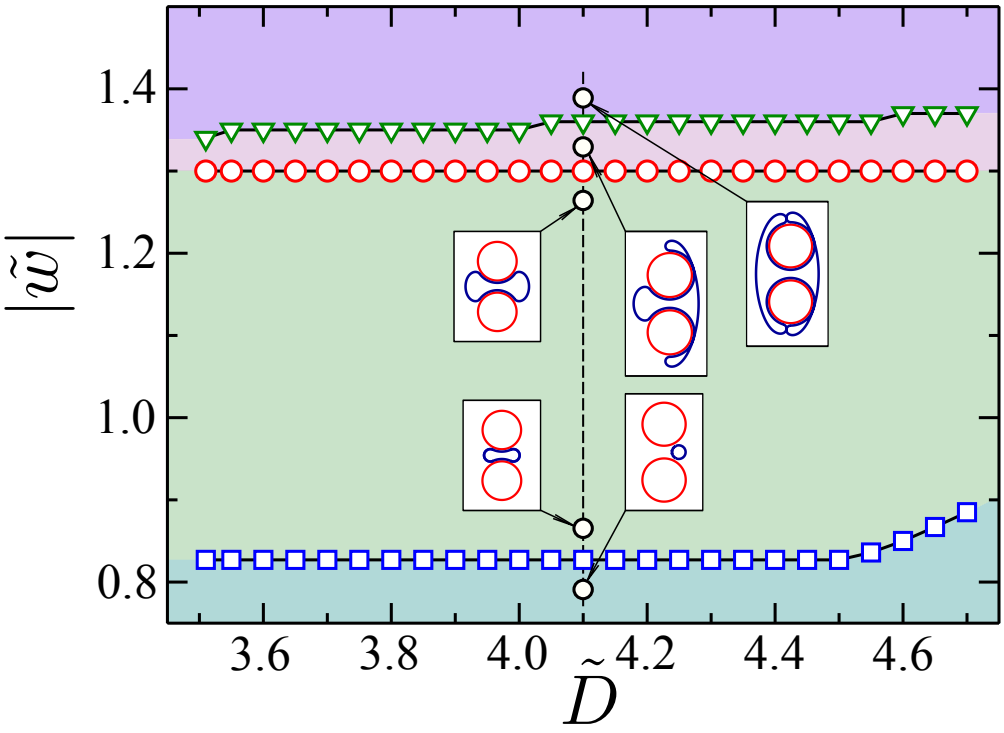

Figure 3.9: Phase diagram for $\tilde{R} = 3.50$ indicating the boundaries between no-wrapping state (blue), symmetric-wrapping state (green) and the asymmetric-wrapping state (red). The first order transition points from weak-wrapping state to the symmetric-wrapping state are shown in blue squares, while the symmetric-to-asymmetric wrapping first-order transition points are shown in red circles. The transition points from asymmetric-wrapping state to closure state are shown in green triangles.

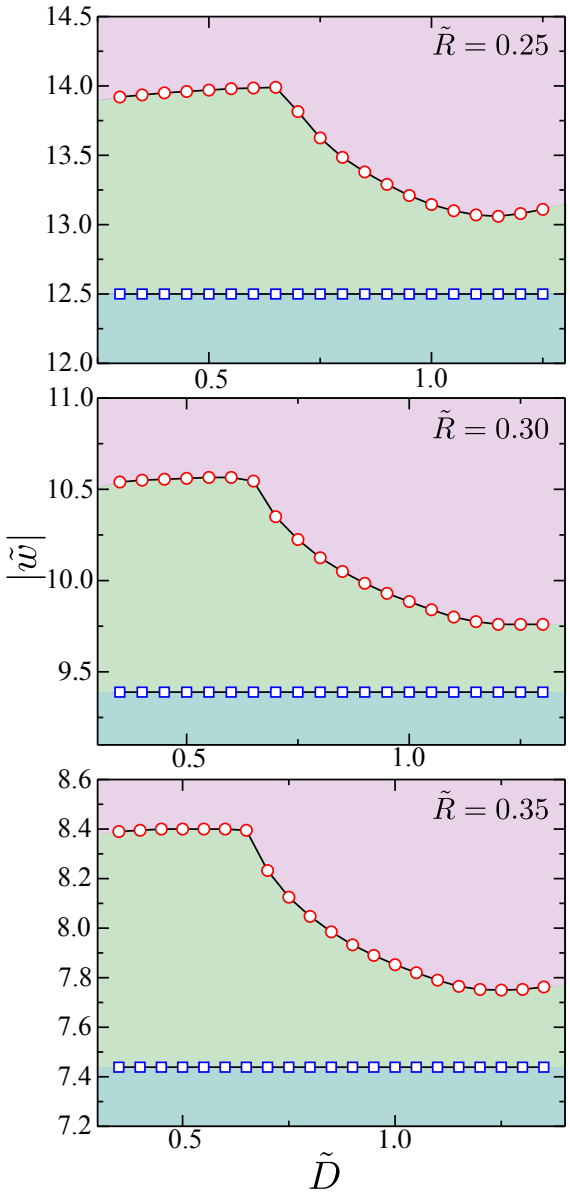

Figure 3.10: Phase diagrams for $\tilde{R} = 0.25$, 0.30 and 0.35 indicating the boundaries between no-wrapping state (blue), symmetric-wrapping state (green) and the asymmetric-wrapping state (red).

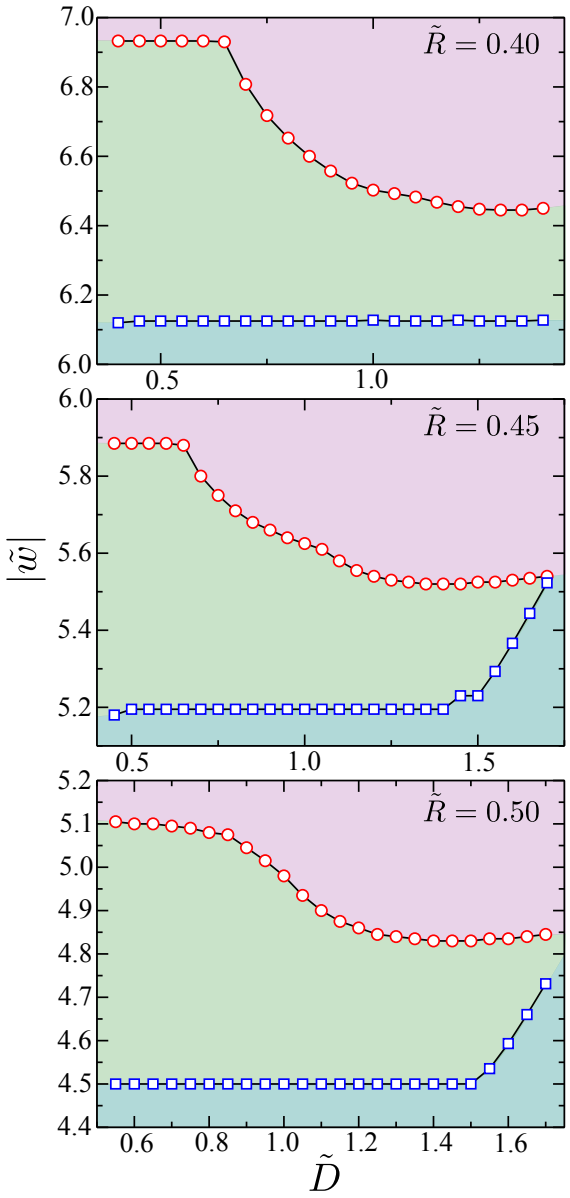

Figure 3.11: Phase diagrams for $\tilde{R} = 0.40$, 0.45 and 0.50 indicating the boundaries between no-wrapping state (blue), symmetric-wrapping state (green) and the asymmetric-wrapping state (red).

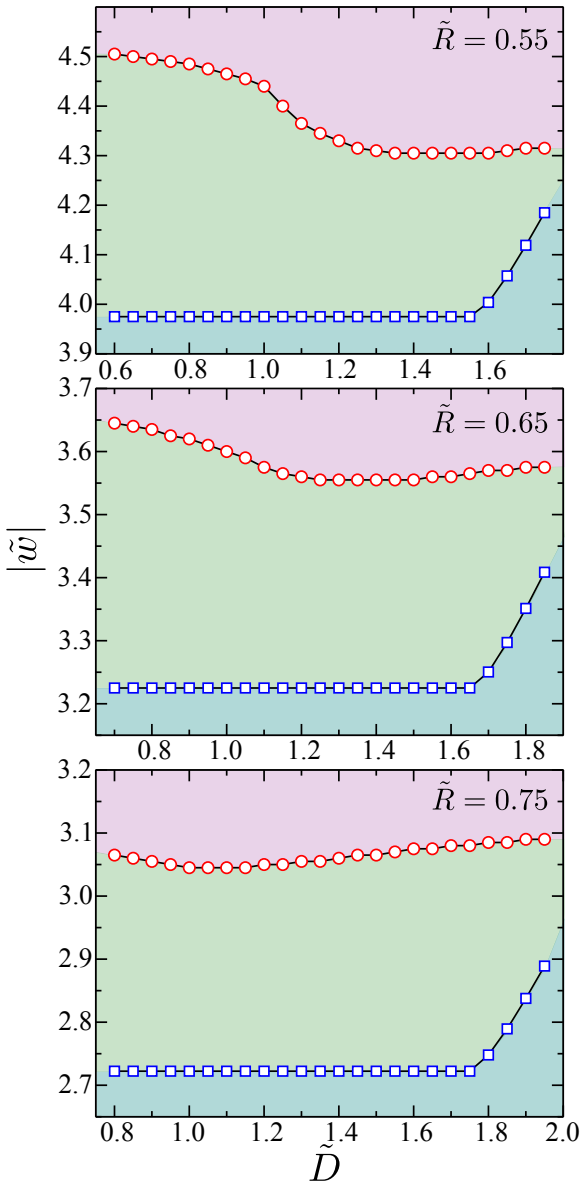

Figure 3.12: Phase diagrams for $\tilde{R} = 0.55$, 0.65 and 0.75 indicating the boundaries between no-wrapping state (blue), symmetric-wrapping state (green) and the asymmetric-wrapping state (red).

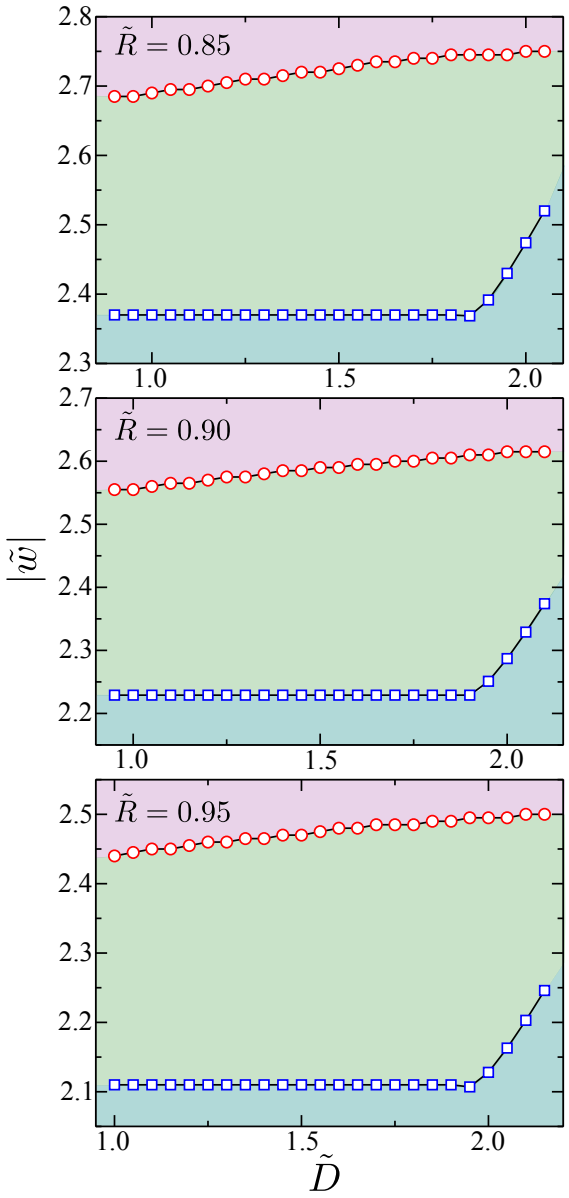

Figure 3.13: Phase diagrams for $\tilde{R} = 0.85$, 0.90 and 0.95 indicating the boundaries between no-wrapping state (blue), symmetric-wrapping state (green) and the asymmetric-wrapping state (red).

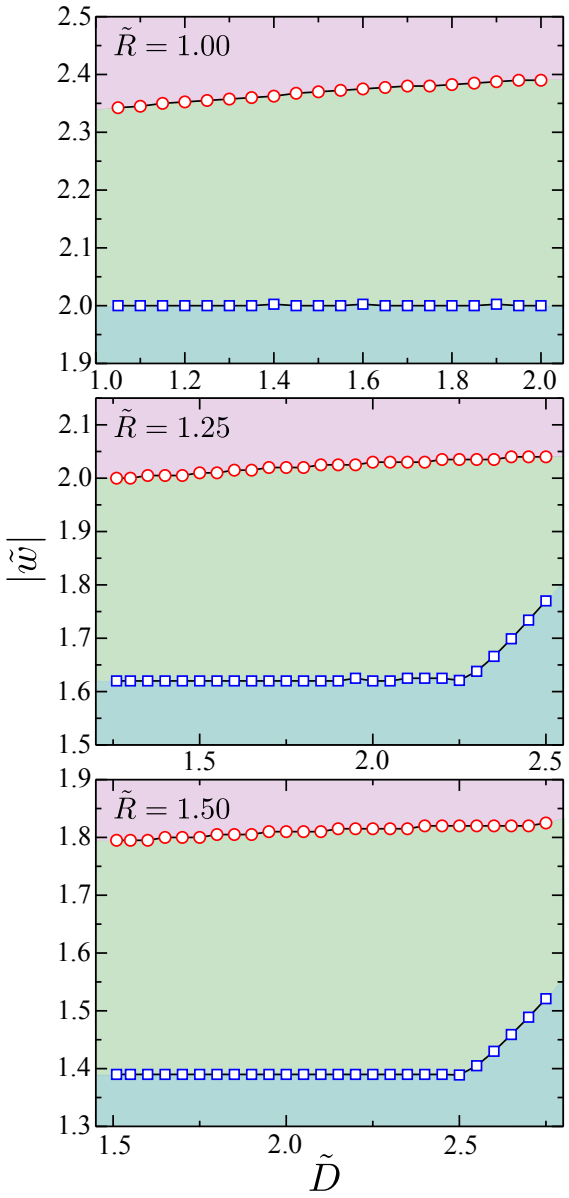

Figure 3.14: Phase diagrams for $\tilde{R} = 1.00$, 1.25 and 1.50 indicating the boundaries between no-wrapping state (blue), symmetric-wrapping state (green) and the asymmetric-wrapping state (red).

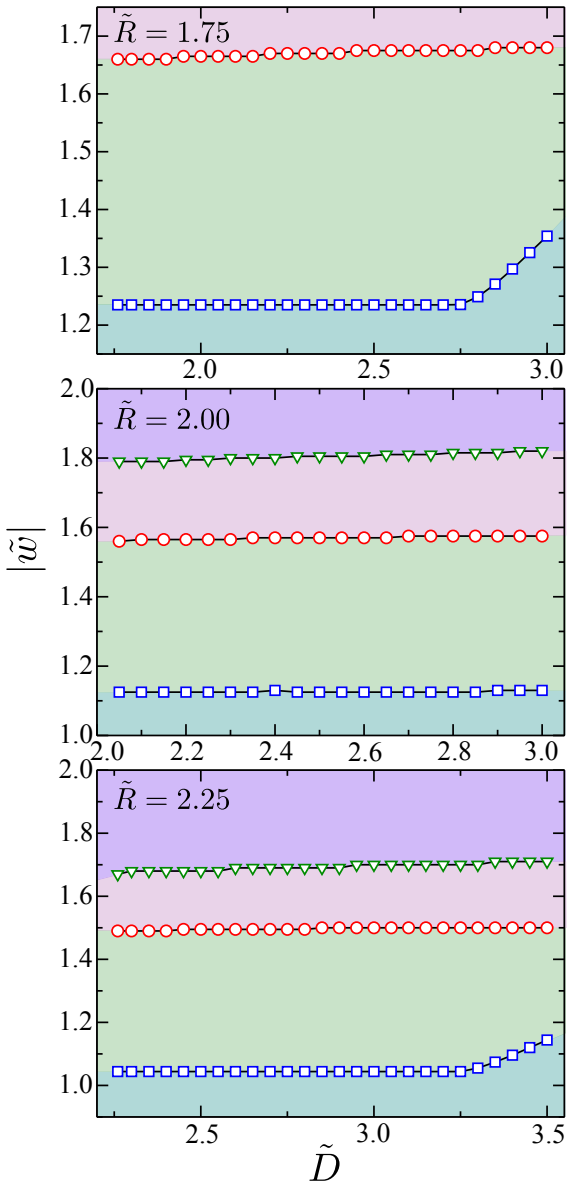

Figure 3.15: Phase diagrams for $\tilde{R} = 1.75$, 2.00 and 2.25 indicating the boundaries between no-wrapping state (blue), symmetric-wrapping state (green), the asymmetric-wrapping state (red) and the closure state (purple).

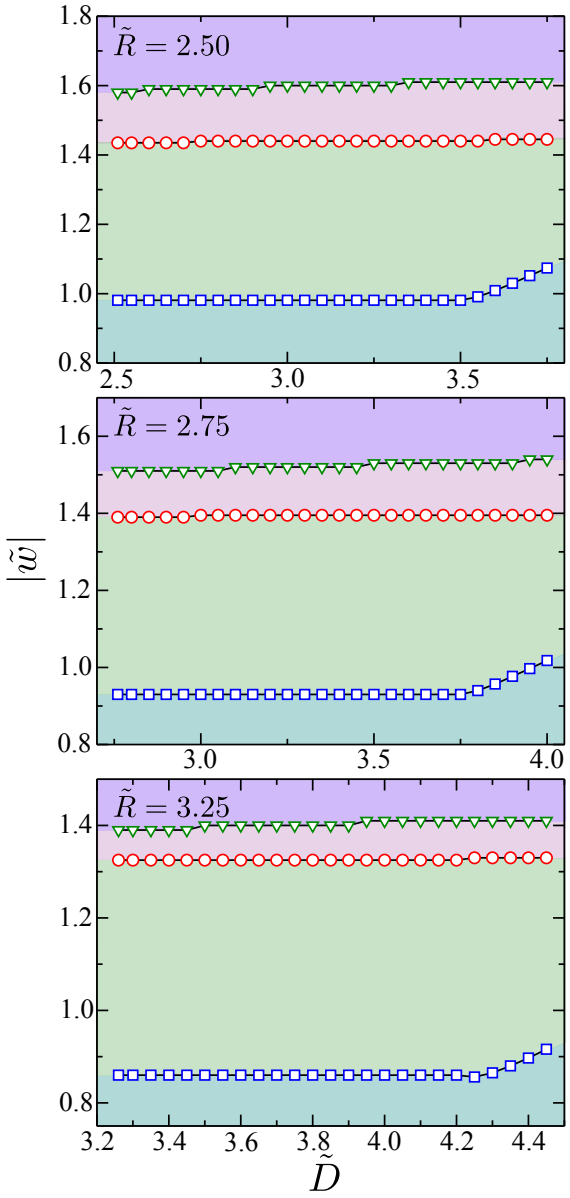

Figure 3.16: Phase diagrams for $\tilde{R} = 2.50$, 2.75 and 3.25 indicating the boundaries between no-wrapping state (blue), symmetric-wrapping state (green), asymmetric-wrapping state (red) and the closure state (purple).

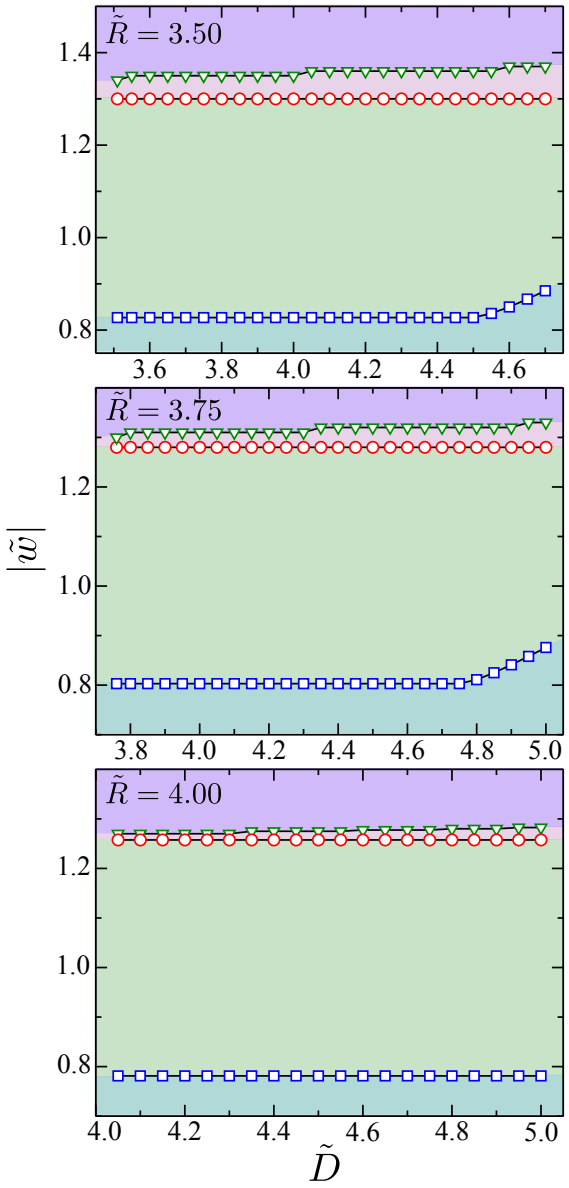

Figure 3.17: Phase diagrams for $\tilde{R} = 3.50$, 3.75 and 4.00 indicating the boundaries between no-wrapping state (blue), symmetric-wrapping state (green), the asymmetric-wrapping state (red) and the closure state (purple).

wrapping state to asymmetric-wrapping state, where the particles are completely enclosed by the membrane.

With increasing size of the cylinders, the asymmetric-wrapping state does not completely encapsulate the cylinders, leaving a gap between the two branches of the membrane from the opposite sides of the cylinders. This can be seen for example, in shapes shown in Fig. 3.3(c3),(c4) for $\tilde{R} = 1.0$ and $\tilde{R} = 1.25$, for example. For the cylinder sizes in the range of $\tilde{R} = 1.0$ to $\tilde{R} = 2.0$, further increase in the adhesion energy gradually leads to complete encapsulation of the cylinders with no signature of phase transition. This is however not the case for cylinder sizes in the range $\tilde{R} > 2.0$, where further increase in the adhesion energy shows existence of another first-order transition from asymmetric-wrapping state to configuration where the cylinders are completely enclosed by the membrane. The transition points for the first order transition from asymmetric-wrapping state to complete closure state are indicated by green triangles on the phase diagrams in Fig. 3.15 - 3.17. Example shapes for the complete closure state are also shown in Figs. 3.4(d1)-(d3).

The phase separation between the symmetric-wrapping state and the asymmetric-wrapping state displays a kink in a certain region of cylinder size $\tilde{R}$ (see for example, Fig. 3.7). This is accompanied with a significant jump in the curvature of the middle portion of the membrane, in between the two cylinders and is a direct consequence of the fact that even for the same contact angle, two solutions with the same free energy minima exist, separated by an energy barrier (see, for example, shapes (e) and (f) in Fig. 2.7). This is also the point where the interaction force between the cylinders changes the sign.

3.4 Fixed Adhesion Energy Between the Cylinders and the Membrane

In this section, we are interested to see how the total reduced free energy of the system, $\Delta\tilde{F}(\tilde{R}, \tilde{D}, \tilde{w}, \gamma_1, \gamma_2)$, depends on the separation between the cylinders $\tilde{D}$ for different values of fixed adhesion energy $\tilde{w}$. The goal is to minimize the total free energy with respect to the separation distance $\tilde{D}$ and map out a phase diagram in the $(\tilde{R}, \tilde{w})$ space.

For each fixed $\tilde{R}$, based on the phase diagrams in the $(\tilde{D}, \tilde{w})$ space mapped out earlier, we first find out the range of the adhesion energies that we are interested in. For each fixed adhesion energy value $\tilde{w}$, we then find the minimum of the function $\Delta\tilde{F}(\tilde{R}, \tilde{D}, \tilde{w}, \gamma_1, \gamma_2)$ for a range of values of $\tilde{D}$ based on the look-up table method described in Section 2.4, essentially tracing straight horizontal lines across the phase diagrams in Figs. 3.10 - 3.17. As a result for each $\tilde{w}$ we generate a free energy curve as a function of the separation

distance between the cylinders and then repeat the procedure for gradually increasing values of $\tilde{w}$. Example free energy curves are shown in Figs. 3.18 ($\tilde{R} = 0.25$, 0.30 and 0.35), 3.19 ($\tilde{R} = 0.40$, 0.45 and 0.50) and 3.21 ($\tilde{R} = 1.00$, 2.00 and 4.00), where the values of the adhesion energies are shown on the right side of the diagrams.

Our results show that for relatively small adhesion energy values $\tilde{w}$, where the system is still within the two phase boundaries (weak-wrapping to two-fold symmetric-wrapping state (blue squares) and symmetric-wrapping state to asymmetric-wrapping state (red circles)), for the range of the separation distances considered, the interaction is always attractive, with the minimum of the free energy occurring at the point where the two cylinders are in close contact with each other (we leave a gap of $\Delta\tilde{D} = 0.01$ for numerical convenience). The free energy curves corresponding to $\tilde{R} = 0.35$ and $\tilde{w} = 7.6$ in Fig. 3.18, or $\tilde{R} = 0.40$ and $\tilde{w} = 6.4$ in Fig. 3.19 are examples of such case, where the configuration of the membrane remains two-fold symmetric along the curve for all the values of $\tilde{D}$. This means, for example, that in Fig. 3.2 the state in (b1) has smaller energy that the state in (b2) and so on, which is due to the fact that closer separation between the cylinders results in more wrapping (hence more adhesion, which is preferred by the system) and less "excess" membrane being pulled in.

With further increase in the adhesion energy, the horizontal lines corresponding to fixed $\tilde{w}$ that we trace in diagrams in Figs. 3.10 - 3.17 start to cross the partially wrapped to asymmetric deep wrapping boundary line (represented by red circles) for large values of $\tilde{D}$, which results in a second weak minima appearing in the free energy curves in Figs. 3.18 - 3.21. With increasing adhesion energy, near the critical point the two minima observed (one corresponding to cylinders being in a close contact with overall configuration of the membrane being two-fold symmetric, see, for example, Fig. 3.2(b1), and the second minima corresponding to an asymmetric state with a fixed separation between the cylinders as in Fig. 3.2(c3)) have equal free energy value and are separated by an energy barrier. We do this for all the values of $\tilde{R}$ considered in this work, and indicate the transition points separating the two-fold symmetric state from the asymmetric-wrapping state are indicated by filled red circles on the diagram in Fig. 3.22.

It is interesting to note that the picture changes for increasing values of the the cylinder radius $\tilde{R}$. For example, for $\tilde{R} = 0.65$ in Fig. 3.20, we still observe the second minimum corresponding to a larger separation between the cylinders, but it never quite reaches the minimum corresponding to the state where two cylinders are in contact, no matter how large the adhesion energy is. With further increase of the size of the cylinders $\tilde{R}$, the second minimum becomes weaker and disappears completely. This indicates that for relatively large cylinder radius size ($\tilde{R} > 0.65$) if the distance is allowed to change freely, the interaction is always attractive leading to cylinders being in a state of close contact. For

relatively small adhesion energy values, the close contact occurs in the two-fold symmetric state and is always preferable to the complete wrapping of the cylinders, since the deformation of the membrane in the latter case cannot be compensated with the adhesion energy any more. For larger adhesion energies, where we are in the region of the asymmetric deep wrapping state, the interaction is still attractive, and the membrane configuration around the cylinders (in close contact) is in the asymmetric wrapping state, since the adhesion energy is now sufficient to compensate for the deformation. This is an interesting results, since for cylindrical colloids on a flat membrane, the interaction has been shown to be always repulsive for all ranges of the adhesion energies [7, 10], and it's possible that the spontaneous curvature of the membrane can affect the sign of the interaction.

An example of diagrams where no second minima is observed are shown in Fig. 3.21 for $\tilde{R} = 1.0$, $\tilde{R} = 2.00$ and $\tilde{R} = 4.0$ for a range of adhesion energies $\tilde{w}$. We see that in any case, regardless of the configuration the interaction between the cylinders is attractive. Note however that, transition from the partially wrapped state to asymmetric-wrapping state still happens (even though the cylinders are in close contact), but the value of the transition point has to be determined from the phase diagrams in Figs. 3.10 - 3.17, for the separation distance that corresponds to the close contact. After minimizing the total reduced free energy $\Delta\tilde{F}(\tilde{R}, \tilde{D}, \tilde{w}, \gamma_l, \gamma_r)$ with respect to the separation distance $\tilde{D}$ in the process described above, we can finally map out a phase diagram separating three phases in the phase space $(\tilde{R}, \tilde{w})$, essentially taking $\tilde{D}$ out of the picture. The resulting diagram is shown in Fig. 3.22, where the green squares indicate the boundary between the no-wrapping state and symmetric-wrapping state and the red circles represent the boundary between the symmetric-wrapping state and the asymmetric-wrapping state.

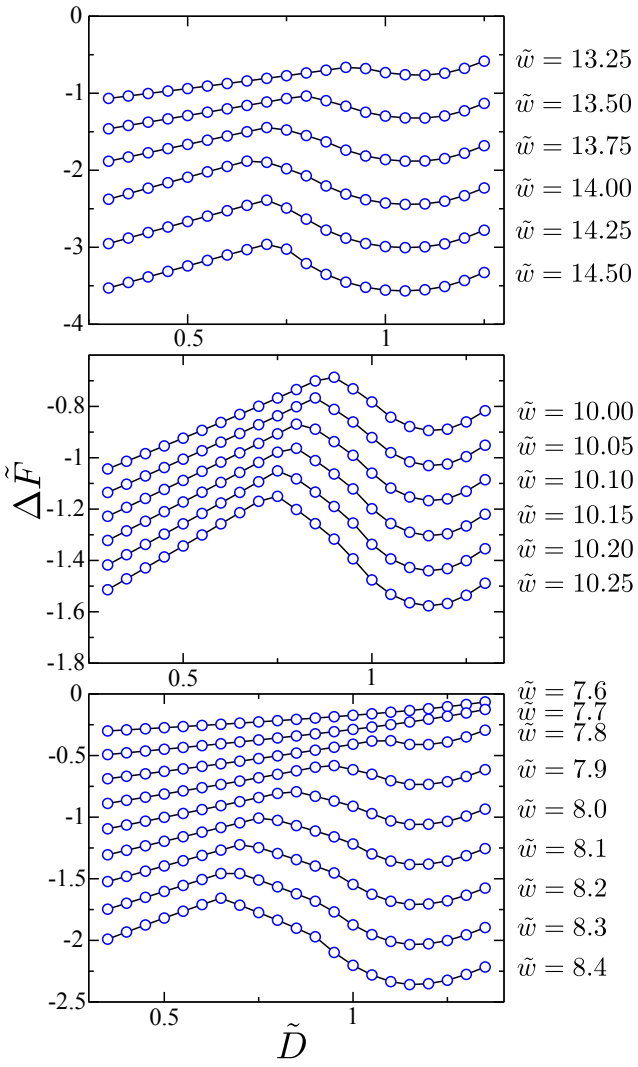

Figure 3.18: Free energy dependence on the separation distance between the cylinders $\tilde{D}$ for various adhesion energies $\tilde{w}$ for $\tilde{R} = 0.25$, $\tilde{R} = 0.30$ and $\tilde{R} = 0.35$ (top to bottom).

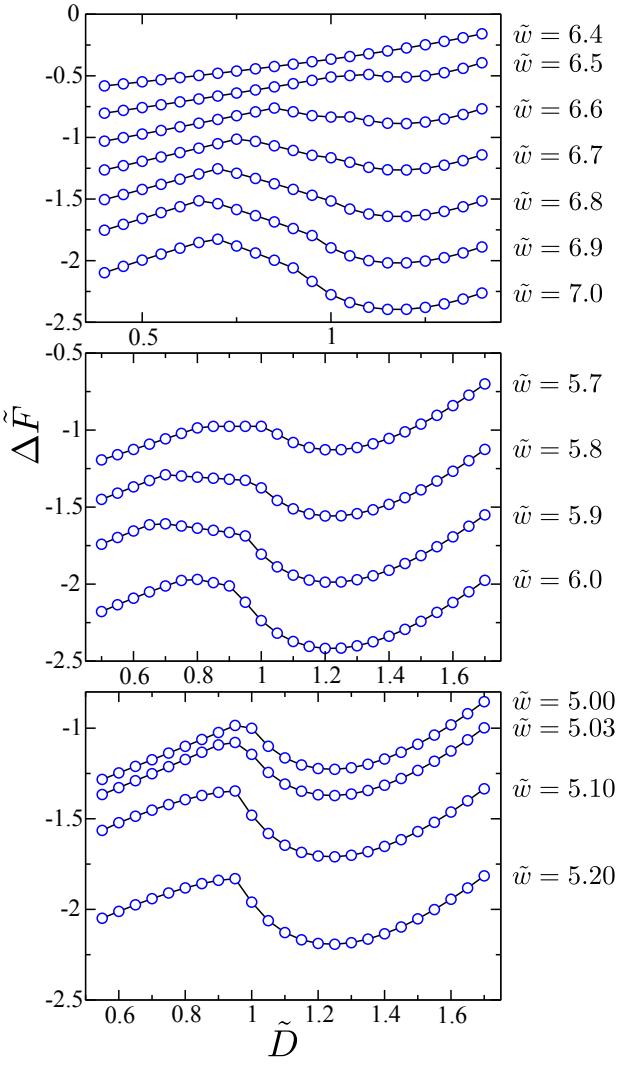

Figure 3.19: Free energy dependence on the separation distance between the cylinders $\tilde{D}$ for various adhesion energies $\tilde{w}$ for $\tilde{R} = 0.40$, $\tilde{R} = 0.45$ and $\tilde{R} = 0.50$ (top to bottom).

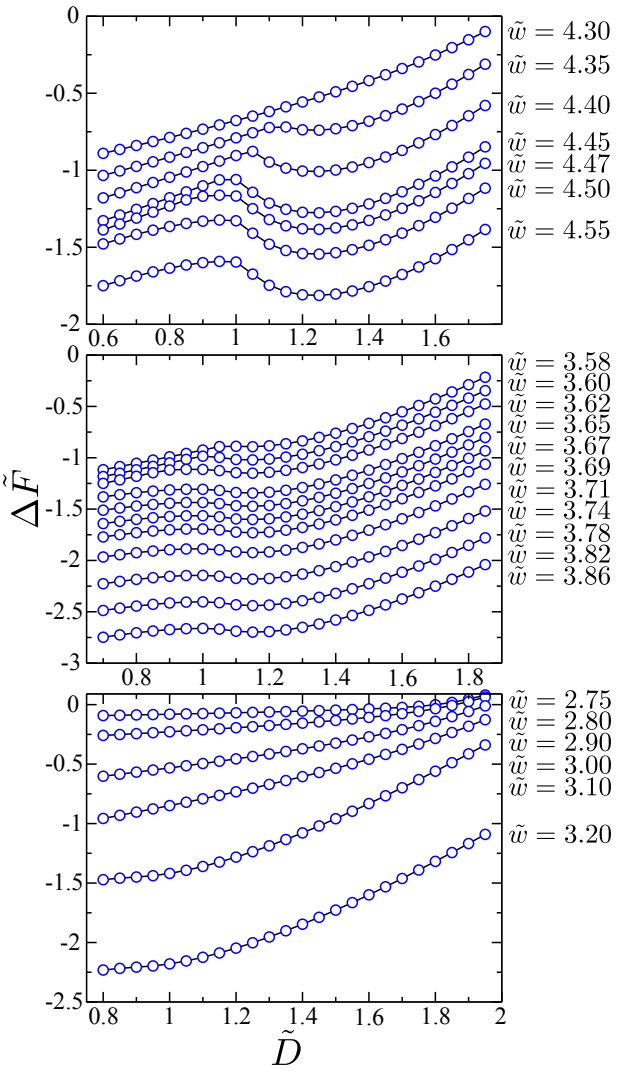

Figure 3.20: Free energy dependence on the separation distance between the cylinders $\tilde{D}$ for various adhesion energies $\tilde{w}$ for $\tilde{R} = 0.55$, $\tilde{R} = 0.65$ and $\tilde{R} = 0.75$ (top to bottom).

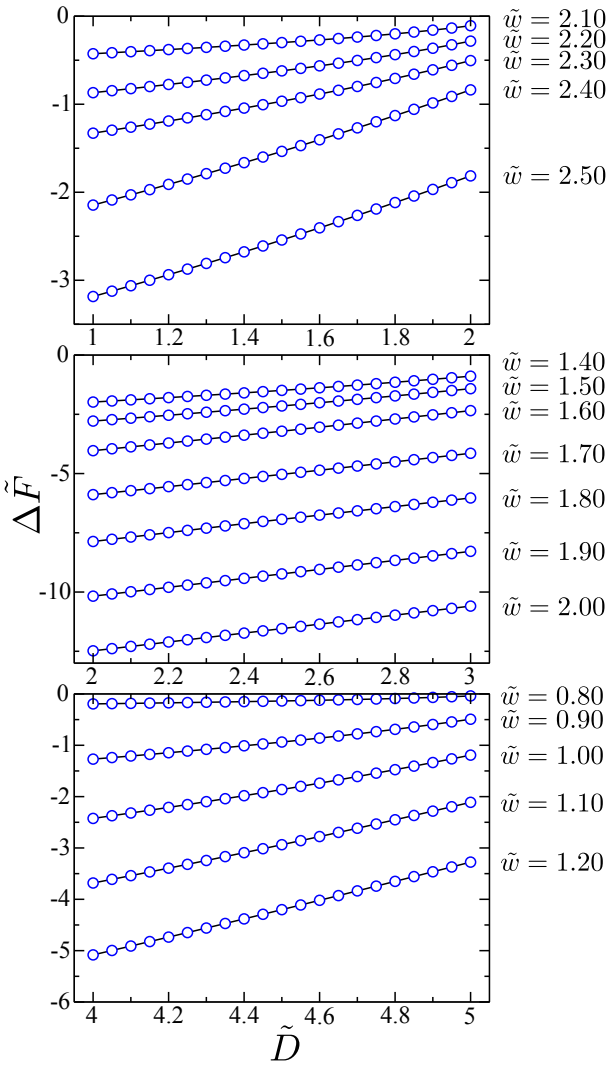

Figure 3.21: Free energy dependence on the separation distance between the cylinders $\tilde{D}$ for various adhesion energies $\tilde{w}$ for $\tilde{R} = 1.00$, $\tilde{R} = 2.00$ and $\tilde{R} = 4.00$ (top to bottom).

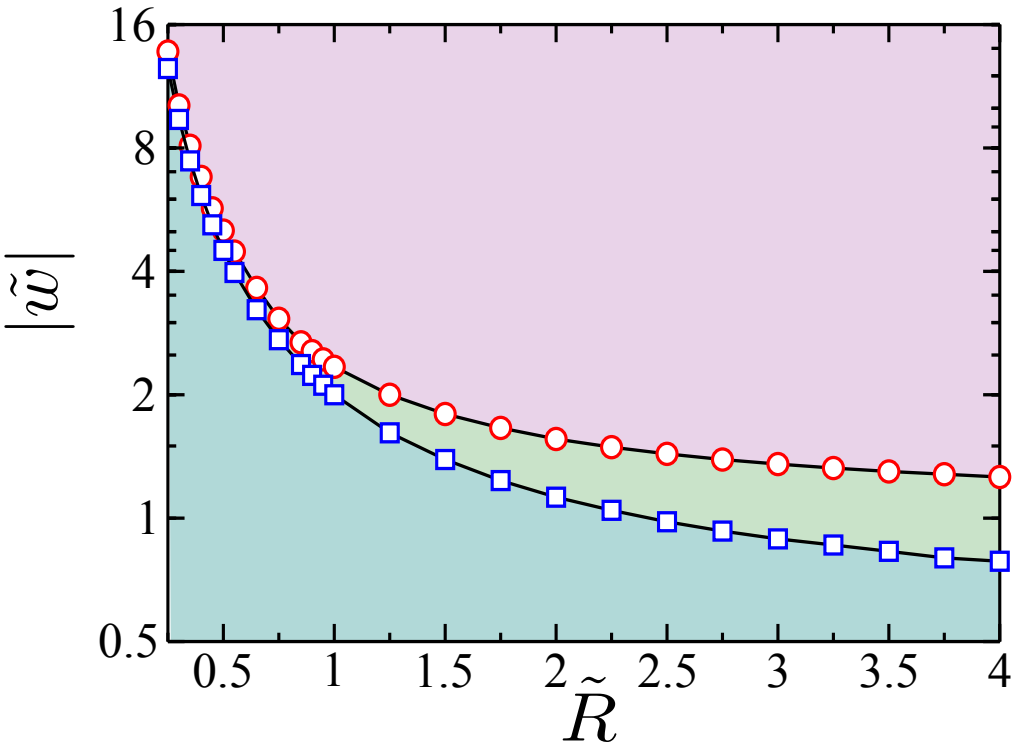

Figure 3.22: The phase diagram for the system of two cylinders of radius R adhering to a soft membrane tube of radius r_0 in the phase space of the adhesion energy $\tilde{w} = wr_0^2/\kappa$ and the relative size of the cylinders $\tilde{R} = R/r_0$. Blue squares represent the boundary separating the no-wrapping state (shown in blue) and the symmetric-wrapping state (shown in green), while the red circles represent the boundary between the symmetric-wrapping state and the asymmetric-wrapping state (shown in red).

Chapter 4

Summary and Outlook

4.1 Summary

In summary, we have investigated phases that can form when two long rigid cylindrical particles of radius R adhere to a membrane tube of radius r_0, where the axes of all three are in parallel, through an excluded-volume interaction and a short-ranged attraction represented by a potential energy per unit area w. We have used the Helfrich model to characterize the free energy of the membrane, which possesses a bending energy κ and surface tension σ. As shown in Section 2.4, of the five parameters present in the system – the nanoparticle radius R, their separation distance D, membrane bending rigidity κ, surface tension σ and the adhesion energy w, only three dimensionless combinations, R/r_0, D/r_0, and wr_0^2/κ, are relevant in the consideration of the structure of the current system.

Starting from the Helfrich model describing the free energy of the system, we have developed a numerical procedure that allows us to solve the shape equations that correspond to the minimum of the free energy in a large range of R/r_0. The analysis of the free energy then leads to the conclusion that multiple phase transitions exist in the system. Similar to several related systems, a non trivial free-to-bound continuous adhesion transition is found, where the membrane tube gets "bound" to the cylinders, slightly deforming its original circular shape. The non-triviality of the transition is in the fact that the free state exists even in a non-zero adhesion potential, and is a result of the competition between the bending and adhesion energies present in the model. Beyond the bound state several stable states are identified, for the increasing interaction strength between the cylinders and the membrane tube. After binding to the cylinders, the membrane gets "sucked in" between the two cylinders in a configuration that is two-fold symmetric and resembles a

dumbbell shape. Further increase in the adhesion energy leads to a break in the symmetry with respect to one of the axes and the membrane becomes significantly curved. Depending on the relative size of the cylinders (relative to the size of the membrane tube), a further discontinuous transition is identified for a certain region of the parameter space, where the membrane tube completely encapsulates the cylinders. For smaller cylinder size, the encapsulation is gradual and carries no signature of a discontinuous phase transition. One of the variables in the system, the cylinder separation D, is then eliminated from the picture through the minimization of the free energy of the system with respect to the separation between the cylinders and the results are then summarized in a single phase diagram, that separates the unbound, symmetric and the asymmetric configurations in the parameter space of the adhesion energy and the relative size of the cylinders.

The second part of the analysis discusses the free energy dependence on the separation between the cylinders for various fixed adhesion energies. We show that for relatively small size of the cylinders, the state of the minimum free energy is achieved at a non-zero separation distance, even in the completely encapsulated state, which increases with the increasing size of the membrane tube. Interestingly, the interaction changes qualitatively with the increase of the cylinder size R/r_0. For a certain critical value of the adhesion energy, a first-order transition is identified between the states where cylinders are separated and the state where cylinders are in close contact. This is accompanied by a jump in the curvature of the membrane between the cylinders. Note that the aggregated state is qualitatively different from the one observed in related three-dimensional systems, since in the aggregated state a significant chunk of membrane still wraps around the cylinders from the middle section (see Fig. 3.3(c2), for example). Beyond a certain value for the size of the cylinders, the state with fixed separation between the cylinders can no longer be stabilized and the interaction becomes attractive regardless of the strength of the interaction between the membrane and the cylinders. This drives the aggregation of the cylinders on the tube in the significantly curved membrane state.

One could think of an experimental setup similar to the one in Ref. [24] to observe the transitions described in our work. For example, it was proposed by Roux *et al.* that a lipid reservoir, kinesin-coated beads and microtubule networks could serve as a minimal system for generating complex tubular structures such as the endoplasmic reticulum, Golgi apparatus and endosomes. In fact, in experiments performed in Ref. [24] complex tubular networks were formed by the kinesin-coated beads pulling on membrane vesicle along the microtubules, which indicates that nanotubes can be used to grow and build membrane networks. Up to several membrane tubes were shown to be able to stabilize along a single microtubule. In a similar setup, by controlling the attractive interaction between the membrane tubes and the microtubules, as well as the size of the microtubules in the

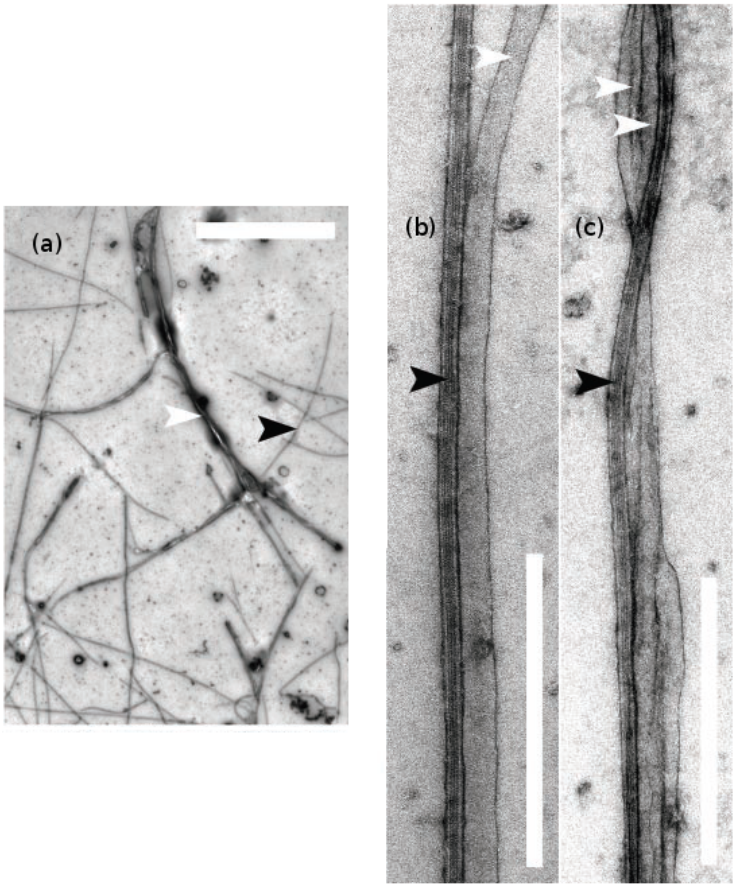

Figure 4.1: (a) Networks of membrane tubes (white arrows) growing on a microtubule network (black arrows). (b) A single tube aligned along microtubule and (c) bundles of two tubes on a microtubule. The bar in (a) is 5 μm and 0.5 μm in (b) and (c). Image taken from Ref. [24].

solution, one could look into the configuration properties of the membrane shapes discussed in this work.

4.2 Outlook

The work described in this Thesis contributes to the body of knowledge relating to the conformational behaviour of membrane shapes in various physical settings. Mapping of the phase diagrams for membrane-nanoparticle systems helps to theoretically understand and predict different membrane structures and the interaction of particles it drives, which can be used in many practical applications such as targeted drug delivery or the development of biosensors. Our results suggest interesting new features in the system of tubular membranes interacting with cylindrical particles. First, we show that the addition of one extra particle to the membrane tube changes the picture quite significantly. Several phases are identified, some of which are accompanied by a symmetry break in the system and are closely related to configurations observed in similar systems. We observe, for example, that in a significantly curved regime, cylindrical particles tend to aggregate in the negative curvature region. Similar effect was observed in a related system, where a light microscopy study in Ref. [42] showed that spherical nanoparticles can cluster in the negative curvature region of the vesicle, or aggregate into ring like structures around the "waist" of the vesicle resulting in a dumbbell shape [42] – configurations that are very similar to ones observed in our work. We also observe an attractive interaction between the cylindrical particles in a certain parameter region, which suggests that the spontaneous curvature of the membrane can play a role in the sign of the interaction between the nanoparticles adhered to it.

As a next step, it would be interesting to look into the adhesion of two *spherical* particles to a closed membrane vesicle, which is a system of high complexity [42, 71, 89, 90, 88]. Analytical solution for a system of membrane vesicle interacting with several nanoparticles becomes incredibly challenging due to the complex geometry of the system and one has to resort to numerical methods. Development of recent tools, such as the Surface Evolver package [91], has proven to be very useful in the applications to membrane systems of these kind. The package allows one to define various energies for a discretized membrane surface of a desired geometry and "evolve" it to the minimum energy state. One can also define custom constraints, such as the total area or volume of the system, which are particularly useful when dealing with closed membrane vesicles. An interesting application of the package has been demonstrated recently for flat membranes interacting with two spherical nanoparticles [36], where attractive interaction has been shown to exist in the deep-curvature regime. It will be interesting to extend the work done in Ref. [36] by

implementing a system of a *closed vesicle* and see if aggregation of nanoparticles on vesicles can be attained in such systems.

Other interesting problems exist in the field. We now know that nanoparticles adhering to the inner wall of membrane vesciles can co-operatively drive tubulation and subsequent pearling of the system. For example, in Ref. [44], phospholipid vesicles containing several nanoparticles were shown to transform from the usual spherical structure into pearls and pearl necklaces that were stable for several hours. This proposes a new way of membrane tubulation and it will be interesting to theoretically model the process within the Helfrich model, which will require a consideration of several nanoparticles adhered to the inner wall of a closed vesicle. The structure of the system consisting of rigid particles confined in a tubular membrane has already been studied in Ref. [29], and it will be interesting to see tubulation for such systems can be described within the Helfrich theory.

APPENDICES

Appendix A

Numerical Methods

A.1 Numerical Integration of Ordinary Differential Equations

A.1.1 Introduction

As described in Section 2.4, in order to find the free energy of the free part of the membrane, our first task is to solve the second-order differential equation in Eq. 2.40. Ordinary differential equations can always be reduced to a system of first-order differential equations by introducing new functions into the system. For example, the following second-order differential equation,

$$\frac{d^2y}{dx^2} + q(x)\frac{dy}{dx} = r(x), \tag{A.1}$$

can be reduced to a system of two, first-order differential equations,

$$\begin{aligned} \frac{dy}{dx} &= z(x) \\ \frac{dz}{dx} &= r(x) - q(x)z(x), \end{aligned}$$

where we have introduced a new variable $z(x) = dy/dx$. This approach can be generalized for the equations of any order, meaning that any generic problem in ordinary differential equations can be reduced to the study of a set of N coupled, first-order equations for functions y_i $(i = 1, 2, 3, \ldots, N)$,

$$\frac{dy_i(x)}{dx} = f_i(x, y_1, y_2, \ldots, y_N), \qquad i = 1, 2, \ldots, N, \tag{A.2}$$

where the functions f_i, on the right hand side are known.

The problem, however, is not fully specified by the equations in A.2. One also needs to know the boundary conditions, that are simply algebraic conditions on the values of functions y_i in the above system. The nature of the boundary conditions determines the type of the numerical approach that needs to be used for the particular problem. There are two types of boundary conditions,

- *Initial value problems* – where all the values for y_i functions are given at some starting point x_a, and need to find the values of the functions y_i at a different point x_b. Numerically this is easier to implement and is usually preferred.
- *Two point boundary value problems* – where the values for functions y_i are given at two different points x_a and x_b. Typically the values for some of the functions y_i will be given at point x_s, while the values for the others are given at x_b. Numerically the implementation is more involved and requires solving an initial value problem multiple times until the desires boundary conditions are reached.

We first discuss the initial value problem, since the solution to the boundary value problem requires solving initial value problems as an intermediate step.

The basic idea for solving initial value problems, is to re-write the dy's and dx's in the Eqs. A.2 as finite differences Δx and Δy and, starting from initial values for y_i (given), find the change in the functions y_i by changing the independent variable x, one Δx step at a time. In the limit of a small step-size Δx a good approximation to the solution at the other boundary is achieved. The direct implementation of this is known as Euler's method, which is however not recommended, since it's a first-order method (the error produced at each step is proportional to the square of the step-size). We will use numerically more accurate Runge-Kutta method, which produces the value of the function at the end of each interval Δx by using a weighted average over several Euler-style steps.

A.1.2 The Classic Runge-Kutta Method

The formula for the Euler's method is

$$y(x+h) = y(x) + hf(x, y(x)), \tag{A.3}$$

which, for given $y(x)$, advances from x to $x+h$ and produces the value for $y(x+h)$ based on the information about the derivative of the function at the beginning of the interval

$[x, x+h]$. The magnitude of the error arising from the Euler's method can be computed by the comparison with a Taylor expansion of the function $y(x)$.

$$y(x+h) = y(x) + hy'(x) + \frac{1}{2}h^2 y''(x) + O(h^3), \tag{A.4}$$

Since we know that $y'(x) = f(x, y)$,

$$y''(x) = \frac{\partial f}{\partial x} + \frac{\partial f}{\partial y}\frac{\partial y}{\partial x} = \frac{\partial f}{\partial x} + \frac{\partial f}{\partial y}f(x, y) \tag{A.5}$$

Using Eq. A.5 in the Taylor expansion for $y(x)$ in Eq. A.4 we get,

$$y(x+h) = y(x) + hy'(x) + \frac{1}{2}h^2\left(\frac{\partial f}{\partial x} + \frac{\partial f}{\partial y}f(x, y)\right) + O(h^3), \tag{A.6}$$

and therefore the error induced by the Euler's method is

$$\frac{1}{2}h^2\left(\frac{\partial f}{\partial x} + \frac{\partial f}{\partial y}f(x, y)\right) + O(h^3). \tag{A.7}$$

For small step-size h the error induced at each Euler step is proportional to h^2. In general, to solve an equation over a range of x, the number of steps should be proportional to $1/h$. The number of steps multiplied by the error in each step will give us a global error proportional to h, and thus the Euler's method is a first order method (a method is conventionally called n-th order if its error term is $O(h^{n+1})$).

We could improve the accuracy of the Euler step in Eq. A.3 by taking an extra step to the midpoint of the interval $[x, x+h]$, and then using the value of both x and y at that point as our starting point for the next step across the interval, reaching our desired destination in two steps instead of one. The value $y(x+h)$ can then be given as

$$y(x+h) = y(x) + k_2 + O(h^3), \tag{A.8}$$

where

$$\begin{aligned} k_2 &= hf(x + \frac{h}{2}, y + \frac{k_1}{2}), \\ k_1 &= hf(x, y). \end{aligned}$$

This cancels out the first-order error term, making the method second-order (called second-order Runge-Kutta or midpoint method).

The most commonly used Runge-Kutta method is the so-called classical (or fourth order) Runge-Kutta method. The method is given by the following equations,

$$y(x+h) = y(x) + \frac{1}{6}(k_1 + 2k_2 + 2k_3 + k_4), \tag{A.9}$$

where

$$\begin{aligned} k_1 &= hf(x,y), \\ k_2 &= hf(x+\frac{h}{2}, y+\frac{k_1}{2}), \\ k_3 &= hf(x+\frac{h}{2}, y+\frac{k_2}{2}), \\ k_2 &= hf(x+h, y+k_3). \end{aligned}$$

The classical Runge-Kutta method is a fourth-order method, meaning that the error per step is on the order of h^5, while the total accumulated error has order h^4. We will use this method in all of our numerical integrations for each of the functions in Eqs. 2.41.

A.1.3 Two-Point Boundary Value Problems and The Shooting Method

For two-point boundary value problems, the ordinary differential equations are required to satisfy boundary conditions at more than one value of the independent variable. The main difference between initial value problems and two-point boundary value problems is that for the former, we can solve the ODEs by simply marching along the integration variable from the starting point to the end of the integration interval, while, for the two-point boundary value problems, the boundary conditions at the starting point are not all given and a given "random" choice is pretty much guaranteed not to satisfy the boundary conditions at the other end of the region.

In general, for two-point boundary value problems, we want to find a solution to a set of N coupled first-order ordinary differential equations, satisfying n_1 boundary conditions at the starting point x_a and a remaining set of $n_2 = N - n_1$ boundary conditions at the final point x_b. The differential equations can be written as

$$\frac{dy_i(x)}{dx} = g_i(x, y_0, y_1, \ldots, y_{N-1}), \qquad i = 0, 1, 2, \ldots, N, \tag{A.10}$$

where at x_a the solutions have to satisfy the following equations

$$B_{1j}(x_a, y_0, y_1, \ldots, y_{N-1}), \qquad j = 0, 1, 2, \ldots, n_1 - 1, \tag{A.11}$$

and at x_b the solutions are supposed to satisfy

$$B_{2k}(x_b, y_0, y_1, \ldots, y_{N-1}), \qquad k = 0, 1, 2, \ldots, n_2 - 1. \tag{A.12}$$

For the two-point boundary value problems described above the so-called shooting method is typically used. In this method one normally chooses the values for all of the dependent variables at one boundary essentially in a random guess. With this, a full set of the initial values is given and we can now simply integrate the ODEs using the Runge-Kutta method discussed above, arriving at the other boundary, where in general, we will have discrepancies from the desired boundary values. At this point, we now have a multidimensional root-finding problem, that is, we want to find such adjustment of the free parameters at the starting point that zeroes the discrepancies at the other end of the boundary.

For our specific problem, the implementation of the shooting method is slightly different since the length of the integration interval is unknown. For the ODEs in Eq. 2.41, in order to have a complete initial value problem, we need to know the values for the length of the integration interval $\tilde{S}$, the initial value ξ for the function $\phi(\tilde{s})$ at the beginning of the interval $[0, \tilde{S}]$, and the Lagrange multiplier λ. We want to find such a triple, that will lead to the desired boundary conditions in Eq. 2.48 at the other end of the integration interval $\tilde{s} = \tilde{S}$. To achieve this, after each integration step, for a random guess of $(\tilde{S}, \xi, \lambda)$ we find and store the discrepancies of the following three functions

$$\begin{aligned} \Delta\psi &= \psi(\tilde{S}), \\ \Delta\theta &= \int_0^{\tilde{S}} \frac{\cos(\psi(s))}{\tilde{\psi}}\, \mathrm{d}\tilde{s} - \frac{\pi}{2} + \theta_0, \\ \Delta\tilde{x} &= \tilde{x}(\tilde{S}) - X_{sym}, \end{aligned} \tag{A.13}$$

which are now functions of only three variables, $\tilde{S}$, ξ and λ. The next step is to solve a multidimensional root finding problem, where we want to find the values for $\tilde{S}$, ξ, λ that will zero the discrepancies $\Delta\psi$, $\Delta\theta$ and $\Delta\tilde{x}$ in Eq. A.14. This is implemented using the Newton-Raphson method for three-dimensions.

A.1.4 Newton-Raphson Method for a System of Equations

Newton-Raphson method is a method for finding successfully better approximations to the roots of a real-valued function. For a one-dimensional case the Newton-Raphson method consists of geometrically extending the tangent line at a current point x_i until it crosses zero

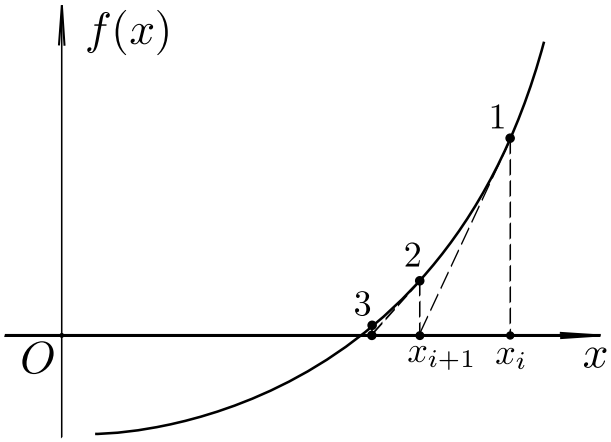

Figure A.1: Illustration of the Newton's method for one-dimension

and pick the next guess x_{i+1} the abscissa of that zero-crossing (see Fig. A.1). Algebraically this is based on the Taylor expansion of the function in the neighbourhood of a point,

$$f(x+\delta) \approx f(x) + f'(x)\delta + \frac{f''(x)}{2}\delta^2 + \dots . \tag{A.14}$$

For small values of δ the terms beyond the second order are unimportant and thus $f(x+\delta)$ implies

$$\delta = -\frac{f(x)}{f'(x)}. \tag{A.15}$$

The process then is repeated as

$$x_{i+1} = x_i - \frac{f(x)}{f'(x)} \tag{A.16}$$

until the desired accuracy is reached.

The method readily generalizes to multiple dimensions. For our problem the three freely-specifiable variables $\tilde{S}$, ξ and λ are treated as components of a vector $\boldsymbol{V}$. A given vector $\boldsymbol{V}$ fully defines the vector $\boldsymbol{y}$ at the starting point $\tilde{s} = 0$, which contains the values of all the functions in Eq. 2.41 at that point. It can then be turned into a different vector $\boldsymbol{y}$ at the final point $\tilde{s} = \tilde{S}$ through the integration of ODEs using the Runge-Kutta method for initial value problems described above. Once at the point $\tilde{s} = \tilde{S}$, we can define another vector $\boldsymbol{F}$ for the discrepancies in Eq. A.14, whose components indicate how far are we

from satisfying our boundary conditions. The next step is a simple implementation of Newton-Raphson method where we want to find values for the components of the vector $\boldsymbol{V}$ that zeroes the components of the vector $\boldsymbol{F}$. The implementation of this step involves solving the set of three linear equations,

$$\boldsymbol{J}\delta\boldsymbol{V} = -\boldsymbol{F}, \tag{A.17}$$

and then adding the corrections back,

$$\boldsymbol{V}^{new} = \boldsymbol{V}^{old} + \delta\boldsymbol{V}, \tag{A.18}$$

where in the above equations the $\boldsymbol{J}$ is the Jacobian matrix, with the components defined as,

$$J_{ij} = \frac{\partial F_i}{\partial V_j}. \tag{A.19}$$

The above derivatives have to be computed numerically, by a separate integration of the ODEs, followed by the evaluation of,

$$\frac{\partial F_i}{\partial V_j} \approx \frac{F_i(V_1, V_2, ..., V_j + \Delta V_j, ..., V_N) - F_i(V_1, V_2, ..., V_j, ..., V_N)}{\Delta V_j} \tag{A.20}$$

As a result of this procedure we obtain the values for $\tilde{S}$, ξ and λ that result in the solution of system of ODEs in Eq. 2.41 satisfying the desired boundary conditions in Eq. 2.48.

The next step in our numerical implementation is to minimize the free energy of the system with respect to the "artificially" enforced intersection point $\tilde{X}$, at which the membrane shape intersects with the x-axis. By doing so we will get the shape, that minimizes the free energy of the membrane, for given $\tilde{R}$, $\tilde{D}$ and contact angle γ only.

A.1.5 Minimization or Maximization of Functions

At this step, we are given the function $\tilde{F}_f$ of a single variable $\tilde{X}$ and our task is to find the value $\tilde{X}_m$ where $\tilde{F}_f$ takes on a maximum or a minimum value. Since we have a one-dimensional minimization problem, the easiest approach would be to initially bracket the minimum, and subsequently pin it down to desired precision by simple golden section search method. Bracketing the minimum is usually desired, since it gives us the confidence that the minimum exists and is within the bracket, while the golden section search allows us to find the minimum without calculating the derivative of the free energy function. Most importantly, the reason for choosing this approach is the fact that for any calculation of

the free energy for a new value of $\tilde{X}$ (of which we have to do many in the minimization process), we need to have a close-enough guess as our starting point. Since we always choose the previous solution as a guess for the next one, we are restricted to small steps when changing the variable $\tilde{X}$, which often times results in having to "walk" to the new value of the $\tilde{X}$ instead of jumping to it.

Bracketing of the Minimum and Golden Section Search

A minimum is known to be bracketed if we can find a triplet of points $\tilde{X}_a < \tilde{X}_b < \tilde{X}_c$, such that $\tilde{F}_f(\tilde{X}_b)$ is less than both $\tilde{F}_f(\tilde{X}_a)$ and $\tilde{F}_f(\tilde{X}_c)$. In this case we know for sure that the function has a minimum in the interval $(\tilde{X}_a, \tilde{X}_c)$. To bracket the minimum numerically, we follow closely the directions in Ref. [92]. One edge of the bracketing boundary is chosen to be the solution (i.e. minima) from the previous guess, while the other end is chosen by simply stepping downhill with gradually increasing step-size until the turning point is reached. In case of a failure we increase the step-size either by a constant factor or by a parabolic extrapolation of the preceding points that is designed to take us to the extrapolated turning point. Since we are stepping downhill, one end of the bracket and the middle point are already known, so we just need to make a big enough step to stop the downhill trend and choose that as the other end of the bracketing boundary.

After the initial bracketing, the next step then is to choose a new point $\tilde{X}$, either between $\tilde{X}_a$ and $\tilde{X}_b$ or between $\tilde{X}_b$ and $\tilde{X}_c$. Suppose we choose the new $\tilde{X}$ point to be between $\tilde{X}_b$ and $\tilde{X}_c$ and evaluate the function $\tilde{F}_f$ at that point. If $\tilde{F}_f(\tilde{X}_b) < \tilde{F}_f(\tilde{X})$, then the new bracketing triplet of points is $(\tilde{X}_a, \tilde{X}_b, \tilde{X})$. Otherwise, if $f(\tilde{X}_b) > f(\tilde{X})$, then the new bracketing triplet is $(\tilde{X}_b, \tilde{X}, \tilde{X}_c)$. In all cases the middle point of the new triplet is the abscissa whose ordinate is the best minimum achieved so far. We then continue the process until the distance between the two outer points of the triplet is tolerably small.

But how do we choose the new point $\tilde{X}$ given the bracket triple $(\tilde{X}_a, \tilde{X}_b, \tilde{X}_c)$? If $\tilde{X}_b$ is a fraction w of the way between $\tilde{X}_a$ and $\tilde{X}_c$, then

$$\frac{\tilde{X}_b - \tilde{X}_a}{\tilde{X}_c - \tilde{X}_a} = w, \tag{A.21}$$

$$\frac{\tilde{X}_c - \tilde{X}_b}{\tilde{X}_c - \tilde{X}_a} = 1 - w. \tag{A.22}$$

Imagine that the new point $\tilde{X}$ that we pick is also a fraction z beyond the point $\tilde{X}_b$, so that

$$\frac{\tilde{X} - \tilde{X}_b}{\tilde{X}_c - \tilde{X}_a} = z. \tag{A.23}$$

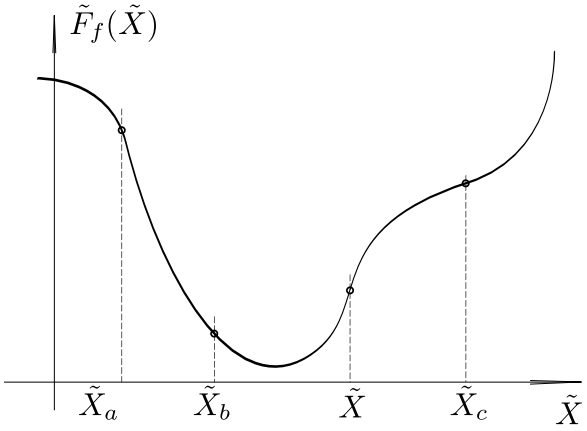

Figure A.2: Illustration of the golden section search of a minimum. The minimum is originally bracketed by points $\tilde{X}_a$, $\tilde{X}_b$ and $\tilde{X}_c$. The function is then evaluated at a new point $\tilde{X}$, after which the minimum is bracketed by points $\tilde{X}_b$, $\tilde{X}$ and $\tilde{X}_c$ and our current best guess for the minimum is the value of the function at the point $\tilde{X}$.

This means that our next bracketing interval is going to be either of length $w + z$ (new bracket $(\tilde{X}_a, \tilde{X}_b, \tilde{X})$) or $1 - w$ (new bracket $(\tilde{X}_b, \tilde{X}, \tilde{X}_c)$), and if we want to minimize the worst case possibility then z needs to be chosen such that the two intervals have an equal length

$$z = 1 - 2w. \tag{A.24}$$

Since the process of bracketing is done continuously until the desired precision is reached, the original bracket $(\tilde{X}_a, \tilde{X}_b, \tilde{X}_c)$ must have been chosen in a similar manner. In other words, $\tilde{X}$ should be the same fraction between $\tilde{X}_b$ and $\tilde{X}_c$, as was $\tilde{X}_b$ from $\tilde{X}_a$ to $\tilde{X}_c$, which implies

$$\frac{z}{1 - w} = w. \tag{A.25}$$

Eq. A.25 along with the Eq. A.24 yields,

$$w \approx 0.38197. \tag{A.26}$$

This means that at each step the optimal bracketing interval $(\tilde{X}_a, \tilde{X}_b, \tilde{X}_c)$ has its middle point a fractional distance 0.38197 from one end, and 0.61803 from the other. These fractions are called the golden section and thus the method is called the golden section search.

In summary, at each stage, given a bracketing triplet of points, we pick a "trial" point which is a fraction 0.38197 into the larger of the two intervals and find the new triplet based on the value of the function at the new point. The is then repeated until the desired precision is reached.

Appendix B

Contact Curvature

In this work, we assume that the membrane shape tangentially connects with the cylinder's surface at the contact point. As discussed in the Section 2.4, the curvature at the contact point is not known *a priori* and needs to be determined through the condition of flatness at the symmetry point via, for example, shooting method. In this section, we want to show that, if the energy is stationary, additional boundary condition can be imposed. In Ref. [87], Seifert showed that the difference between the curvature of the membrane at the contact point and the curvature of the substrate is related to the adhesion energy through a simple relationship,

$$\left(C_0 - \frac{1}{\tilde{R}}\right)^2 = 2|\tilde{w}|. \tag{B.1}$$

Note that this boundary condition cannot be enforced if the detachment point is fixed, but only holds if the energy is stationary. Below, we want to derive this boundary condition from the stationarity equation.

Assume that at the equilibrium point of detachment the contact angle is ψ_0 and the curvature of the substrate is C_0. The variation of the arclength δs entails the following change in the contact angle ψ,

$$\delta\psi = \left(C_0 + \frac{\cos\psi_0}{r_0}\right)\delta s, \tag{B.2}$$

which implies changes in the energy of the system, both from the free and the bound parts of the membrane. For simplicity let's assume that the variation results in an additional piece of area $\delta A = L\delta s$ being wrapped around the cylinder. This piece will change the adhesion, bending and surface tension terms for the adhered part of the membrane, that are

easy to calculate since the substrate shape is known. For contributions from the free part of the membrane we need to look at the boundary terms which occur upon the variation of the functional

$$\delta\tilde{F}_{free}|_{boundary} = \left[\frac{\partial L}{\partial\dot{\psi}}\delta\psi - H\delta s\right]_{boundary}. \tag{B.3}$$

Let us derive the variation above. Recall the Lagrangian in our problem,

$$L = \frac{\kappa}{2}\left[\frac{d\psi}{ds} - \frac{\cos\psi}{r}\right]^2 + \sigma, \tag{B.4}$$

thus

$$P_\psi = \frac{\partial L}{\partial\dot{\psi}} = \kappa\left[\frac{d\psi}{ds} - \frac{\cos\psi}{r}\right]. \tag{B.5}$$

The Hamiltonian can then be written as,

$$H = \dot{\psi}P_\psi - L = \left(\frac{P_\psi}{\kappa} + \frac{\cos\psi}{r}\right)P_\psi - \frac{P_\psi^2}{2\kappa} - \sigma, \tag{B.6}$$

$$H = \frac{P_\psi^2}{2\kappa} + \frac{P_\psi\cos\psi}{r} - \sigma. \tag{B.7}$$

Since a piece of a membrane is removed during this variation the contribution from Eq. B.3 contributes with a negative sign. The total change in the energy is therefore given by

$$\begin{aligned}\delta\tilde{F} &= (-w + \frac{1}{2}C_0^2 + \sigma)\delta s \\ &- \left[\kappa\left(\dot{\psi}_0 - \frac{\cos\psi_0}{r_0}\right)\left(C_0 + \frac{\cos\psi_0}{r_0}\right) - \frac{1}{2}\kappa\dot{\psi_0}^2 + \frac{1}{2}\kappa\left(\frac{\cos\psi_0}{r_0}\right)^2 + \sigma\right]\delta s.\end{aligned} \tag{B.8}$$

Setting $\delta\tilde{F} = 0$, we obtain a simple expression for the contact curvature

$$\left(\dot{\psi}_0 - \frac{\cos\psi_0}{r_0} - C_0\right)^2 = 2|\tilde{w}|, \tag{B.9}$$

which for cylindrical colloids becomes

$$\left(\dot{\psi}_0 - \frac{\cos\psi_0}{r_0} - \frac{1}{\tilde{R}}\right)^2 = 2|\tilde{w}|, \tag{B.10}$$

where

$$C_0 = \dot{\psi}_0 - \frac{\cos\psi_0}{r_0} \tag{B.11}$$

is the curvature of the substrate at the contact point.

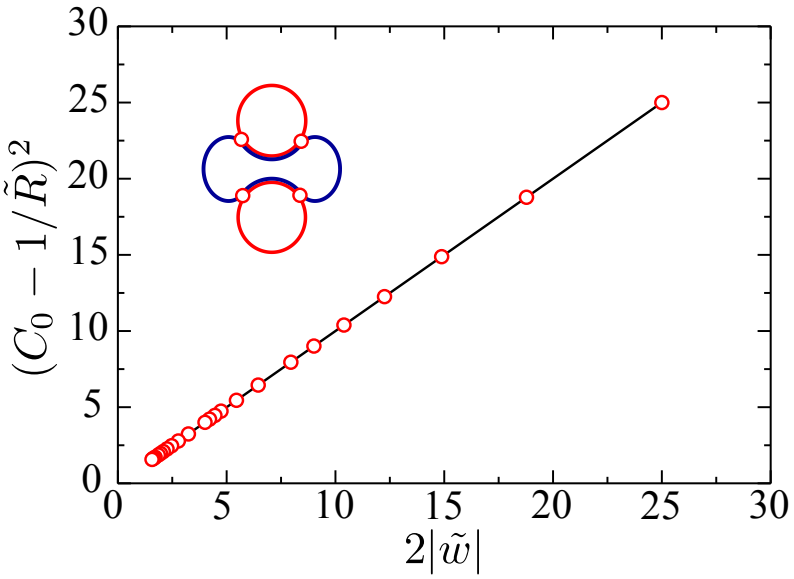

Figure B.1: Numerical results for the square of the difference between the curvature of free membrane portion and the curvature of the wrapped cylinder at the contact point $\tilde{s} = 0$ as a function of $2|\tilde{w}|$, for various values of $\tilde{R}$. The straight line represents the theoretical result, Eq.(38), from Ref. [63].

References

[1] H. Lodish, A. Berk, L. Zipursky, P. Matsudaira, D. Baltimore, and J. Darnell. *Molecular Cell Biology*. W. H. Freeman, Reading, Massachusetts, fourth edition, 1999.

[2] R. B. Gennis. *Biomembranes: Molecular Structure and Function*. Springer, Berlin, 1989.

[3] R. Lipowsky and E. Sackmann. *Structure and Dynamics of Membranes, Handbook of Biological Physics*. Elsevier, New York/North-Holland, Amsterdam, 1995.

[4] H. T. Tien and A. Ottova-Leitmannova. *Planar Lipid Bilayers (BLMs) and Their Applications*. Elsevier Science, Amsterdam, 2003.

[5] D. F. Evans and H. Wennerstrom. *The Colloidal Domain: Where Physics, Chemistry and Biology Meet*. Wiley-VCH, New York, second edition, 1994.

[6] A. Boulbitch. *Europhysics Letters*, 59:910, 2002.

[7] T. R. Weikl. *The European Physical Journal E: Soft Matter and Biological Physics*, 12:265, 2003.

[8] M. Deserno. *Physical Review E*, 69:031903, 2004.

[9] M. Deserno. *Journal of Physics: Condensed Matter*, 16:S2061, 2004.

[10] S. Mkrtchyan, C. Ing, and J. Z. Y. Chen. *Physical Review E*, 81:011904, 2010.

[11] H. Garoff, R. Hewson, and D.-J. E. Opstelten. *Microbiology and Molecular Biology Reviews*, 62:1171, 1998.

[12] S. B. Sieczkarski and G. R. Whittaker. *Journal of General Virology*, 83:1535, 2002.

[13] H. Garoff and K. Simons. *Proceedings of the National Academy of Sciences of the United States of America*, 71:3988, 1974.

[14] K. Simons, H. Garoff, and A. Helenius. *Scientific American*, 246:58, 1982.

[15] Y. E. Lu and M. Kielian. *Journal of Virlogy*, 74:7708, 2000.

[16] E. Evans and W. Rawicz. *Physical Review Letters*, 64:2094, 1990.

[17] J. Song and R. E. Waugh. *Journal of Biomechanical Engineering*, 112:235, 1990.

[18] D. V. Zhelev, D. Needham, and R. M. Hochmuth. *Biophysical Journal*, 67:720, 1994.

[19] F. M. Hochmuth, J. Y. Shao, J. Dai, and M. P. Sheetz. *Biophysical Journal*, 70:358369, 1996.

[20] R. Bar-Ziv, T. Frisch, and E. Moses. *Physical Review Letters*, 75:3481, 1995.

[21] R. Bar-Ziv, E. Moses, and P. Nelson. *Biophysical Journal*, 71:294, 1998.

[22] J. Dai and M. P. Sheetz. *Biophysical Journal*, 77:3363, 1999.

[23] N. Borghi, O. Rossier, and F. Brochard-Wyart. *Europhysics Letters*, 64:837, 2003.

[24] A. Roux, G. Cappello, J. Cartaud, J. Prost, B. Goud, and P. Bassereau. *Proceedings of the National Academy of Sciences of the United States of America*, 99:5394, 2002.

[25] I. Tsafrir, Y. Caspi, M.-A. Guedeau-Boudeville, T. Arzi, and J. Stavans. *Physical Review Letters*, 91:138102, 2003.

[26] O. Campas, C. Leduc, P. Bassereau, J. Casademunt, J.-F. Joanny, and J. Prost. *Biophysical Journal*, 94:5009, 2008.

[27] F. Brochard-Wyart, T. Tanaka, N. Borghi, and P.-G. de Gennes. *Langmuir*, 21:4144, 2005.

[28] J. Z. Y. Chen. *Physical Review Letters*, 98:088302, 2007.

[29] J. Z. Y. Chen, Y. Liu, and H. J. Liang. *Physical Review Letters*, 102:168103, 2009.

[30] I. Derenyi, F. Julicher, and J. Prost. *Physical Review Letters*, 88:238101, 2002.

[31] T. R. Powers, G. Huber, and R. E. Goldstein. *Physical Review E*, 65:041901, 2002.

[32] M. Tokarz, B. Akerman, J. Olofsson, J.-F. Joanny, Paul Dommersnes, and O. Orwar. *Proceedings of the National Academy of Sciences of the United States of America*, 102:9127, 2005.

[33] M. Tokarz, B. Hakonen, P. Dommersnes, O. Orwar, and B. Akerman. *Langmuir*, 23:7652, 2007.

[34] F. Campelo and A. Hernandez-Machado. *Physical Review Letters*, 100:158103, 2008.

[35] J. Hurtig and O. Orwar. *Soft Matter*, 4:1515, 2008.

[36] B. J. Reynwar and M. Deserno. *Soft Matter*, 7:8567, 2011.

[37] M. M. Muller, M. Deserno, and J. Guven. *Physical Review E*, 76:011921, 2007.

[38] M. Deserno, M. M. Muller, and J. Guven. *Physical Review E*, 76:011605, 2007.

[39] M. M. Muller, M. Deserno, and J. Guven. *Physical Review E*, 72:061407, 2005.

[40] M. M. Muller, M. Deserno, and J. Guven. *Europhysics Letters*, 69:482, 2005.

[41] B. J. Reynwar, G. Illya, V. A. Harmandaris, M. M. Muller, K. Kremer, and M. Deserno. *Nature*, 447:461, 2007.

[42] I. Koltover, J. O. Radler, and C. R. Safinya. *Physical Review Letters*, 82:1991, 1999.

[43] K. S. Kim, J. Neu, and G. Oster. *Biophysical Journal*, 75:2274, 1998.

[44] Y. Yu and S. Granick. *Journal of the American Chemical Society*, 131:14158, 2009.

[45] T. Bickel. *Journal of Chemical Physics*, 118:8960, 2003.

[46] B. Rozycki, R. Lipowsky, and T. R. Weikl. *European Physics Letters*, 84:26004, 2008.

[47] M. Karlsson, K. Sott, A.-S. Cans, A. Karlsson, R. Karlsson, and O. Orwar. *Langmuir*, 17:6754, 2001.

[48] W. Helfrich and R.-M. Servuss. *Il Nuovo Cimento D*, 3:137, 1984.

[49] W. Helfrich. *Z. Naturforsch C*, 28:693, 1973.

[50] U. Seifert and R. Lipowsky. *Physical Review A*, 42:4768, 1990.

[51] J. Z. Y. Chen and S. Mkrtchyan. *Physical Review E*, 81:041906, 2010.

[52] R. Lipowsky. *Nature*, 349:475, 1991.

[53] D. Boal. *Mechanics of the Cell*. Cambridge University Press, Cambridge, UK, 2012.

[54] S. A. Safran. *Statistical Thermodynamics of Surfaces, Interfaces, and Membranes*. Addison-Wesley Pub., Reading, Mass., 1994.

[55] D. R. Nelson, T. Piran, and S. Weinberg. *Statistical Mechanics of Membranes and Surfaces*. World Scientific Pub., River Edge, N.J., 2004.

[56] P. B. Canham. *Journal of Theoretical Biology*, 26:61, 1970.

[57] H. J. Deuling and W. Helfrich. *Journal de Physique*, 37:1335, 1976.

[58] R. Mukhopadhyay, H. W. G Lim, and M. Wortis. *Biophysical Journal*, 82:1756, 2002.

[59] H. W. G Lim, M. Wortis, and R. Mukhopadhyay. *Proceedings of the National Academy of Sciences of the United States of America*, 99:16766, 2002.

[60] F. Brochard and J. F. Lennon. *Journal de Physique*, 36:1035, 1975.

[61] N. Gov, A. G. Zilman, and S. Safran. *Physical Review Letters*, 90:228101, 2003.

[62] J.-B. Fournier, D. Lacoste, and E. Raphael. *Physical Review Letters*, 92:018102, 2004.

[63] U. Seifert, K. Berndl, and R. Lipowsky. *Physical Review A*, 44:1182, 1991.

[64] L. Miao, B. Fourcade, M. R. M. Wortis, and R. K. P. Zia. *Physical Review A*, 43:6843, 1991.

[65] L. Miao, U. Seifert, and M. D. Dobereiner. *Physical Review E*, 49:5389, 1994.

[66] M. Goulian, R. Bruinsma, and P. Pincus. *Europhysics Letters*, 22:145, 1993.

[67] I. Tsafrir, D. Sagi, T. Arzi, M.-A. Guedeau-Boudeville, V. Frette, D. Kandel, and J. Stavans. *Physical Review Letters*, 86:1138, 2001.

[68] R. Lipowsky and U. Seifert. *Langmuir*, 7:1867, 1991.

[69] M. Deserno and W. M. Gelbart. *Journal of Physical Chemistry B*, 106:5543, 2002.

[70] M. Deserno and T. Bickel. *Europhysics Letters*, 62:767, 2003.

[71] A. Saric and A. Cacciuto. *Physical Review Letters*, 108:118101, 2012.

[72] J. C. Pamies and A. Cacciuto. *Physical Review Letters*, 106:045702, 2011.

[73] P. Gosselin, H. Mohrbach, and M. M. Muller. *Physical Review E*, 83:051921, 2011.

[74] H. B. G. Casimir. *Proceedings of the Koninklijke Nederlandse Akademie van Wetenschappen*, 51:793, 1948.

[75] T. R. Weikl, M. M. Kozlov, and W. Helfrich. *Physical Review E*, 57:6988, 1998.

[76] D. Bartolo and J.-B. Fournier. *European Physical Journal E*, 11:141, 2003.

[77] P. D. Blood and G. A. Voth. *Proceedings of the National Academy of Sciences of the United States of America*, 103:15068, 2006.

[78] B. Antonny. *Current Opinion in Cell Biology*, 18:386, 2006.

[79] J. N. Israelachvili, D. J. Mitchell, and B. W. Ninham. *Journal of the Chemical Society, Faraday Transactions 2*, 72:1525, 1976.

[80] E. Evans and D. Needham. *Journal of Physical Chemistry*, 91:4219, 1987.

[81] W. Rawicz, K. C. Olbrich, T. McIntosh, D. Needham, and E. Evans. *Biophysical Journal*, 79:328, 2000.

[82] P. A. Wiggins and P. C. Nelson. *Physical Review E*, 73:031906, 2006.

[83] A. Pressley. *Elementary Differential Geometry*. Springer, 2005.

[84] E. Kreyszig. *Differential Geometry*. Dover, New York, 1991.

[85] F. David. *Statistical Mechanics of Membranes and Surfaces*. World Scientific, Singapore, second edition, 2004.

[86] M. Do Carmo. *Differential Geometry of Curves and Surfaces*. Prentice Hall, Englewood Cliffs, 1976.

[87] U. Seifert. *Physical Review A*, 43:6803, 1991.

[88] W. T. Gozdz. *Langmuir*, 23:5665, 2007.

[89] S. Cao, G. Wei, and J. Z. Y. Chen. *Physical Review E*, 84:050901(R), 2011.

[90] J. Benoit and A. Saxena. *Physical Review E*, 76:041912, 2007.

[91] K. Brakke. *Experimental Mathematics*, 1:141, 1992.

[92] W. H. Press, S. A. Teukolsky, W. T. Vetterling, and B. P. Flannery. *Numerical Recipes in C: The Art of Scientific Computing*. Cambridge : University Press, 1992.

[93] F. Campelo, J.-M. Allain, and M. B. Amar. *Europhysics Letters*, 77:1, 2007.

[94] B. Pontes, N. B. Viana, L. Campanati, M. Farina, V. M. Neto, and H. M. Nussenzveig. *European Biophysics Journal*, 37:121, 2008.

[95] S. Tzlil, M. Deserno, W. M. Gelbart, and A. Ben-Shaul. *Biophysical Journal*, 86:2037, 2004.

[96] F. L. H. Brown. *Annual Review of Physical Chemistry*, 59:685–712, 2008.

[97] S. Tristram-Nagle and J.F. Nagle. *Chemistry and Physics of Lipids*, 127:3–14, 2004.

[98] J. F. Nagle. *Annual Review of Physical Chemistry*, 31:157195, 1980.

[99] J. F. Nagle and H. L. Scott. *Physics Today*, 31:38–47, 1978.

[100] D. L. Melchior and J. M. Steim. *Biochimica Et Biophysical Acta*, 466:148–159, 1977.

[101] F. Wunderlich, W. Kreutz, P. Mahler, A. Ronai, and G. Heppeler. *Biochemistry*, 17:2005–2010, 1978.

[102] D. R. Nelson and L. Peliti. *Journal de Physique*, 48:1085–1092, 1987.

[103] M. Deserno. Fluid Lipid Membranes. "http://www.cmu.edu/biolphys/deserno/pdf/membrane_theory.pdf".

[104] M. Deserno. Notes on Differential Geometry. "http://www.cmu.edu/biolphys/deserno/pdf/diff_geom.pdf".

[105] H. B. Callen. *Thermodynamics*. Wiley & Sons, New York, 1961.

[106] R. Phillips, J. Kondev, and J. Theriot. *Physical Biology of the Cell*. Garland Science, first edition, 2009.